EVOLUTION OF TURBINE BLADE DEPOSITS IN AN ACCELERATED

DEPOSITION FACILITY: ROUGHNESS

AND THERMAL ANALYSIS

by

James E. Wammack

A thesis submitted to the faculty of

Brigham Young University

In partial fulfillment of the requirements for the degree of

Master of Science

Department of Mechanical Engineering

Brigham Young University

December 2005

BRIGHAM YOUNG UNIVERSITY

GRADUATE COMMITTEE APPROVAL

of a thesis submitted by

James E. Wammack

This thesis has been read by each member of the following graduate committee and by majority vote has been found to be satisfactory.

12 Aug 05	_Jeffrey P. Bons, Chair_
Date	Jeffrey P. Bons, Chair
August 12, 2005	_Thomas H. Fletcher_
Date	Thomas H. Fletcher
12 August 2005	_Brent W. Webb_
Date	Brent W. Webb

BRIGHAM YOUNG UNIVERSITY

As chair of the candidate's graduate committee, I have read the thesis of James E. Wammack in its final form and have found that (1) its format, citations, and bibliographical style are consistent and acceptable and fulfill university and department style requirements; (2) its illustrative materials including figures, tables, and charts are in place; and (3) the final manuscript is satisfactory to the graduate committee and is ready for submission to the university library.

_____26 OCT 2005_____   _____
Date   Jeffrey P. Bons
                                                                 Chair, Graduate Committee

Accepted for the Department

                                              _____
                                              Matthew R. Jones
                                              Graduate Coordinator

Accepted for the College

                                              _____
                                              Alan R. Parkinson
                                              Dean, Ira A. Fulton College of Engineering
                                              and Technology

ABSTRACT

EVOLUTION OF TURBINE BLADE DEPOSITS IN AN ACCELERATED

DEPOSITION FACILITY: ROUGHNESS

AND THERMAL ANALYSIS

James E. Wammack

Department of Mechanical Engineering

Master of Science

During the operation of a gas turbine, ingested contaminants present in the air form

deposits on the surfaces of the turbine blades. These deposits grow over time, resulting in

an increasingly rough surface. This gradual increase in roughness results in several

negative consequences, among which is an increase in the rate of heat transfer to the

blade which shortens blade life. This thesis presents research in which deposits were

evolved on three different turbine blade coupons and their evolution was studied. A trend

in roughness change over time was discovered. Also, an attempt was made to find the

effect of the deposits on the heat transfer characteristics of a coupon surface. The deposits

were formed using the BYU Turbine Accelerated Deposition Facility (TADF), which was

used to simulate three months of deposition within a two hour test time. All three

coupons underwent four cycles in the TADF: eight total hours of combustor testing—or

one simulated year of deposition—with topological measurements being made on the coupon surface after every two hours (three simulated months) of testing. The data produced by the topological measurements were used with a CNC mill to machine scaled-up plastic models of the rough surfaces: four surfaces per model representing three, six, nine, and twelve simulated months of deposition. The models were placed in a wind tunnel where, following a period of thermal soaking at room temperature, they were suddenly exposed to a heated air stream. The thermal histories of the model were recorded with an infrared camera and were used to derive the heat transfer coefficient of each surface using the method developed by Shultz and Jones. The heat transfer coefficients are reported in the form of Stanton numbers to allow for the difference in thermal properties between the conditions and properties of the wind tunnel and its components and those of a real gas turbine. The Stanton numbers for the various surfaces were plotted versus the simulated gas turbine operational time. Additionally, several roughness correlations were used to predict the Stanton number for each surface, producing a probable Stanton number history for the coupon. The measured non-dimensional heat transfer coefficients did not reach the magnitudes predicted by the correlations. This is most likely due to unexpected flow conditions inside the wind tunnel. Recommendations for future research are presented.

ACKNOWLEDGEMENTS

This thesis would not have been possible without the guidance, assistance, and support of several people. I would like to thank my graduate advisor, Dr. Jeffrey Bons, for allowing me the opportunity to work on such a fascinating and challenging project. I would also like to thank the other members of my graduate committee, Drs. Tom Fletcher and Brent Webb. Their varied fields of experience and insight allowed me to better understand and appreciate the many facets of scientific research. I am also grateful for the generous grant from the BYU Department of Mechanical Engineering that helped this project to reach completion.

I would also like to express my gratitude for the efforts of Jared Jensen, whose research made my own possible. Thanks also goes out to Ken Forster and Kevin Cole whose expertise and willingness to help greatly benefited the project. The efforts and assistance of Jared Crosby, Daniel Fletcher, and John Pettitt were instrumental in the successful completion of this thesis.

Finally, I would like to thank my ever-patient wife La Tisha and our daughters MacKayla and Annika for their love and support during a challenging time.

TABLE OF CONTENTS

LIST OF FIGURES

LIST OF TABLES

Nomenclature

English Symbols

A_{exit} Area of TADF nozzle exit [m^2]

B Bias error

c_f Coefficient of friction

c_P Specific heat [J/kg*K]

GT   Gas Turbine

h Convective heat transfer coefficient [W/m^2*K]

H   Shape factor (δ^*/θ)

HP   High Pressure (in reference to a gas turbine)

k Average roughness height [mm or μm]

k_s Equivalent sandgrain roughness [mm]

k^+ Roughness Reynolds number

M   Mach number

$\dot{m}$ Mass flow rate [kg/s]

n Sample size

ppmw   Parts per million by weight

Pr   Prandtl number

Pr$_t$ Turbulent Prandtl number

$P_{\bar{x}}$ Precision uncertainty in the mean

ΔP	Pressure difference (as measured by the Druck transducer) [Pa]
q	Thermal energy [W]
R	Gas constant [J/kg*K]
R	Tool-tip radius [mm]
Ra	Average roughness (a.k.a. Centerline average roughness) [μm]
Re_x	Reynolds number with respect to x
Rq	Root-mean-square roughness [μm]
Rt	Maximum peak-to-valley roughness [μm]
Rz	Mean peak-to-valley roughness [μm]
St	Stanton number
St_{avg}	Average Stanton number
St_0	Flat plate Stanton number
S_x	Standard deviation
$S_{\bar{x}}$	Standard deviation of the mean
S_w/S	Ratio of wetted surface area versus planform area
$S_{y,x}$	Standard error of estimate
t	Time [s]; Student-t distribution
TADF	Turbine Accelerated Deposition Facility
TBC	Thermal Barrier Coat
T_S	Surface temperature [°C]
T_w	Wind tunnel wall temperature [°C]
T_∞	Freestream temperature [°C]
U_∞	Freestream velocity [m/s]

w	Uncertainty
x	With respect to the *x*-axis
y	With respect to the *y*-axis

Greek Symbols

α	Thermal diffusivity ($k/\rho c_P$) [m^2/s]
$\overline{\alpha_f}$	Average forward facing angle [degrees]
α_{rms}	Root-mean-square of surface slope angle [degrees]
δ^*	Displacement thickness [mm]
κ	Thermal conductivity [W/m*K];
Λ_s	Roughness shape/density parameter
μ	Viscosity [Pa*s]
ν	Degrees of freedom [*n*-1]
θ	Momentum thickness [mm]
ρ	Density [kg/m^3]

Subscripts

i	Refers to the *i*th element
j	Refers to the jth element

Chapter 1: Introduction

1.1   Background

As a gas turbine operates, large quantities of air are ingested. This air is passed through

filters so as to remove various contaminants found in the atmosphere. These

contaminants may be composed of a variety of substances such as dust or airborne

pollutants that are produced by the combustion of fossil fuels. Although newly installed

filters may be able to capture most particulate before it is able to enter the engine,

degradation over time can allow particulate of ever-increasing size to pass through the

filter. Although after some service a filter may be capable of preventing the passage of

particles 20-80 μm in diameter, some particles less than 20 μm in diameter may still pass

through (Jensen, 2004). These particles pass through the combustor where they are heated

by the exhaust gases and can change phase. As they continue through the turbine section

of the engine, the particles tend to erode the turbine blades if the particles are below a

certain threshold temperature, or, if above the threshold temperature, to adhere to the

turbine blades, creating deposits on the blade surfaces. Once beyond the temperature

where the particulate changes phase, the rate of particulate agglomeration increases while

the rate of blade erosion decreases (Wenglarz & Wright, 2002). Studies involving aircraft

engines indicate that this threshold appears to occur between 980 and 1150°C (Wenglarz

& Wright, 2002; Smialek et al., 1992; Toriz et al., 1988). In one study involving volcanic

ash ingestion by an aircraft engine, deposits did not occur at temperatures lower than

1

1121°C (Kim et al., 1993). Once formed, deposits roughen the blade surfaces resulting in an increase in the convective heat transfer rate between the exhaust gases and the turbine blades. Over time, as the deposits grow, the heat transfer rate increases, thus decreasing the life of the blades.

Unfortunately, because this deposition process requires thousands of hours to occur in a gas turbine engine, and because it is not economically feasible to shut down a gas turbine at frequent intervals for study, little is known about the heat transfer properties of real turbine surfaces (Bons et al., 2001). Although many studies have been undertaken to characterize the heat transfer properties of a roughened turbine blade, most suffer from at least one of two shortcomings. First, in many studies, real roughness was simulated using an artificially roughened surface [e.g., a study by Stripf and Wittig (2005) in which heat transfer measurements were performed on blades roughened with evenly spaced truncated cones]. While matching the roughness statistics of a real turbine blade, this approach does not replicate the irregular structure of genuine turbine blade deposits (Bons et al., 2001). Second, in the event that real roughened surfaces are used in a study, the surfaces used represent the condition of the blade surface at a single moment in time and do not provide a detailed account of the evolutionary history of the deposits. In one extensive study in which real deposits were used as the basis for convective heat transfer experiments, 100 samples were obtained from four turbine manufacturers that were "representative of surface conditions generally found in the land-based gas turbine inventory (Bons, 2002)."
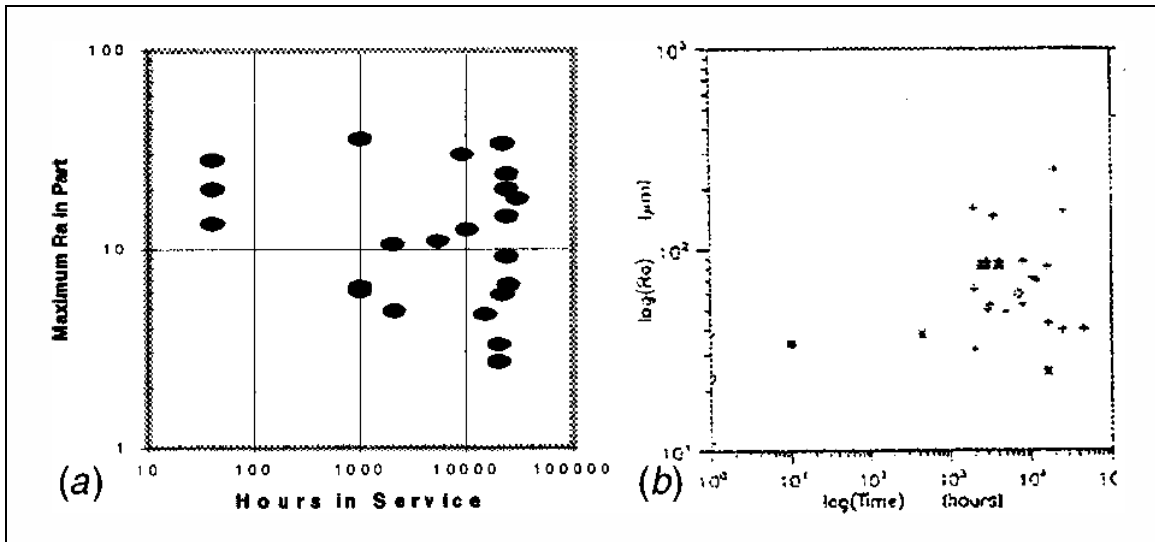
Figure 1. Distribution of Ra values for multiple turbine blades from studies by Bons et al., 2001 and Tarada et al., 1993.

Although allowing a broad view of the different kinds of surfaces that may be found on gas turbine blades after many hours of operation, these samples were taken from a variety of gas turbines, each operating under different conditions and in different environments. Figure 1 illustrates the amount of scatter encountered when the surface roughness from a number of turbine blades procured from a variety of sources are plotted versus time of service. Without being able to study a particular turbine over a period of time, it would be impossible to make an in-depth study into the evolution of deposits under a given set of conditions.

In any event, even if samples could be taken from a single gas turbine, the deposition process occurs continuously from one maintenance period to the next—a duration of several thousand hours. Thus, it would be both economically difficult and time

3

consuming to obtain samples with the frequency required to study the evolution of deposits between maintenance cycles.

The difficulty of obtaining deposits for study under controlled conditions was overcome with the creation of a facility that rapidly reproduces the sort of deposition found on turbine blade surfaces (Jensen et al., 2005). The facility consists of a specialized combustor capable of creating deposits on small turbine blade coupons at a vastly accelerated rate and under controllable conditions. This combustor—named the Turbine Accelerated Deposition Facility (TADF)—was designed, constructed, and operated by Jensen with the author serving as an assistant.

1.2   TADF Validation

The deposits formed in the TADF were analyzed by Jensen et al. and presented at the ASME TURBO EXPO 2004 as well as in the ASME Journal of Turbomachinery (Jensen et al., 2005). Accelerated deposits were considered to be "valid" if they would produce the same thermodynamic effects on a gas turbine blade as real deposits do. These effects are twofold: first, as has already been mentioned, deposits increase the rate of convective heat transfer. Second, by forming an extra layer of material on a gas turbine blade surface, the deposits perform an insulating function. The validation process involved the comparison between deposits formed on a serviced gas turbine blade over a long period of time and deposits formed through accelerated deposition in the TADF. Three aspects were investigated: topography, internal structure, and chemical composition.

4

1.2.1 Topography of Accelerated Deposits

The conventional deposits and the accelerated deposits were initially compared visually. A side-by-side comparison showed a similar appearance with respect to color, roughness structure, area coverage, and deposit thickness.
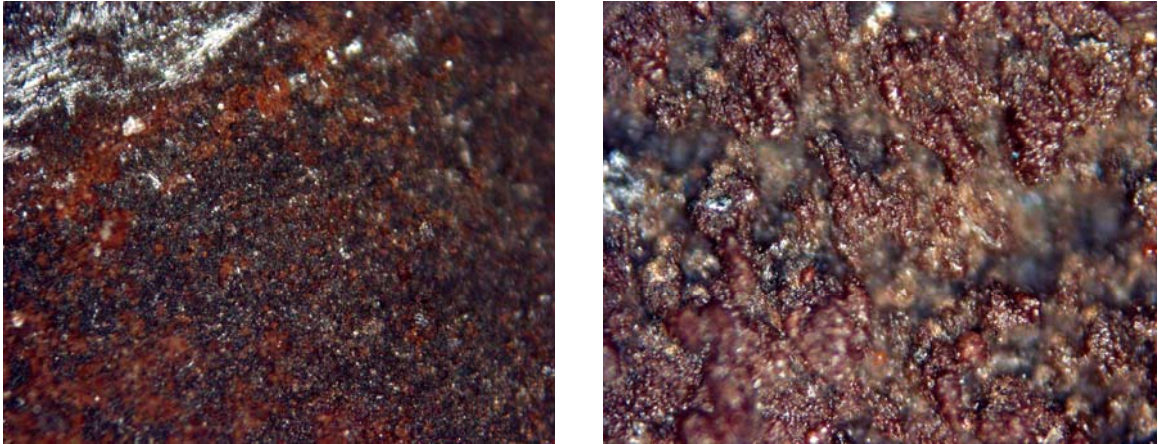
Figure 2. Photographs of service turbine blade (left) and accelerated sample (right). Images are magnified 10 times. Photographs represent an area 3 mm x 3 mm.

In addition to a visual comparison between surfaces (Figure 2), their respective roughness statistics were also compared. Due to the irregular nature of roughness and the unlikelihood of any two turbine blades having identical roughness patterns, blade roughness is usually compared through roughness statistics (e.g. *Ra*, *Rq*, *Rz*) as well as other parameters—such as the average forward-facing surface angle, $\overline{\alpha_f}$, the rms slope angle, α_{rms}, or the roughness shape/density parameter Λ_s (see Section 5.1.2)—that describe the physical character of the surface. Additionally, surface roughness correlates empirically with skin friction and convective heat transfer, thus giving an indication of the convective heat transfer properties of a surface (Blair, 1994; Boynton et al., 1993).

Therefore, if an accelerated deposition specimen and a serviced turbine blade share similar roughness characteristics, it is probable that they share similar convective heat transfer characteristics as well. Although direct measurement of convective heat transfer properties was not part of the original study performed by Jensen et al., such measurements are presented in the current study.

The surface of a coupon that had seen 4 hours in the TADF with a particulate loading of 60 ppmw (see section 2.1. for information regarding particulate loadings), as well as the surface of a serviced turbine blade that had 25,000 hours of operation, were scanned using a profilometer to determine the roughness of their surfaces as well as to produce three-dimensional surface maps (Figure 3).
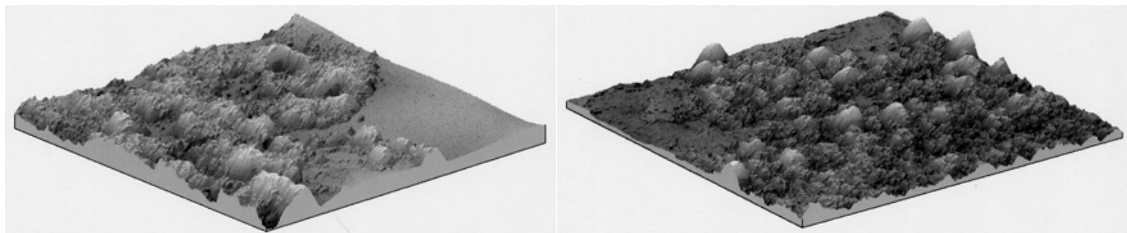
Figure 3. Surface map of a serviced turbine blade after 25,000 hours of operation (left) and a map of a coupon after 4 hours in the TADF (right). The area for each is approximately 4 mm x 4 mm.

Although there are some visible differences between the above two surfaces—most notably that the surface of the accelerated coupon is dominated by more distinct peaks than that of the serviced turbine blade—the respective heights of the roughness features are of the same order of magnitude. More so, the roughness statistics for various serviced turbine blades compare favorably to those obtained from coupons that were exposed to 4 hours of accelerated deposition (Table 1). That is to say that the variations between the

6

accelerated deposits and the deposits found on serviced hardware were within the

variation expected to occur between any two real turbine blades exposed to differing

deposition conditions.

Table 1. Roughness comparisons between accelerated deposits and serviced hardware.

	Surface Type	Ra (μm)	Rt (μm)	α_{rms}	S_w/S	Λ_s
Accelerated Test (4 hours)	60ppmw, at coupon edge Figure 3	28	257	29	1.43	13
	280ppmw, 90deg impingement	32	260	16.5	1.12	82
	280ppmw, 45deg impingement	10	107	13.7	1.06	180
	280ppmw, at coupon edge	38	249	18	1.11	87
Serviced Blades	25000hr blade Figure 3	32	240	27	1.36	22
	22500hr blade	41	296	24	1.24	36
	<1000hr blade	19	394	18	1.11	77
	24000hr vane	17	220	15.8	1.09	134

1.2.2   Internal Structure and Chemical Composition of Accelerated Deposits

In addition to increasing the rate of convective heat transfer between the exhaust gases

and the surface of the deposits, deposits tend to form an insulating layer, their second

thermodynamic effect on a turbine blade. Given the difficulty in accurately measuring the

thermal conductivity of deposit layers, Jensen et al. studied extensively two factors which

strongly affect overall thermal conductivity: deposit structure and chemical composition.

Deposit structure was studied by sectioning segments of serviced turbine blades and

accelerated deposition coupons and viewing their cross-sections with a scanning electron

7

microscope (SEM). Comparison between serviced turbine blades and coupons with

TADF-produced deposits showed the presence of elongated structures running parallel to

the turbine blade surface in both samples (Figure 4). The existence of similar internal

structures—and thus similar heat conduction paths, porosity, etc.—in both real and

accelerated deposits suggest similar heat conduction properties.
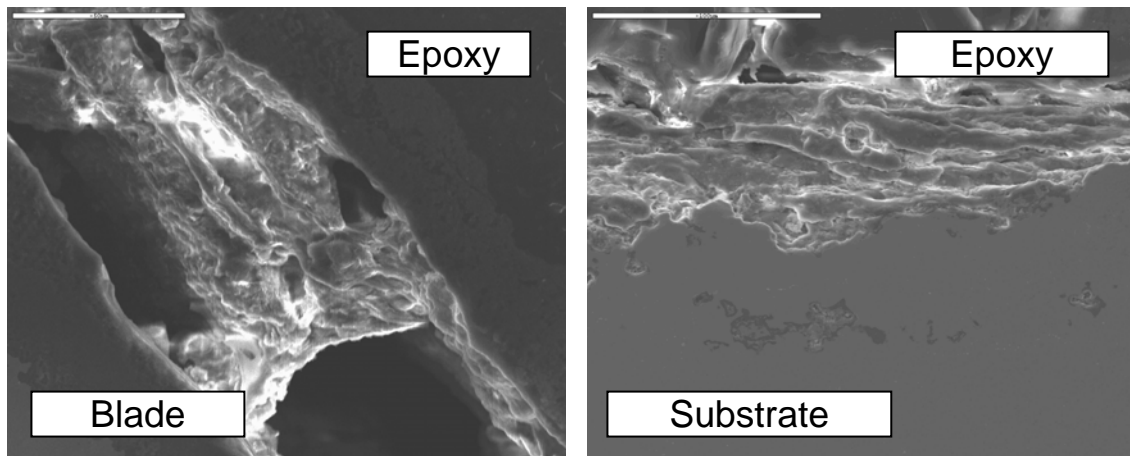
Figure 4. SEM cross-section from a 16000-hour service blade with a 50 μm metering bar (left) and an accelerated deposit specimen with a 100 μm metering bar (right).

Chemical composition is the second component of the thermal conductivity of a deposit

layer. The SEM used to analyze the internal structure of the deposit layers also had the

capability to determine chemical composition through the use of X-ray spectroscopy. The

chemical composition of the accelerated deposits was compared to that of service blade

deposits and aircraft engine deposits formed in desert conditions as reported by Borom et

al. (1996) (see Figure 5).
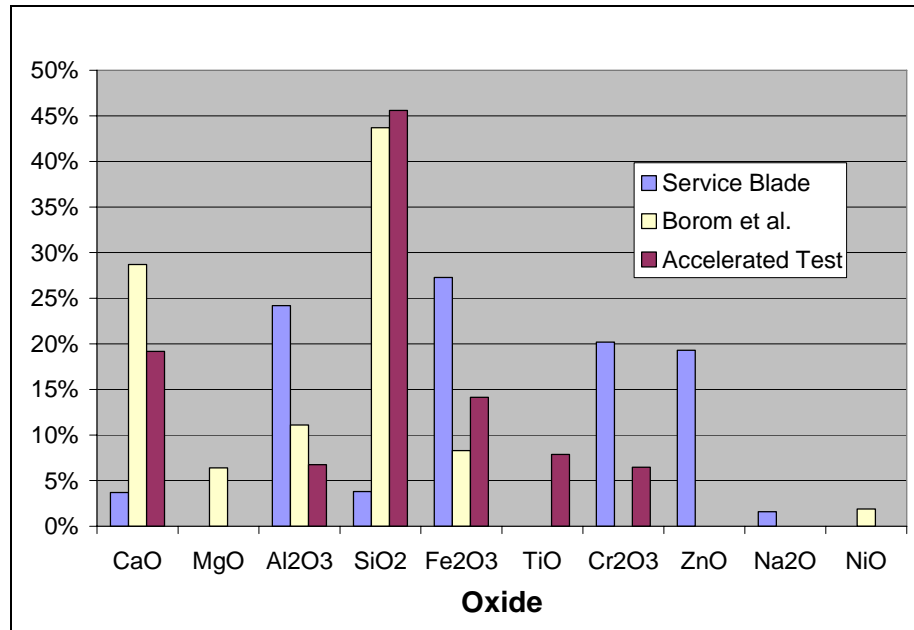
Figure 5. Comparison of weight percentages of elements found in deposits on a land-based service turbine blade, an aircraft service blade (as reported by Borom et al, 1996), and a TADF-produced accelerated test sample.

As shown in the figure, the chemical composition of the accelerated deposits most closely matched the composition of the deposits studied by Borom et al. Some variation is expected, however, due to the variety of chemical mixtures that can be found in different environments. Most importantly, analysis of several locations throughout the accelerated deposit layer showed that, like in-service turbine blades, the distribution of the component chemicals throughout the accelerated deposits was relatively homogeneous (Jensen, 2004). This indicates that a similar process occurs during both conventional deposition as well as accelerated deposition.

1.3   Objective

With the development and validation of the TADF, the ability to simulate deposit evolution within a reasonable time frame and under repeatable conditions was made possible. The objectives of the current study are twofold. The first objective is the production of deposits representative of those found on a gas turbine blade at several discrete moments within an approximately 10,000 hour operational cycle and to study any trends that may appear in the evolution of the surface roughness. The second objective is the determination of the convective heat transfer characteristics of each surface topology in order to determine how convective heat transfer rates change with deposit evolution during the operation of a gas turbine. It is hoped that this study will be the first in a line of studies meant to increase understanding of the changing conditions within a gas turbine, thus allowing better informed decisions regarding maintenance scheduling and the period between each shut-down.

Chapter 2: Deposition Evolution—Experimental Facilities and Techniques

2.1   Accelerated Deposition

The principle behind the production of accelerated deposits is that of matching the product of the particle flow rate and the number of hours of operation. Thus, if the particle flow rate through a gas turbine and the number of hours of operation was known, then the particle flow rate through the TADF could be determined for a given experimental time period. Conversely, a required experimental time period could be determined from a given TADF particle flow rate.

GT Particle Flow (ppmw) x Operational Hours = TADF Particle Flow (ppmw) x Experiment Hours

Thus:

TADF Particle Flow (ppmw) = (GT Particle Flow (ppmw) x Operation Hours)/Experiment Hours

Or:

Experiment Hours = (GT Particle Flow (ppmw) x Operation Hours)/TADF Particle Flow (ppmw)

It must be noted that the limits of this technique have not yet been tested. Very high particulate loadings tend to form unusual deposits that are dissimilar to real deposits. Thus, a high particulate loading combined with a short test duration may produce unrealistic deposits. Figure 6 illustrates the potential effect of overly high particulate loadings. The deposits found immediately adjacent to the surface had a realistic

11

appearance and structure, but the deposits farthest from the surface were exceptionally thick and brittle with a glassy surface appearance and a highly porous internal structure. The coupon shown in Figure 6 was intended to represent approximately 10,000 hours of operation with a GT particle flow of approximately 0.09 ppmw (900 ppmw-hrs). Therefore, the coupon was exposed to a high particulate loading of 221 ppmw for a period of 4 hours (884 ppmw-hrs).
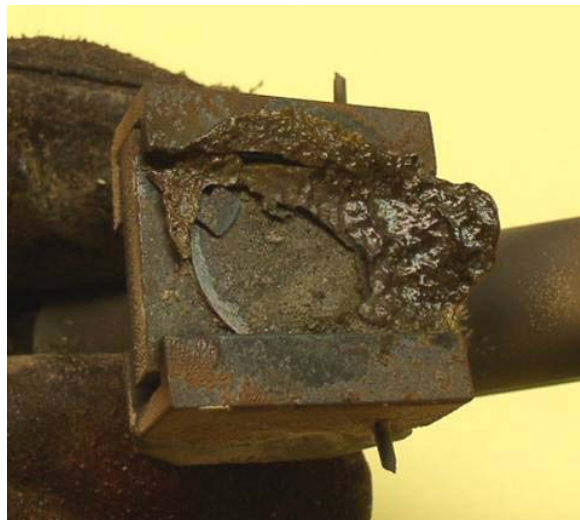
Figure 6. Photograph of accelerated deposits produced by a very high particulate loading.

Although such unusual deposits were not always produced by particulate loadings of a magnitude similar to that which formed the deposits seen in Figure 6, for this study, particulate loadings were significantly lower: on the order of 43 ppmw-hrs per test for a cumulative 172 ppmw-hrs through the standard series of four tests.

The particle flow introduced into the TADF for this study consisted of dust that was extracted from the atmosphere in Arizona by Air Filter Testing Laboratories, Inc. This

dust meets the particulate size standards of ASHRAE (American Society of Heating,

Refrigeration, and Air Conditioning Engineers). Since the dust was taken directly from

the air, it has the same composition as particles that would have been drawn into a gas

turbine located in the same region. Therefore, this facility is able to produce deposits with

realistic chemical characteristics. Table 2 presents the chemical composition of the

particulate used in the Turbine Accelerated Deposition Facility for the current study. The

crustal composition of the earth as determined by Ford, 1954 is compared to the

composition of the Arizona dust as determined by Air Filter Testing Laboratories, Inc.

and as determined at BYU with X-ray spectroscopy. Figure 7 presents the size

distribution of the particulate used for the current study as a percentage of total mass.

Table 2. Chemical composition of particulate used in the Turbine Accelerated Deposition Facility.

	Crustal Composition (Ford, 1954)	Manufacturer Assay of Seed Particulate	BYU SEM Assay of Seed Particulate
SiO_2	59.8	68.5	60.2
Al_2O3	14.9	16	4.5
CaO	4.8	2.9	13.7
MgO	3.7	0.8	N/A
Other Alkalies	6.2	4.6	7.3
Fe_2O_3	2.7	4.6	10.7
FeO	3.4	negligible	negligible
H_2O	2	0	N/A
Ignition Losses	N/A	2.7	N/A
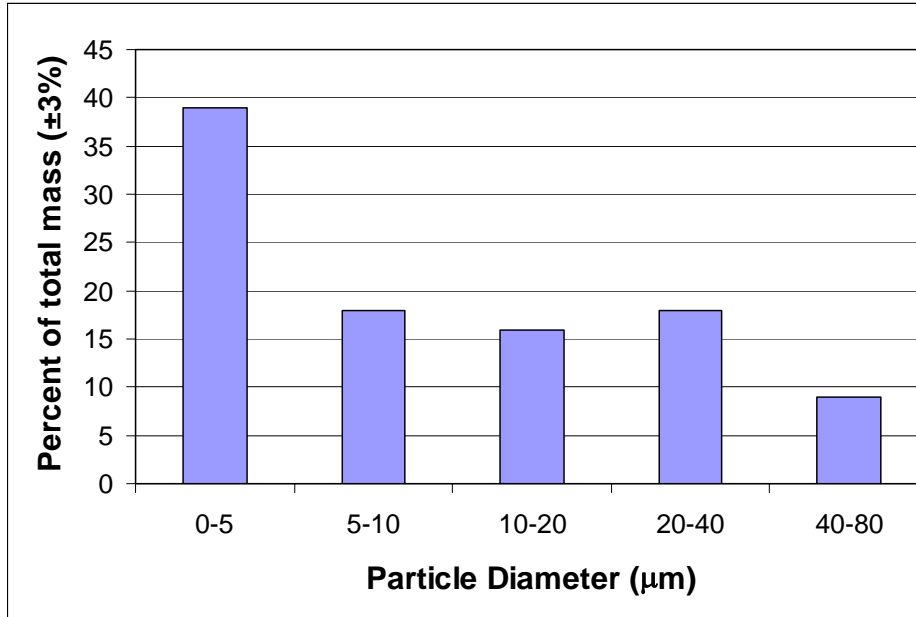
Figure 7. Particle diameter distribution by mass percentage.

2.2   Turbine Accelerated Deposition Facility

As mentioned above, the facility used to produce accelerated deposition is a highly

specialized natural gas-fueled combustor that reproduces the thermal and aerodynamic

conditions found at the first stage turbine blades in a gas turbine engine. This involves a

stream of combustion byproducts striking a turbine blade (or turbine blade coupon) at a

freestream temperature ranging from 1150°C-1200°C and a Mach number of

approximately 0.31. However, unlike the first stage of a gas turbine, the static pressure

within the TADF does not far exceed atmospheric pressure. As has been done by other

authors (Tabakoff et al., 1995; Wenglarz & Fox, 1990), no attempt was made to

reproduce the static pressures found in a real gas turbine with the TADF. These and other

authors (Borom et al., 1996; Kim et al., 1993) maintain that deposition rates are not a

function of static pressure. From the above studies and Jensen's research, it can be

concluded that those parameters that are considered to be necessary for simulation of real

deposition are:

- Temperature—As mentioned in Chapter 1, deposition tends not to occur at temperatures below which the particulate changes phase.
- Flow Velocity—In order to properly simulate the conditions inside a gas turbine, particulate should strike the coupon surface with a momentum that is comparable to that found in a real gas turbine.
- Particulate Concentration—As illustrated by Figure 6, overly high particulate concentrations can result in unrealistic deposits.

2.2.1 TADF Operation

During operation, a horizontal stream of air is introduced into the base of the TADF. This

stream is diffused within a region filled with 1.3 cm-diameter marbles to ensure that the

flow is evenly distributed across the entire 30.5 cm-diameter base of the facility. The

diffused flow, now following a vertical path, is straightened by an aluminum honeycomb

and enters the combustion region. Within this region, four upward curving tubes

introduce partially pre-mixed natural gas, which is immediately ignited. A quartz

viewport allows visual monitoring of the flame. The viewport is kept clear of particulate

and soot by use of a purge that is fed by air bypassed from the main line. See Figure 8 for

details.
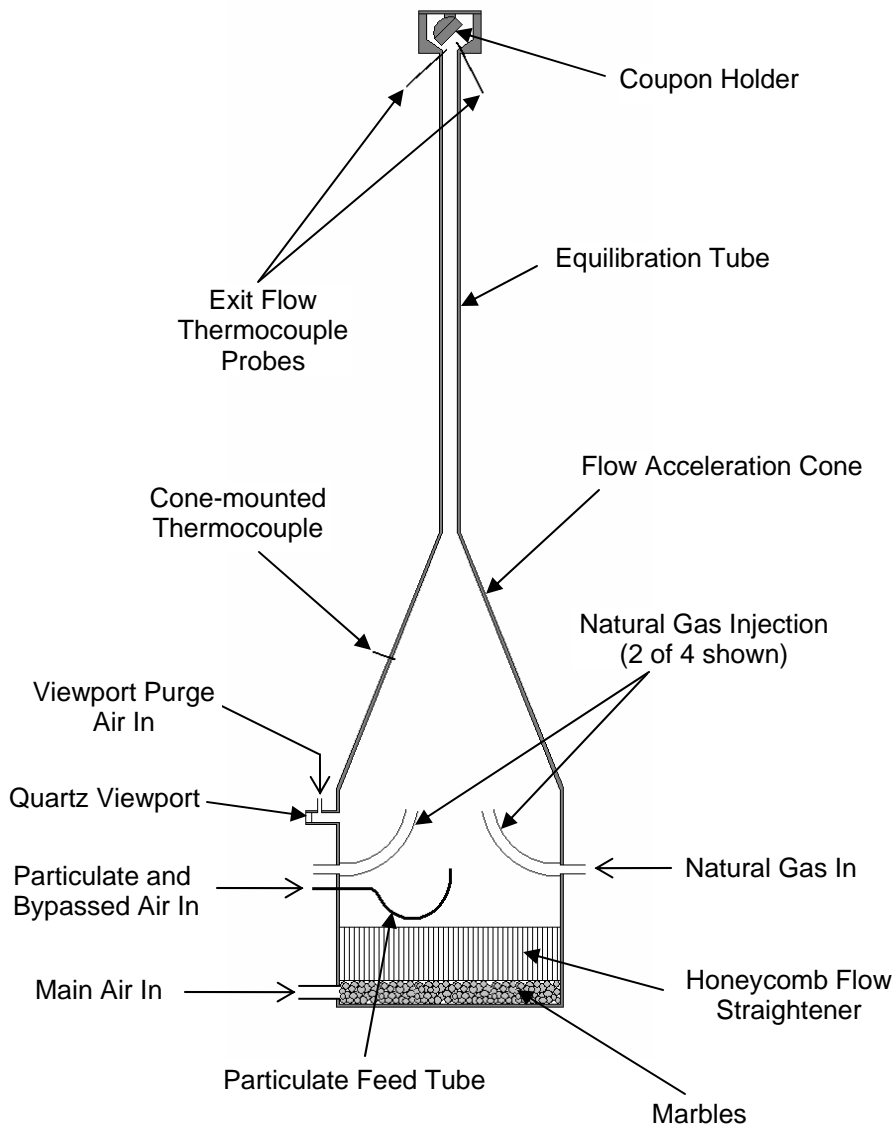
Figure 8. TADF cross-sectional schematic.

Particulate is introduced into the combustor through a line that is bypassed from the

primary air line. This secondary stream passes through a glass bulb into which particulate

is slowly injected with a motor-driven syringe (Figure 9). The particulate is entrained into

the flow and is sent into the combustor through a tube that enters the combustion region.

This tube initially curves downward, so as to keep it sufficiently clear of the flame, and

then upward. The particulate laden flow, now mixed with the hot exhaust gases, passes

through a cone directly above the combustion region which gradually accelerates the

flow. Immediately beyond the cone, the flow passes through a 1 m long equilibration tube

with a 1.58 cm inner diameter. The tube length was determined by the length of time it

would take to bring a 40 μm particle up to the freestream temperature and velocity of the

exit flow under test conditions (Jensen, 2004). At the exit, the flow velocity is

approximately 220 m/s (Mach 0.31). This value is typical of the inlet flow Mach number

experienced by first stage high pressure (HP) turbine blades and vanes during operation.
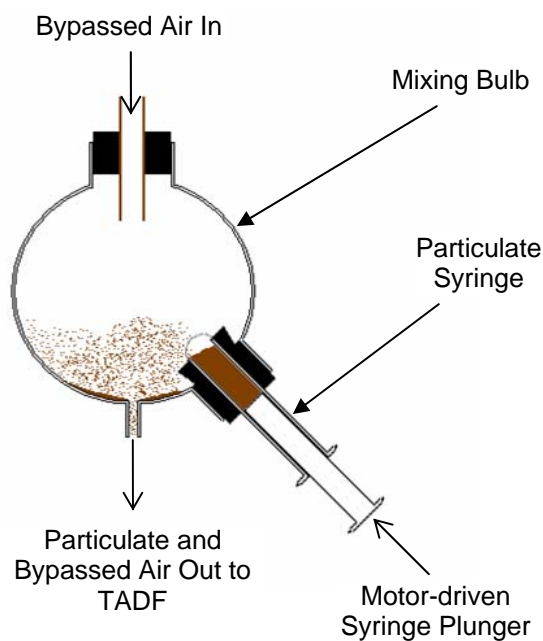
Figure 9. Cross-sectional schematic of particle-feed system.

The tube terminates into a cup-shaped region within which a turbine blade coupon is

held. The coupon holder is located approximately 2 to 3 jet diameters above the exit of

the equilibration tube. At this point, the freestream temperature, which is between 1150ºC and 1200ºC, matches that found in the first stage of G-class gas turbines.

The coupon holder is capable of being positioned at an angle of 30, 45, or 90°. For the current study, an angle of 45° was decided upon due to the discovery by Jensen that the statistical roughness factors *Ra* and *Rt* peaked in experiments where the coupon was held at an angle 45° to the flow (Jensen, 2004). Additionally, of the three available angles, 45° ensures that the greatest possible area would be exposed to parallel flow rather than impinging flow. This was favorable since the convective heat transfer experiments were performed with a heated stream of air flowing parallel to the surface. A FLUENT simulation was used to determine how the exit gases flowed over the coupon and holder (Figure 10). The simulation showed that the location of the stagnation point was below the region where roughness measurements were taken.
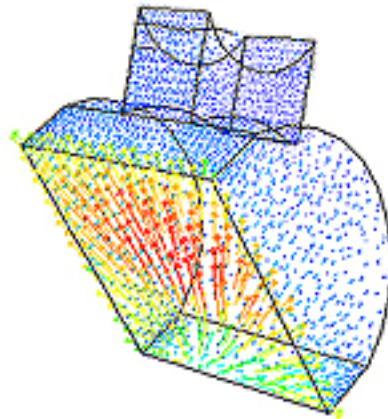
Figure 10. FLUENT produced vector diagram for the TADF sample holder.
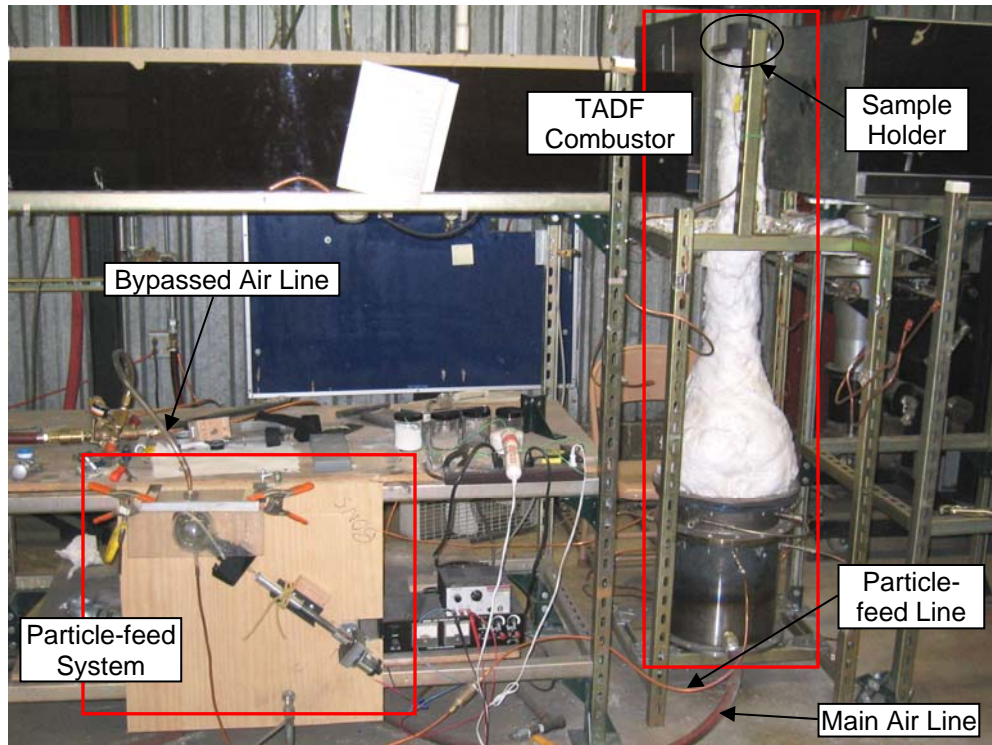
Figure 11. Brigham Young University TADF facility in building B-41.

2.2.2 Instrumentation

Air flow into the TADF is determined through the use of a choked flow orifice plate mounted to the main air line that is controlled using a Valtek actuator. The output of the pressure transducer mounted on the upstream side of the orifice plate is routed through a National Instruments SCXI chassis. Additionally, a K-type thermocouple is mounted near the orifice plate, giving the temperature of the incoming air. These pressure and temperature data are monitored by the LabVIEW VI program, and are used to determine the mass flow rate of the air. The natural gas flow rate is measured with a rotometer with an attached pressure gauge. This flow rate is adjusted throughout the course of an experiment in order to maintain the desired exit temperature, although it is generally 3.7% of the air mass flow rate.

19
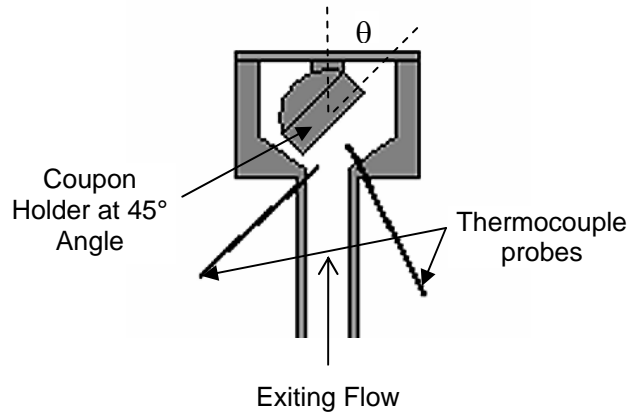
Figure 12. Cross-sectional schematic of TADF sample holder.

The exit temperature is measured by two 0.8mm diameter Super OMEGACLAD K-type thermocouple probes capable of continuous use at 1150°C protruding into the flow (Figure 12). The probes are connected to a National Instruments NI SCXI-1112 thermocouple module mounted in an NI SCXI-1000 chassis. The temperature data at the exit is passed to the same LabVIEW VI program as the main air pressure and temperature data. Finally, the LabVIEW VI program calculates the total mass flow rate. The mass flow rate, the data from thermocouple probes, and the cross-sectional area of the TADF exit nozzle are used to calculate the flow Mach number using the Ideal Gas Law relation for the speed of sound (Equation 1). The specific heat ratio used was that for combustion in air (γ=1.3) while the gas constant was approximated as being the same as the value for air (i.e. R=287 J/kgK).

$$M = \frac{\dot{m}}{\rho_{gas} A_{exit} \left(\sqrt{\gamma RT} \right)_{gas}} \tag{1}$$

2.2.3   TADF Modifications

The TADF as designed by Jensen was modified in several ways for this project. First it was found that the diffusion flame originally used within the combustor led to a problem with incomplete combustion. To correct this, the air and natural gas lines were modified to allow for partial premixing of the fuel. Because this modification increased the velocity of the gas entering the TADF through the straight, horizontal fuel injection nozzles, there was a tendency for the flame to impinge on the sides of the combustor. In response, larger diameter nozzles which curved upward toward the cone of the TADF were installed as shown in Figure 8.

Second, the flow Mach number at the exit of the TADF was originally determined prior to an experiment, requiring that the air flow and exhaust temperature be maintained within strict parameters during the course of the experiment so as to achieve that Mach number. The air flow rate was monitored using a Fluke Multimeter which read the output voltage from the pressure transducer mounted immediately upstream of the orifice plate while the incoming air temperature was read by a pyrometer. Under this setup, only the temperature of the flow exiting the TADF was recorded in real time. For the current project, the pressure transducer output and main air thermocouple output were routed through the National Instruments SCXI chassis and passed to a modified version of the LabVIEW VI program used by Jensen in order to calculate the real time mass flow rate. Further modifications of the VI allowed for a real time calculation and recording of the exit flow Mach number.

Third, bare wire S-type thermocouples which used ceramic sheathing for support were replaced with the Super OMEGACLAD K-type thermocouple probes. It had been discovered that the brittle ceramic sheathes tended to develop deposits over the course of an experiment, which often led to them breaking off under the aerodynamic load. Although the thermocouple probes also developed deposits, their malleability prevented them from breaking while also allowing for the removal of deposits between tests without suffering damage. The amount of deposits that formed on the probes over the course of a test was not sufficient to cause a noticeable change (i.e. a change larger than $\pm 5°C$) in the measured temperature.

Finally, to allow for a more consistent rate of particulate feeding and to increase the level of automation of the TADF, the hand-cranked particle feed system originally mounted was replaced by a motorized one. In addition, the larger syringe used by Jensen was replaced by a smaller diameter syringe to allow for the lower particulate loading used for this project.

2.3   Turbine Blade Coupons

The TADF is designed to form deposits on turbine blade coupons rather than actual turbine blades. These coupons—which are constructed of the same materials as those found in real turbine blades and are coated in the same manner—are used by turbine blade manufacturers for various testing purposes. The particular specimens used for this project were flat, circular disks with a diameter of approximately 2.54 cm. Like real turbine blades, the coupons consist primarily of a nickel-cobalt substrate. Three types of

coupons—one with an unpolished oxidation resistant coating, one with a polished bare

metal surface, and one with an oxidation resistant coating and a polished overlying

thermal barrier coat (TBC)—were used in the current study (Figure 13). The TBC was air

plasma-sprayed, yttria stabilized zirconia (YSZ). These coupons were obtained from

several manufacturers of gas turbine components.
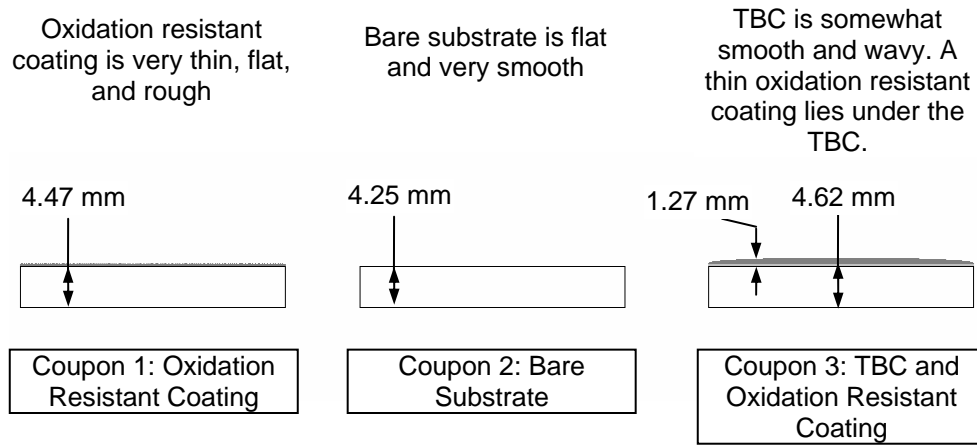
Figure 13. Cross-sectional drawing of coupons.

2.4   Deposition Evolution

Until recently the TADF had been used solely to demonstrate the concept of accelerated

deposition and to produce deposits for thermal conductivity experiments. These prior

experiments used particle loadings and experiment time periods that recreated the amount

of deposit that would be expected on a turbine blade that has undergone a full cycle

between maintenance periods. However, not only is the final state of a turbine blade of

interest, but also the intermediate states of the blade as it experiences deposition

conditions. Thus, each coupon used in this study underwent four cycles (hereafter

23

referred to as "burns") in the TADF, each simulating approximately three months of operation, to produce a total of one year's worth of deposition.

2.4.1 Burn Procedures

During a burn, each coupon experienced approximately 45 minutes of warm-up time, during which the TADF was brought to an operational freestream temperature of between 1150ºC and 1160ºC. Once steady state had been reached, particulate was introduced into the facility. This particulate flow was maintained for a period of two hours after which it was closed off. The gas lines to the TADF were then shut off. The coupon was allowed to cool for several hours, after which it was removed from its fixture. Upon removal, the coupon was placed in another fixture and held firmly in place by four screws while topological measurements were taken. Following this process, the coupon was photographed and carefully stored until the following burn.

2.4.2 Coupon Surface Analysis

The surface of the coupon was analyzed with a Hommel Inc. T8000 profilometer equipped with a TKU600 stylus. The Hommel profilometer runs the stylus across the surface of a sample, taking height data at a user-defined number of points during its traverse. This direction of motion is defined as the x direction. Once a traverse has been made, the profilometer returns to its start position (i.e. x=0) and steps a certain distance in the y direction, which is also user defined. The profilometer then repeats this process until the predetermined number of steps has been made. The profilometer was set to

measure a region located roughly in the center of the circular coupon, 20 mm x 7.99 mm

in size. Approximately 2000 measurements were made in the x direction with each

traverse for a Δx of approximately 10 μm. Exactly 800 steps in the y direction were made

with a Δy of 10 μm.
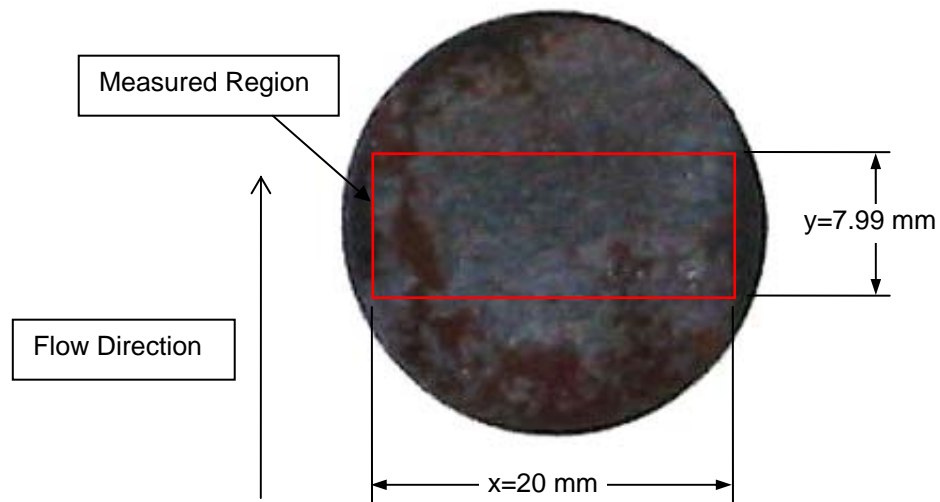
Figure 14. Illustration of coupon measured region and flow direction.

The measurements were recorded as text files containing x, y, and z coordinates. The

surface topology of the coupon was measured five separate times: one measurement of

the clean surface prior to any deposition and one measurement after each of the four

burns in the TADF. Topological maps, three-dimensional surface representations, and

roughness statistics were produced with the Hommelwerke Hommel Map software.

Chapter 3: Deposition Evolution Results

3.1   Roughness Measurement

For this study, a statistical evaluation of the roughness of the deposits formed by the

TADF was an essential element in describing the evolutionary process as well as

predicting the convective heat transfer properties of each surface. Four statistics in

particular were utilized: Ra, Rq, Rz, and $\overline{\alpha_f}$. The first three parameters are evaluated by

the Hommelwerke software. These values generally describe the unevenness of the

surface. The parameters Ra and Rq are defined as follows:

$$Ra = \frac{1}{NM} \sum_{x=0}^{N-1} \sum_{y=0}^{M-1} \left| Z_{x,y} \right| \tag{2}$$

$$Rq = \sqrt{\frac{1}{NM} \sum_{x=0}^{N-1} \sum_{y=0}^{M-1} Z_{x,y}^{2}} \tag{3}$$

In a two-dimensional calculation, Ra is a measurement of the area bounded by the

roughness surface profile and the mean line of the roughness height. This area is then

divided by the evaluation length N. In a three-dimensional calculation, which is the type

of evaluation used in this project, the area is calculated along two dimensions and is

divided by both evaluation lengths N and M. Rq is similar to Ra but is an rms value.

As defined by the Hommelwerke software, the value of Rz is the mean of the vertical distance between the five highest peaks and five deepest valleys within a neighborhood of a given size. This statistic is often used to approximate the average roughness height k, which is the average distance between the peaks and valleys of a surface. The fourth parameter mentioned, $\overline{\alpha_f}$, is the average forward facing angle (Figure 15). It was determined for each surface with a MATLAB program written for that purpose. The average forward facing angle gives a sense of the peakedness of the surface. This is useful since equal Ra values can be obtained with very different surfaces. A surface dominated by pointed cones may have the same Ra value as one that is covered with hemispheres. Ra in conjunction with $\overline{\alpha_f}$ can describe a surface in great detail.

Additionally, Bons developed a correlation for determining the Stanton number of a surface which involves the forward facing angle (Bons, 2005).
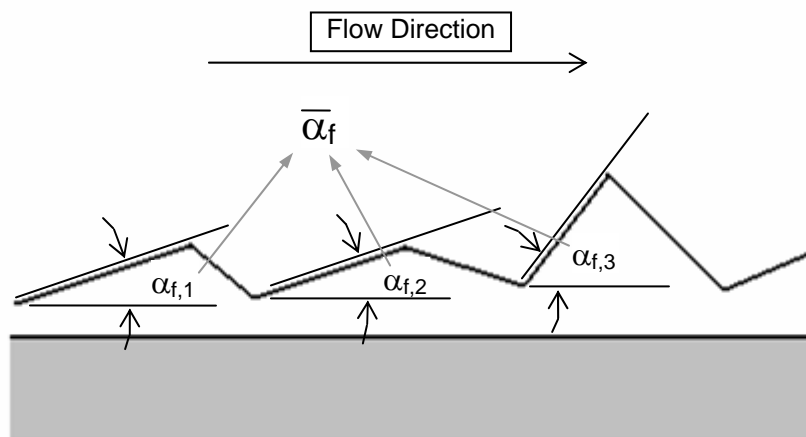
Figure 15. Surface roughness forward facing angle.

Surface roughness becomes important in cases where the surface is in contact with a turbulent moving fluid. Rougher surfaces—especially those with higher average forward facing angles—generally produce higher friction coefficients and rates of convective heat transfer. It has been shown through experimentation that:

$$c_f = f(k_s, \text{Re}) \tag{4}$$

$$St = f(k_s, \text{Re}) \tag{5}$$

where k_s is a parameter known as the sandgrain roughness. The sandgrain roughness correlates the average roughness height of a surface, k, with a sand-coated surface that has an average roughness height of k_s which produces the equivalent effect. It has also been shown that k_s can be related to various roughness statistics:

$$k_s = f(Ra, k, \overline{\alpha}_f) \tag{6}$$

3.1.1 Form Removal

While Coupons 1 and 2 were found to be flat, the TBC coating of Coupon 3 had a noticeable degree of curvature. Such a curvature causes streamlines flowing over the surface to curve, remaining tangent to the surface. Because the surface roughness that affects the flow should be measured with respect to a meanline that runs parallel to the flow, either the meanline must be curved or the surface must be flattened. Therefore, a form removal function available in the Hommelwerke software was used prior to determining the surface roughness statistics. Whereas Coupons 1 and 2 were nearly flat,

29

Coupon 3 had a curved surface similar to those seen on other TBC coated coupons used in projects related to the current one.
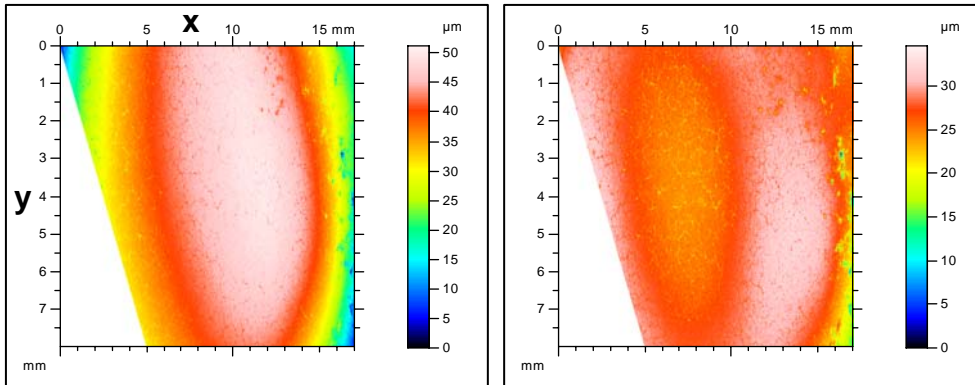
Figure 16. Topological map showing the preburn surface curvature Coupon 3 prior to (left) and following (right) a second order form removal.

A second order form removal was therefore used to reduce the curvature prior to roughness analysis (Figure 16).

3.1.2   Data Drop-out Error

A defect that was discovered in the Hommelwerke profilometer measurements for Coupon 3 Burns 1 through 4 is believed to have been caused by data drop-out error. This error was caused by a short in the data transfer cables which resulted in an interruption in the signal being sent from the profilometer stylus. Whenever this occurred, the data would be smeared—data from a previous point would be used in place of the gap. Thus, a discrete point would be seen as a short line (Figure 17). These lines originally occurred parallel to the motion of the stylus. A 15° rotation to align the flow direction with the y-axis has given the lines a 15° angle from the horizontal.

30

This error was found to be more prevalent in the lower left-hand regions of the measurements where there were smaller height variations in the surface. Inspections of the models produced using the surface data showed that since the error occurred in those particular regions, it had a minimal effect on the overall roughness of the models. Additionally, measurement of a profilometer calibration surface with a *Ra* value of 3.02 µm gave a value of approximately 3.05 µm, indicating that the effect of the error on measurements of the surface was small.
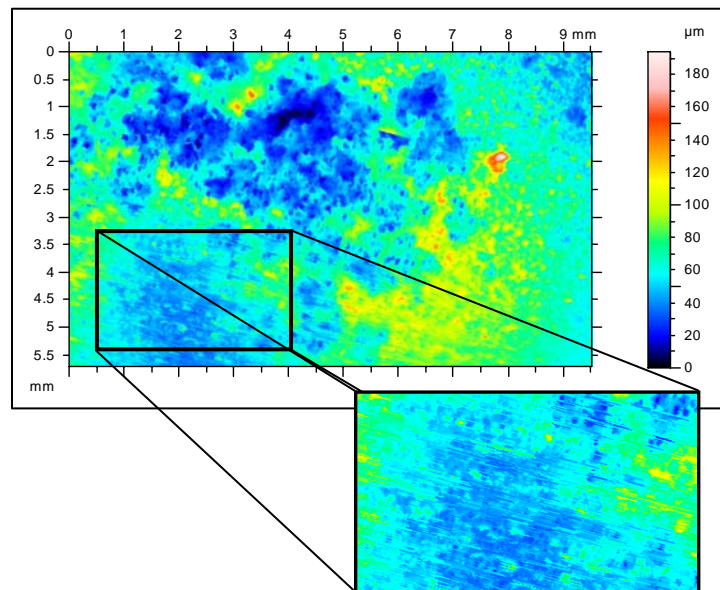
Figure 17. Illustration of data drop-out error.

3.1.3 Coupon Analysis

As mentioned in Chapter 2, deposits were evolved on three coupons: one with oxidation resistant coating, one with a bare substrate surface, and one with TBC coating. In this chapter the three coupons are analyzed. In all analyses the left and right edges of the measured region are omitted. This is due to the presence of large deposits that form at the

interface between the coupon surface and the edges of the coupon holder. These deposits are ignored in this study since they are not representative of the deposits that form on the free surface of a coupon.

3.2   Coupon 1: Unpolished Anti-Oxidation Coating

The surface of the first coupon was coated with an unpolished anti-oxidation layer, making the surface rougher than that of a typical new turbine blade. The coupon underwent four sequential burns, each lasting two hours, under similar temperatures and particulate loadings (Table 3). Topological measurements were made following each burn. The deposits showed little or no evidence of flaking after the coupon was removed from the TADF. Although topological maps and three-dimensional representations of Coupon 1 show deposition occurring during each burn (Figure 18 and Figure 19), the surface does not become increasingly rougher with each experiment. In fact, the value of *Ra* decreased from one test to the next in all but one case (see Figure 20). It is believed that this behavior was caused primarily by the initially high level of roughness of the coupon surface. Given the large number of peaks on the preburn surface, there were few locations where new peaks could be formed but a large number of regions where valleys could be filled in. Additionally, the average forward facing angle experiences only a single slight rise between Burns 2 and 3. Otherwise, the angle decreases steadily. This would tend to reduce the convective heat transfer between the surface and the freestream over time (see section 5.1.4).

Table 3. TADF experimental settings for Coupon 1 (Oxidation Resistant Coating).

Burn	Temperature (C)	Simulated Parameters		ppmw-hrs	Test Parameters	
		Time (hrs)	ppmw		Time (hrs)	ppmw
1	1160	2619	0.02	52.37	2	26.19
2	1155	2192	0.02	43.85	2	21.92
3	1155	2436	0.02	48.72	2	24.36
4	1160	2436	0.02	48.72	2	24.36

Considering that between the preburn surface and the Burn 4 surface, the value of Ra

increased by only 0.6%, the value of Rq increased by only 6.4%, and the value of $\overline{\alpha_f}$

decreased by 53.5%, it is unknown at which point a trend of increasing roughness would

be seen. It is known that Jensen, who used several coupons from the same lot as

Coupon 1, was able to obtain a surface roughness that was significantly higher than that

of the preburn surface (Jensen, 2004). This is most likely due to the fact that Jensen used

a much higher particulate loading than was used in this study. It is possible that higher

particulate loadings per test, or more burns, would have eventually produced increasingly

rougher surfaces.

Although it did not follow the expected trend, Coupon 1 did serve to show that the TADF

could produce deposition evolution. It also indicated that the preburn roughness of the

surface may have a strong effect on the surface roughness after exposure to deposition

conditions. Later analysis would show that a period of a similar evolutionary behavior

occurred during the simulated operational cycles of Coupons 2 and 3 (Figure 32).
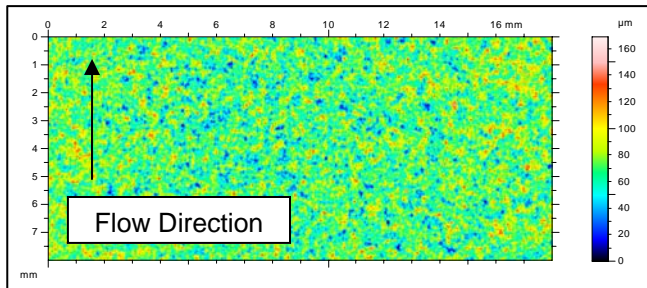
Figure 18a. Topological map of Coupon 1 prior to exposure to deposition conditions (Preburn).
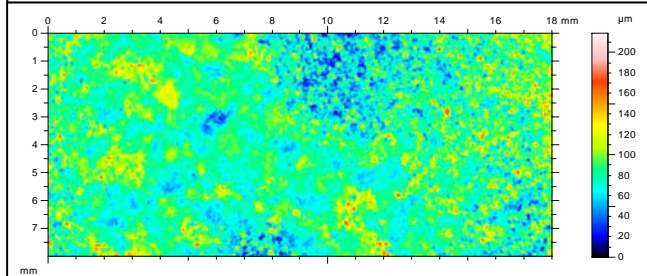
Figure 18b. Topological map of Coupon 1 following Burn 1.
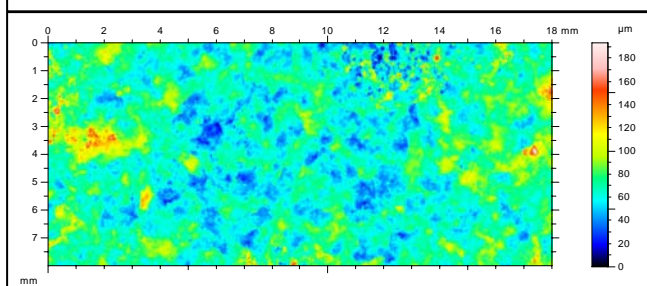
Figure 18c. Topological map of Coupon 1 following Burn 2.
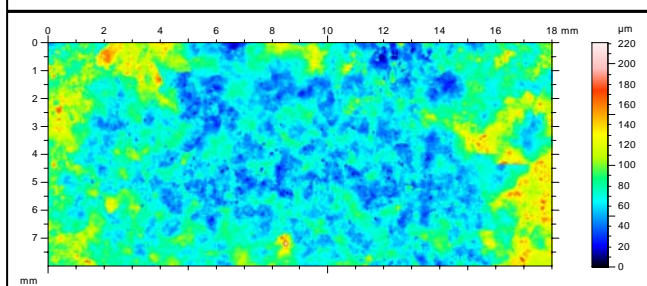
Figure 18d. Topological map of Coupon 1 following Burn 3.
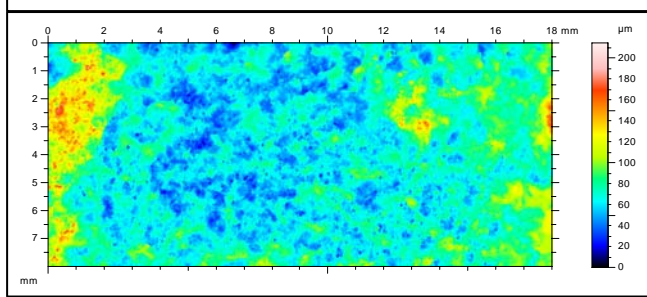
Figure 18e. Topological map of Coupon 1 following Burn 4.

Figure 18. Topological representations of deposits on Coupon 1 (Oxidation Resistant Coating).
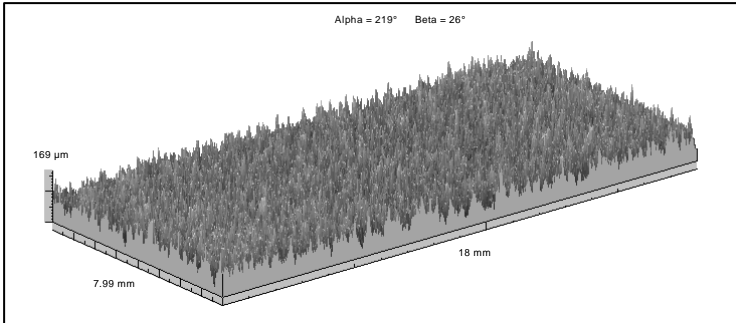
Figure 19a. Three-dimensional representation of Coupon 1 preburn.
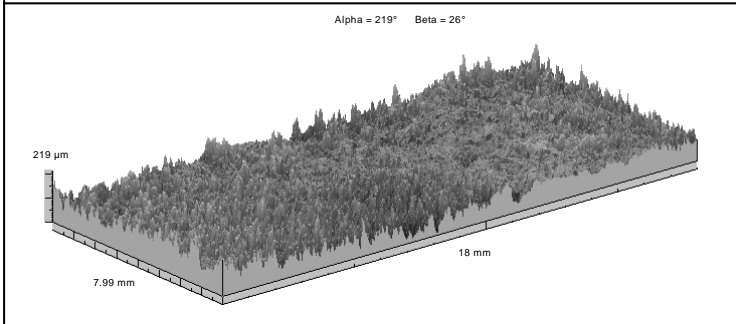
Figure 19b. Three-dimensional representation of Coupon 1 Burn 1.
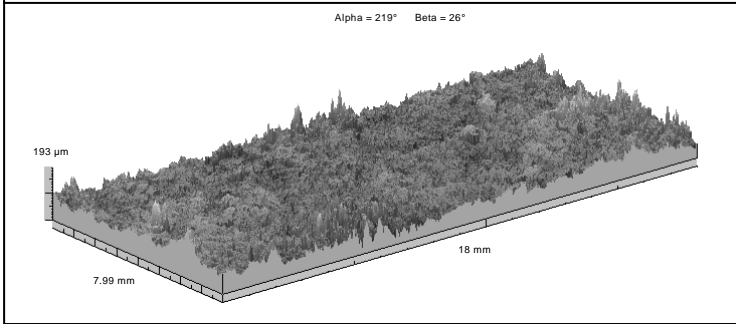
Figure 19c: Three-dimensional representation of Coupon 1 Burn 2.
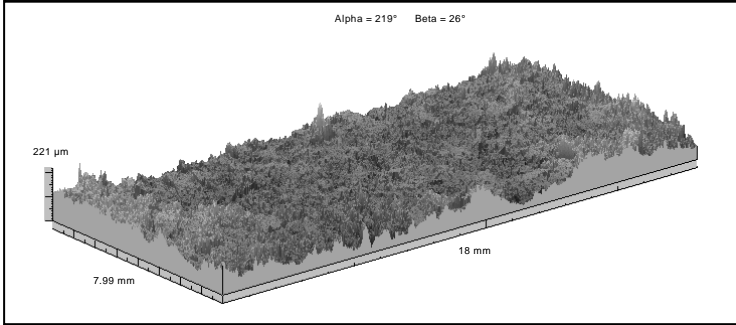
Figure 19d. Three-dimensional representation of Coupon 1 Burn 3.
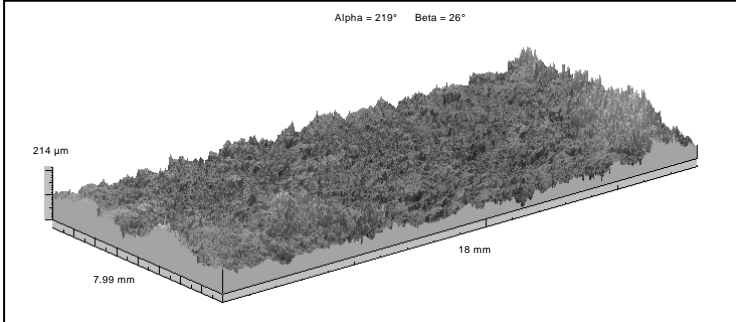
Figure 19e. Three-dimensional representation of Coupon 1 Burn 4.

Figure 19. Three-dimensional representations of deposits on Coupon 1 (Oxidation Resistant Coating).
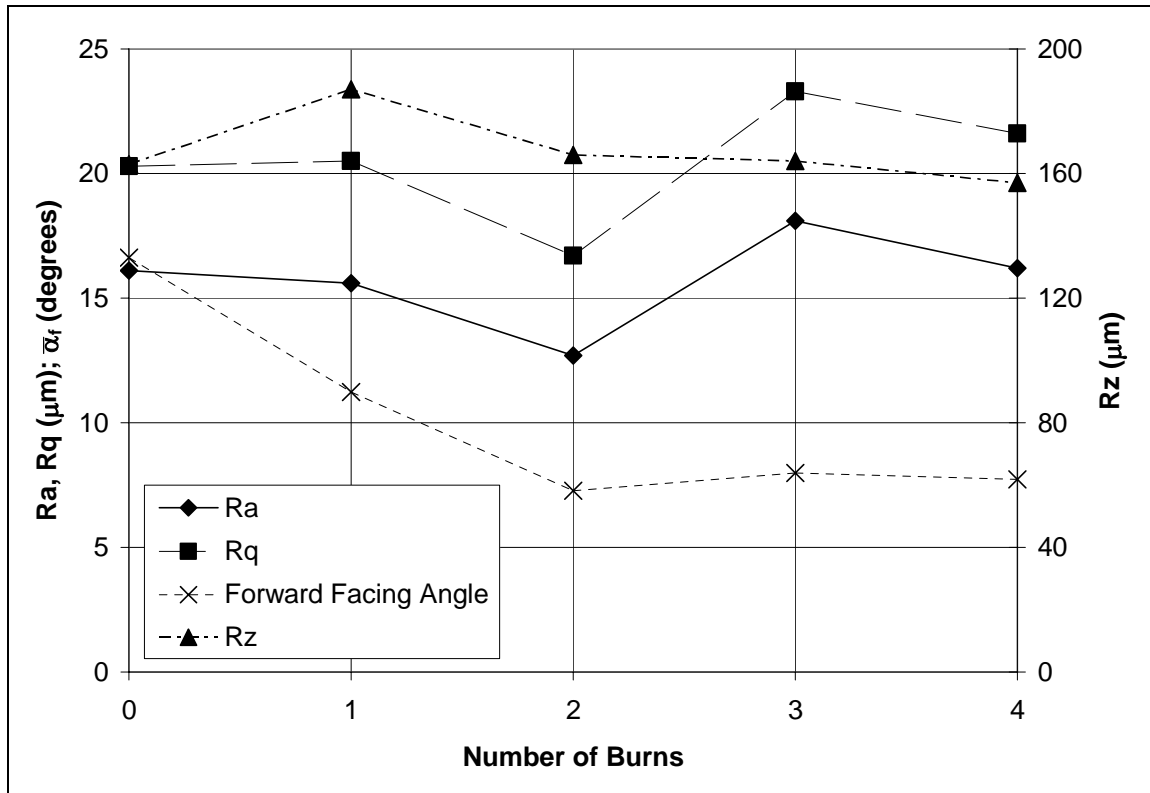
Figure 20. Plot of roughness statistics for an 18 mm x 7.99 mm area of Coupon 1.

3.3   Coupon 2: Polished Bare Metal Substrate

The second coupon had a highly polished surface, making it smoother than that of a typical new turbine blade. Coupon 2 experienced essentially the same deposition conditions as Coupon 1 (Table 4). However, Coupon 2 experienced a high degree of flaking, with large regions of bare substrate or deposits from previous burns being exposed when the overlying deposits would flake off after removing the coupon from the TADF. This flaking is believed to be caused by differing thermal coefficients of expansion. As the coupon cools and contracts, the deposits are put under stress and respond by flaking off. This process is often quite active, with flakes of deposit springing off the surface, sometimes making an audible sound. After several hours of cooling,

flakes would often be found several inches away from the coupon. See section 3.3.7 for a discussion of deposit flaking.

Due to the complication introduced by the flaking off of deposits, two approaches were taken in analyzing the roughness characteristics of Coupon 2. In the first approach, presented in sections 3.3.1 through 3.3.6, the surface roughness statistics were evaluated based on the overall surface. In the second approach, presented in sections 3.3.8 through 3.3.11, a smaller portion of the overall measured surface was studied from burn to burn. The portion selected consisted of a region where deposit flaking appeared to be minimal (Figure 21). Representing three consecutive burns that produced long-lasting deposits, it was believed that this magnified region would best represent the surface that Coupon 2 may have had if widespread flaking of deposits had not occurred.
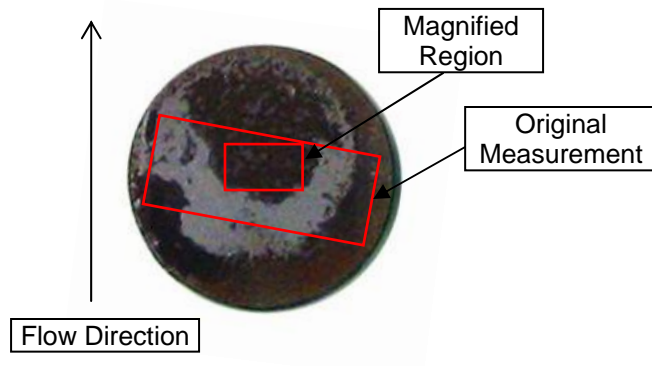
Figure 21. Illustration of location of surface measurement and magnified region.

3.3.1 Coupon 2, Preburn—Overall Surface

Figure 22a and Figure 23a show the topological features of Coupon 2 prior to TADF testing. The image has been rotated so as to align the y-axis of the topological map and the flow direction. Additionally, the leftmost and rightmost sides have been cropped. This is to exclude the ridges of deposits that form at the edges of the coupon holder from the roughness analysis.

Table 4. TADF experimental settings for Coupon 2 (Bare Substrate).

Burn	Temperature (C)	Simulated Parameters		ppmw-hrs	Test Parameters	
		Time (hrs)	ppmw		Time (hrs)	ppmw
1	1154	2192	0.02	43.85	2	21.92
2	1154	3410	0.02	68.21	2	34.1
3	1157	2631	0.02	52.62	2	26.31
4	1150	2558	0.02	51.16	2	25.58

3.3.2 Coupon 2, Burn 1—Overall Surface

Following Burn 1, the coupon was allowed to cool within the TADF for three hours. At the time of removal, the sample was found to be almost entirely coated in deposits. To the naked eye, the coating appeared to be nearly uniform. Since flaking deposits can affect the results given by the Hommel profilometer, the coupon was left to cool further before the coupon surface was measured. During this time, a large portion of the deposits in the region at the top center of the measured area flaked off, leaving the surface seen in Figure 22b and Figure 23b. It is believed that the deposits remaining are representative of the deposits that were removed.

3.3.3 Coupon 2, Burn 2—Overall Surface

As with Burn 1, approximately three hours after the TADF was shut down, the sample was removed. The sample was found to be almost entirely coated in deposits with a visible discontinuity along the edges of the top center region where deposits had flaked off following the first burn. As the coupon was allowed to further cool for several hours, a large portion of the deposits flaked off, leaving the surface seen in Figure 22c and Figure 23c. Flaking after Burn 2 appeared to occur primarily in the regions where deposits had previously remained following Burn 1 whereas the most tenacious deposits resulting from Burn 2 occurred in the region where deposits had flaked off following Burn 1. This resulted in a topology that is a near mirror opposite of that obtained following the Burn 1. Some flaking appeared to have occurred in those regions that remained covered by deposits, although the flaking was not extensive enough to uncover the substrate. Much of this lighter flaking continued to occur for days after the burn and the subsequent measurement with the Hommel profilometer.

3.3.4 Coupon 2, Burn 3—Overall Surface

Unlike the previous burns, the majority of the deposits produced during Burn 3 remained attached to the surface. It is notable that by this point the majority of deposits produced during Burn 1 had almost completely flaked off, with the exception of two small regions at the edges of the measured area (Figure 22c). Therefore, despite having experienced three burns by this point, because the deposits from Burn 1 flaked off, but not those from Burns 2 and 3, the highest region on the coupon—the top center region—shows only two burns worth of deposition accumulation. Likewise, since the deposits from Burns 1 and 2

39

in the region surrounding the top center region simultaneously flaked off following burn two, those regions show only one burn worth of accumulation. Some light flaking occurred in some of the thinner deposit layers following topological measurements of this surface.

3.3.5   Coupon 2, Burn 4—Overall Surface

Like the preceding burn, Burn 4 produced lasting deposits. Although some light flaking occurred over much of the surface, only a thin layer of deposit was removed, leaving behind the thick deposit layer underneath it (Figure 22e). The fact that the majority of the deposits that were initially laid on the polished, unoxidized substrate surface had since flaked off, whereas those deposits that formed on the later oxidized surface remained firmly attached, suggests that permanent deposits form much more readily on the oxidized substrate. This was despite the fact that the oxidized surface was only slightly rougher than the unoxidized surface (see section 3.3.6).

3.3.6   Coupon 2 Overall Surface Roughness Trend

The evolution of the overall surface roughness behaved as expected, i.e. the roughness increased continuously (Figure 24). From the preburn to Burn 3, the increase in Ra and Rq is nearly linear, with a noticeably smaller rate of increase between Burns 3 to 4. The average peak-to-valley roughness, Rz, increased by only 3% from Burns 1 to 2. This suggests that the net deposit growth between these two burns was minimal. It is therefore likely that deposit formation and subsequent flaking was the dominant mechanism in

producing the measured increase in *Ra* and *Rq* between Burn 1 and Burn 3. It is notable

that there was relatively little deposit flaking following Burns 3 and 4 and that there was

a 23.8% increase in the magnitude of *Rz* between Burns 3 and 4. It can therefore be

concluded that the increase in roughness from Burn 3 to Burn 4 was primarily due to the

accumulation of deposits rather than the much more dramatic flaking off of deposits from

a nearly uniform coating, as occurred in Burns 1 and 2.

3.3.7   Commentary on Deposit Flaking

It is probable that the smooth metal surface of Coupon 2 facilitated the flaking process,

leading to the dramatic results seen in this study. There was also a noticeable reduction in

flaking once the surface had been oxidized. However, given these results and the light

flaking that occurred during experiments with the Coupon 3, which is coated with a layer

of TBC, it is likely that deposit flaking also occurs with real turbine blades. The coupons

used in this project are constructed of the same material and the deposits formed have

been found to have a similar structure and composition as those formed on real turbine

blades. It can therefore be expected that thermal cycling of a turbine blade will result in

the removal of some surface deposits. Thus, the act of removing a coupon from the

TADF or a blade from a gas turbine will introduce a certain element of error. The surface

measured will not be precisely the same surface that was formed through exposure to

deposition conditions. Unless some method is discovered in which a surface may be

studied in situ and at operation temperatures, it must be recognized that this error is likely

to affect any study involving realistically produced surface deposition.
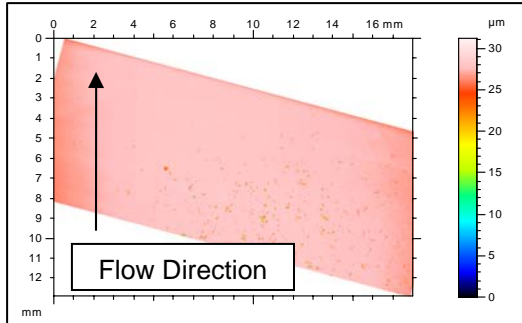
Figure 22a. Topological map of Coupon 2 prior to exposure to deposition conditions (Preburn).
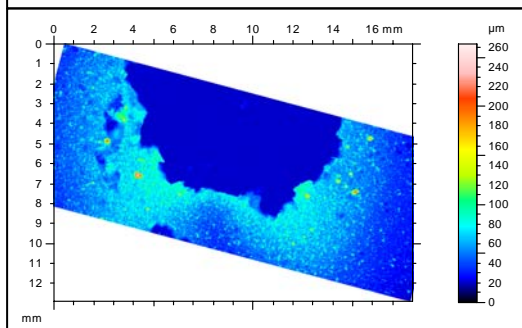
Figure 22b. Topological map of Coupon 2 Burn 1.
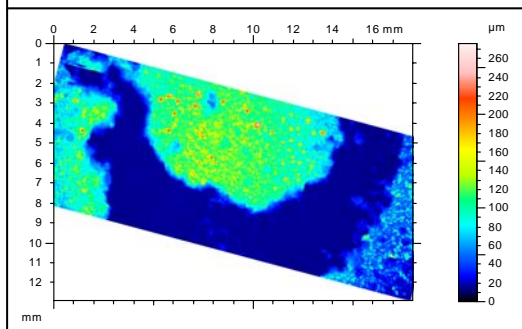
Figure 22c. Topological map of Coupon 2 Burn 2.
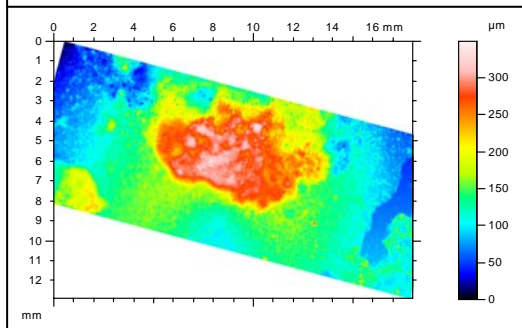
Figure 22d. Topological map of Coupon 2 Burn 3.
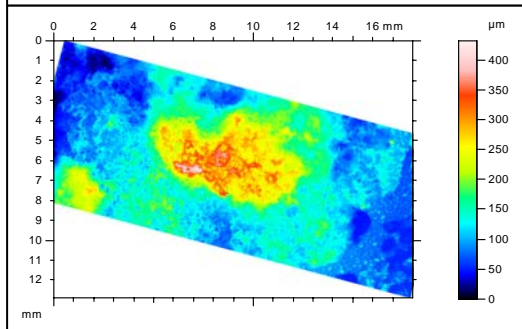
Figure 22e. Topological map of Coupon 2 Burn 4.

Figure 22. Topological representations of deposits on Coupon 2 (Bare Substrate).
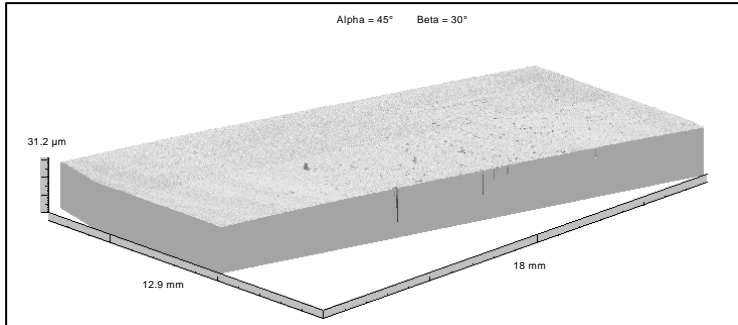
Figure 23a. Three-dimensional representation of Coupon 2 prior to exposure to deposition conditions (preburn).
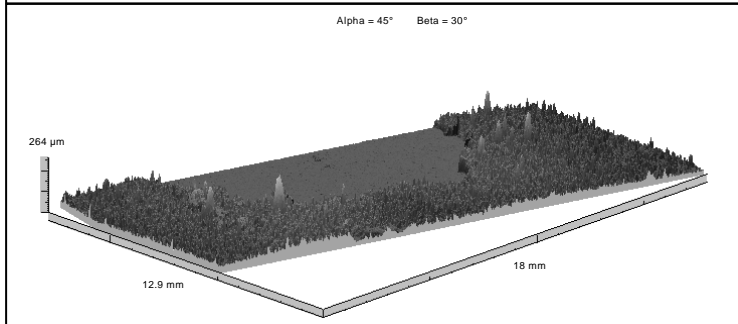
Figure 23b. Three-dimensional representation of Coupon 2 Burn 1.
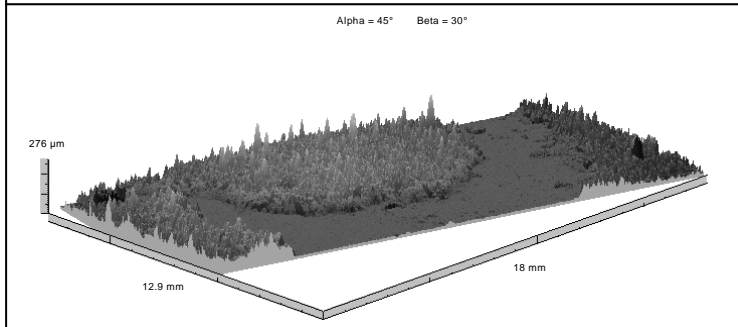
Figure 23c. Three-dimensional representation of Coupon 2 Burn 2.

Figure 23d. Three-dimensional representation of Coupon 2 Burn 3.

Figure 23e. Three-dimensional representation of Coupon 2 Burn 4.

Figure 23. Three-dimensional representations of deposits on Coupon 2 (Bare Substrate).

43
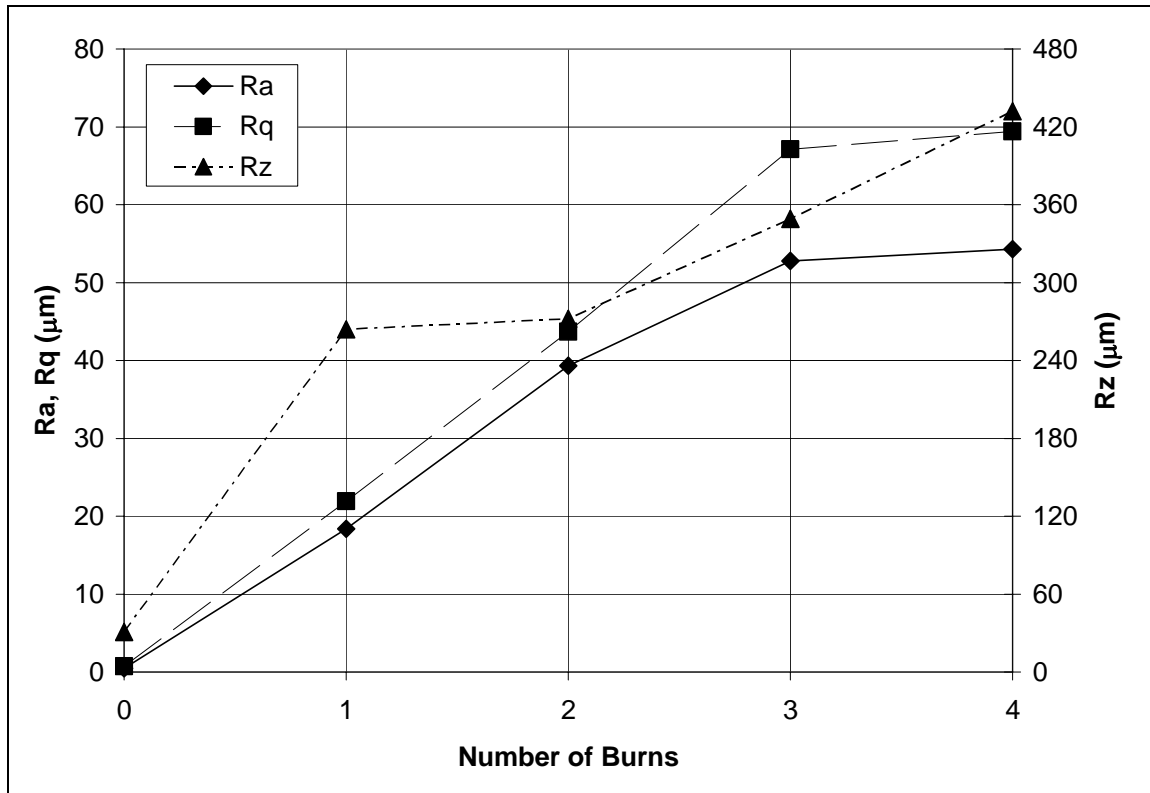
Figure 24. Plot of roughness statistics for the overall surface of Coupon 2.

3.3.8 Coupon 2, Burn 1—Magnified Region

Analysis of the magnified region of Coupon 2 shows that the surface changed little once

the deposits there had flaked off (Figure 25b; Figure 26b). The value of *Ra* increases

from 0.131 μm to 0.467 μm, which is significantly less rough than a polished TBC

surface (Coupon 3), which had a preburn *Ra* value of 2.14 μm. Although there are a few

small peaks, the majority of the surface is a nearly uniform, slightly rough surface. This

newly oxidized surface and its light deposits would form the basis for thick deposits in

later burns. The mean forward facing angle, $\overline{\alpha_f}$, increased slightly from 0.3° to 1.14°

(Figure 27).

3.3.9 Coupon 2, Burn 2—Magnified Region

Burn 2 resulted in a deposit dominated by large peaks of roughness and is similar to that shown in Figure 3 and Figure 26. These peaks led to a large spike in Rz for Burn 2, which exceeded that of the following burn. The values of Ra and Rq also increased significantly, reaching values of 13.3μm and 18.8μm respectively. The value of $\overline{\alpha_f}$ increased to 13.9° (Figure 27).

3.3.10 Coupon 2, Burn 3—Magnified Region

With Burn 3, the valleys between the large peaks from Burn 2 appear to have been filled in, reducing the value of Rz. While some of the peaks produced during Burn 2 may have been broken off during Burn 3, the largest peak appeared to have survived while further deposits built up around the base. The highest peak in Figure 25c, located approximately at x=3.9 mm and y=0.2 mm can also be seen in Figure 25d, surrounded by further deposits.

Burn 3 also marks a distinct change in the surface characteristics. Whereas Burn 2 was dominated by sharp peaks, Burn 3 now has a 'wavy' surface. Tall, distinct peaks have given way to large patches of deposits. The decrease in $\overline{\alpha_f}$ from the 13.9° of Burn 2 to 7.4° for Burn 3 confirms that the surface had indeed become less peaked. Interestingly, despite the vast change in surface appearance, the Ra value increased only 28.6% from Burn 2 to Burn 3; an increase that is much smaller than is seen between any two other burns. This effect may be similar to that seen in Coupon 1, in which the valleys between

45

tall, sharp peaks were filled in with deposits, changing a peak-dominated surface into a 'wavier' one.

3.3.11 Coupon 2, Burn 4—Magnified Region

The change in surface appearance between Burn 3 and Burn 4 is also significant. Rather than the rolling surface of Burn 3, the surface of Burn 4 is more jagged and has a significantly higher Ra value (115% percent higher) (Figure 27). The value of $\overline{\alpha_f}$ increased from 7.4° for Burn 3 to 13.6° for Burn 4, confirming the visible increase in peakedness. This value of the average forward facing angle is very close to that of Burn 2, being only 2.2% lower. This much higher roughness may be due in part to some post-burn deposit flaking, or possibly to some erosion that occurred during Burn 4, in the upper left-hand portion of the region (Figure 26).

3.3.12 Coupon 2 Magnified Region Roughness Trend

If the surface left behind after Burn 1—in which nearly all deposits had flaked off—were to be taken as a starting point for deposition evolution, then an interesting trend is revealed (Figure 27). Roughness—in the form of Ra and Rq—initially increases substantially (Burn 1 to Burn 2). This is followed by a phase in which the rate of increase slows (Burn 2 to Burn 3). Finally, the rate of roughness increase picks up again (Burn 3 to Burn 4). Although it had been expected that the values of Ra and Rq would increase with exposure to deposition conditions, this precise trend was unexpected.

Even more unexpected than the exact trend in the increase in roughness was the fluctuation seen in the peakedness of the deposit structures, as shown by both a visual examination of the three-dimensional surface representations as well as by a comparison of the average forward facing angle, $\overline{\alpha_f}$ (Figure 27). After Burn 1 and the subsequent flaking of the local deposits, the zoomed surface of Coupon 2 showed a relatively low value of $\overline{\alpha_f}$. This value increased by 1120% after Burn 2, resulting in the high peak-dominated surface seen in Figure 26c. With Burn 3, a 'wavier' surface was produced with the attendant 46.8% drop in average forward facing angle. Finally, the surface of Burn 4 returned to a more peaked state, as was indicated by its 83.8% increase in $\overline{\alpha_f}$ over that of Burn 3. Also of note is the fact that Rz follows the same trend as that of $\overline{\alpha_f}$, with the value of Rz following the first effective burn (Burn 2) exceeding that of the following burn. This is then followed by a rapid upturn that coincides with the upturn in the average forward facing angle. This trend in the increase in roughness as well as a similar fluctuation in $\overline{\alpha_f}$ can also be seen in the evolution of deposits on the TBC coupon, Coupon 3 (see section 3.4.5).

3.4   Coupon 3: TBC Coated Substrate

Coupon three was exposed to similar deposition conditions as the preceding two coupons (Table 5). The surface topologies and three-dimensional representations presented are derived from a 9.52 mm x 5.71 mm portion of the measured surface that was used as the basis for the wind tunnel models intended for convective heat transfer experiments (Figure 28).
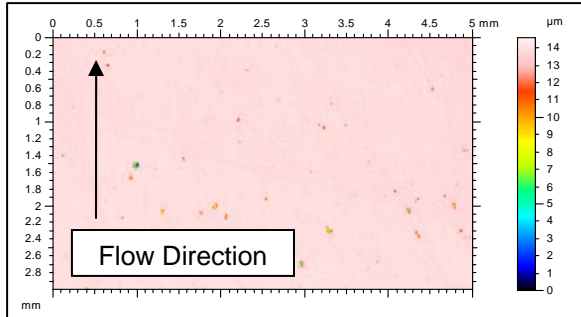
Figure 25a. Topological map of zoomed Coupon 2 preburn.
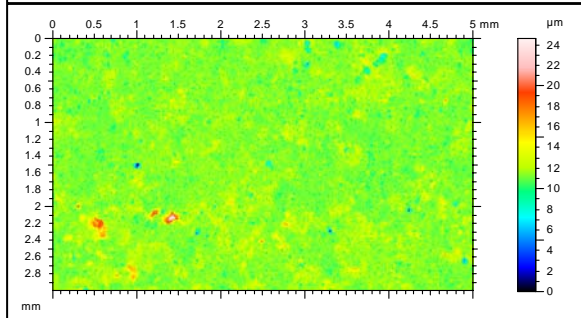
Figure 25b. Topological map of zoomed Coupon 2 Burn 1.
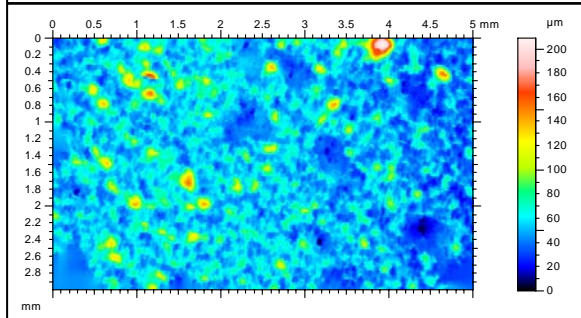
Figure 25c. Topological map of zoomed Coupon 2 Burn 2.

Figure 25d. Topological map of zoomed Coupon 2 Burn 3.

Figure 25e. Topological map of zoomed Coupon 2 Burn 4.

**Figure 25.** Topological representations of deposits on Coupon 2, zoomed region (Bare Substrate).

48
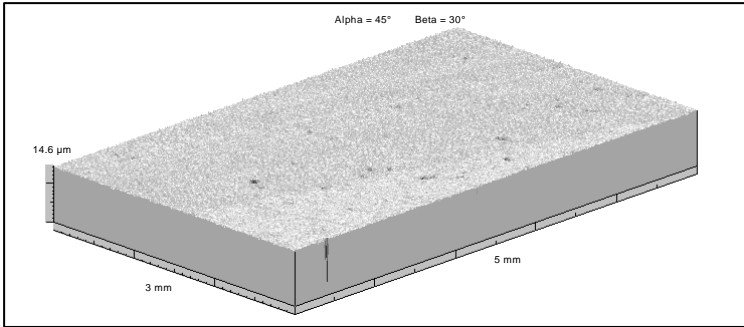
Figure 26a. Three-dimensional representation of zoomed Coupon 2 preburn.
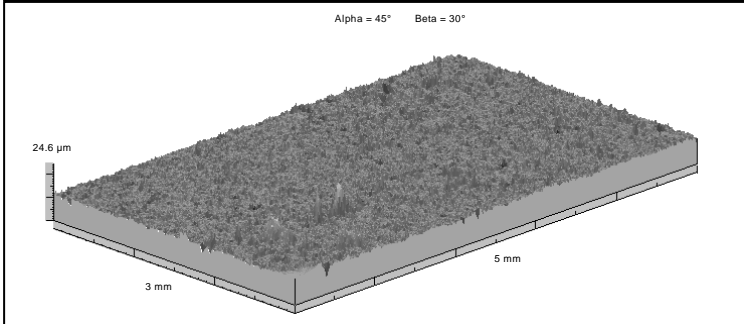
Figure 26b. Three-dimensional representation of zoomed Coupon 2 Burn 1.
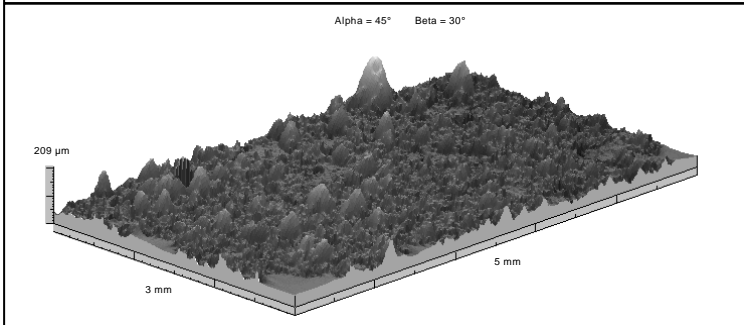
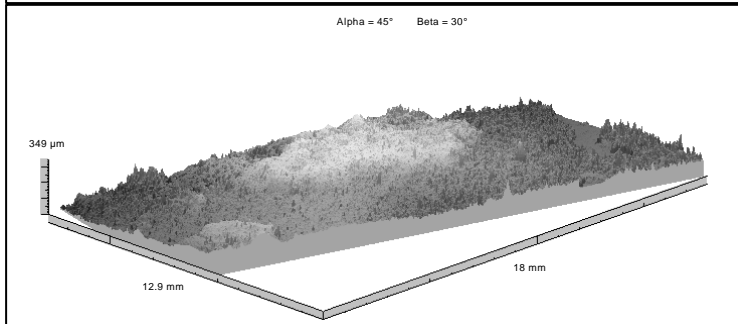**Figure 26c.:** Three-dimensional representation of zoomed Coupon 2 Burn 2.
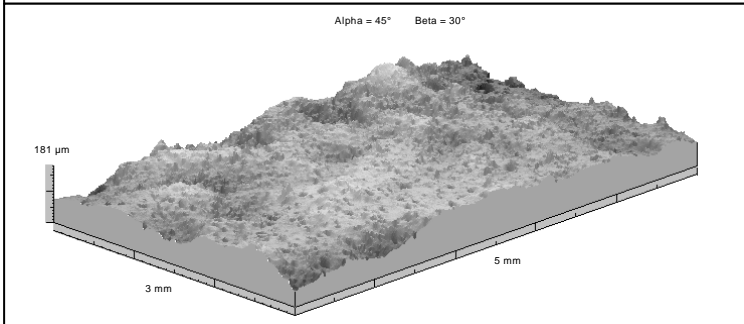
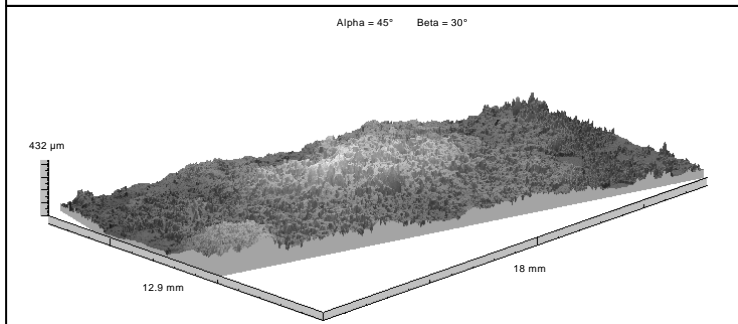**Figure 26d.** Three-dimensional representation of zoomed Coupon 2 Burn 3.

Figure 26e. Three-dimensional representation of zoomed Coupon 2 Burn 4.

**Figure 26.** Three-dimensional representations of deposits on Coupon 2, zoomed region (Bare Substrate).

49
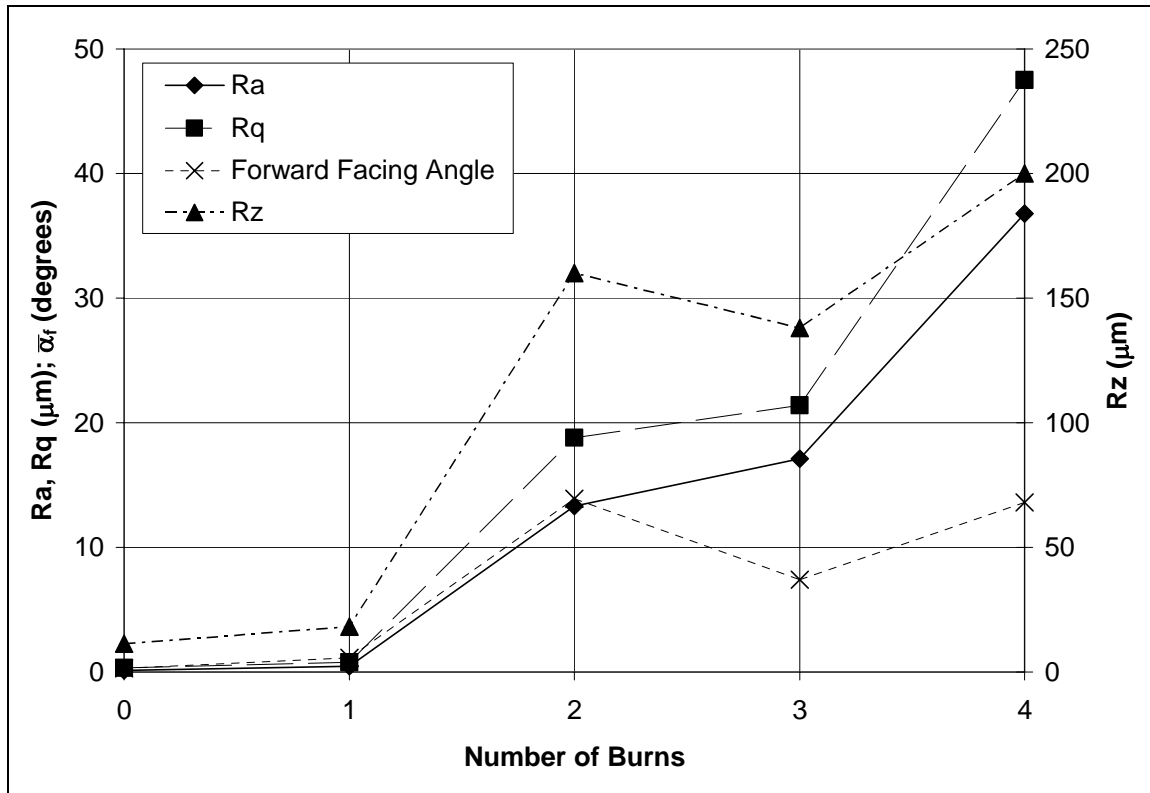
Figure 27. Plot of roughness statistics for the zoomed 5 mm x 3 mm region of Coupon 2.

The near uniformity of the deposits on Coupon 3 allows the magnified region to be representative of the whole with regards to *Ra* and *Rq*. However, due to the sensitivity of *Rz* to relatively small areas of tall peaks or low valleys, the difference between the average peak-to-valley values of the magnified region versus those of the overall surface measurement is much more substantial (see Table 6).

This region was selected, in part, because of damage suffered by the TBC following Burns 3 and 4. Thermal cycling caused portions of the TBC on the coupons left side to crack and lift away from the rest of the surface, a process known as spallation. Further damage occurred when the raised portions of the TBC were removed to avoid damage to

50

the Hommel profilometer stylus. Thus, the location of the magnified region was chosen

so as to avoid the spalled portions. The spalled region is ignored in all roughness statistics

in this section.

Unlike Coupon 2, the deposits formed on Coupon 3 were relatively uniform with little

noticeable deposit flaking. This may be due to several factors: first, the preburn surface of

the TBC coupon was rougher than the polished surface of Coupon 2. Second, unlike the

non-porous polished metal substrate of Coupon 2, the surface of Coupon 3 was coated

with a 1.3 mm thick layer of a relatively porous ceramic material. The porosity of the

TBC would likely allow deposits to become better anchored during formation. Finally,

the lower coefficient of thermal expansion inherent in a ceramic coating such as the TBC

would produce less strain on any attached deposits during cool-down.

Table 5. TADF experimental settings for Coupon 3 (TBC).

| Burn | Temperature (C) | Simulated Parameters | | ppmw-hrs | Test Parameters | |
		Time (hrs)	ppmw		Time (hrs)	ppmw
1	1157	1827	0.02	36.54	2	18.27
2	1155	2680	0.02	53.6	2	26.8
3	1155	2314	0.02	46.28	2	23.14
4	1155	2314	0.02	46.28	2	23.14

A comparison between the results obtained for the TBC coated coupon (Coupon 3) and

the real turbine blade samples evaluated during Jensen's research reveals that several

major roughness statistics are of the same order of magnitude (Table 7). Although a

direct comparison cannot be made between blades that have not been exposed to identical

deposition conditions, the fact that these statistics are similar suggests that the deposits

that have formed on Coupon 3 are similar in character to deposits that formed on real

turbine blade surfaces.

Table 6. Comparison between overall surface roughness statistics and the magnified region roughness statistics.

	Burn	1	2	3	4
Ra	Overall Surface	16.3	18.1	22.9	30.9
	Zoomed Region	16.6	17.1	20.2	32.9
	% Difference	1.84	-5.52	-11.79	6.47
Rq	Burn	1	2	3	4
	Overall Surface	20.6	23.5	30.2	38.9
	Zoomed Region	20.8	22	25.9	40.1
	% Difference	0.97	-6.38	-14.24	3.08
Rz	Burn	1	2	3	4
	Overall Surface	204	222	250	366
	Zoomed Region	174	140	145	286
	% Difference	-14.71	-36.94	-42.00	-21.86

Table 7. Comparison between service blade roughness statistics and the TBC coupon (Coupon 3) statistics.

	Surface Type	Ra (μm)	Rt (μm)	α_{rms}	Λ_s
Serviced Blades	25000hr blade Figure 3	32	240	27	22
	22500hr blade	41	296	24	36
	<1000hr blade	19	394	18	77
	24000hr vane	17	220	15.8	134
TBC Coupon	Burn 1	16.6	194	17.2	49
	Burn 2	17.1	172	15.8	72.5
	Burn 3	20.2	186	15.8	73
	Burn 4	32.9	286	19	108

3.4.1   Coupon 3, Burn 1

The surface produced by Burn 1 consists mostly of small, evenly distributed roughness

structures along with some sharp peaks and a few larger clumps of deposits (Figure 29b

and Figure 30b). *Ra* has increased from the 2.14 μm of the preburn surface to 16.6 μm.
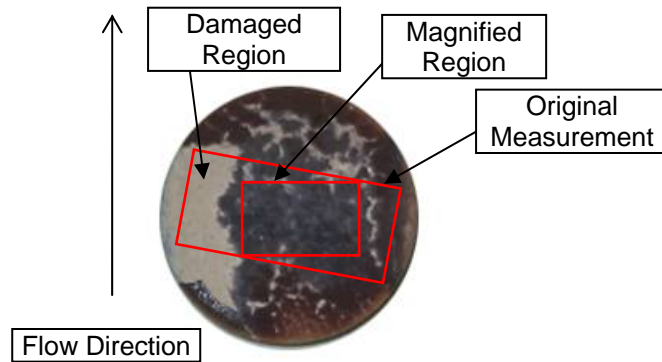
Figure 28. Illustration of location of surface measurement and magnified region. Image above is of Coupon 3 Burn 3.

The fact that much of the roughness consists of sharp peaks rather than the thick crusts of deposits found on later burns makes the surface of Coupon 3 Burn 1 somewhat similar to Coupon 2 Burn 2—the effectual first burn of Coupon 2. By comparison, the value of $\overline{\alpha_f}$ for Coupon 3, Burn 2 is 12.6°, which is 9.3% lower than that of Coupon 2, Burn 1.

3.4.2   Coupon 3, Burn 2

The large peak seen after Burn 1 located at x=8 mm and y=2 mm is missing from Burn 2 (Figure 30c). A region of deposits in the lower right-hand corner at approximately x=7 mm and y=5.5 mm has begun to grow. A very tall peak has also grown in the upper right-hand corner. With regards to roughness, statistically there has been very little change: the value of *Ra* increased by 3%. The average forward facing angle has dropped to 10.7°, indicative of a slight decrease in the peakedness of the surface roughness.

3.4.3 Coupon 3, Burn 3

With Burn 3, the region of deposits in the lower right hand corner has persisted and has become more prominent (Figure 30d). The peak in the upper right hand corner is now gone. Except for these few changes, the appearance of the two surfaces is similar, as are their respective roughness statistics. *Ra* has increased by 18.1% to a value of 20.2 μm. The value of $\overline{\alpha_f}$ is nearly identical at 10.9°.

3.4.4 Coupon 3, Burn 4

With Burn 4, the deposits in the lower right hand corner have grown dramatically and cover a sizeable portion of that corner (Figure 30e). A very large clumping of deposits has formed in the upper left hand corner with no noticeable precursor in the previous burns. This suggests that, while some roughness structures have a long evolutionary history that is relatively easy to trace over time, other structures appear quite suddenly. The roughness has increased significantly: *Ra* has increased by 62.87% to a value of 32.9 μm. The average forward facing angle has increased to 12.95°, showing that the surface is now more peak-dominated than following the previous burn. As was the case for Coupon 2, Burn 4, this value of $\overline{\alpha_f}$ is similar to that of the first effective burn (Burn 2 for Coupon 2, Burn 1 for Coupon 3). In the case of Coupon 3, the average forward facing angle for Burn 4 is 2.61% higher than that of Burn 1.
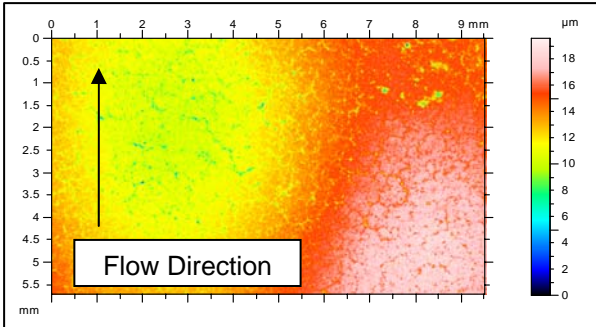
Figure 29a. Topological map of Coupon 3 preburn.
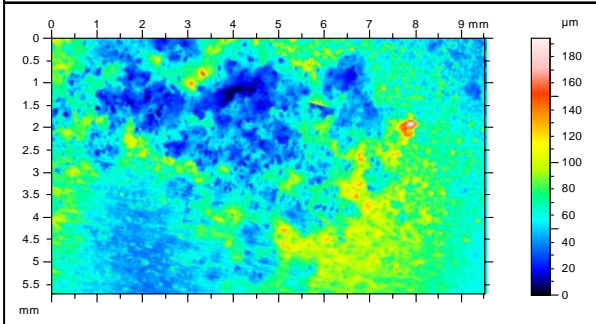
Figure 29b. Topological map of Coupon 3 Burn 1.
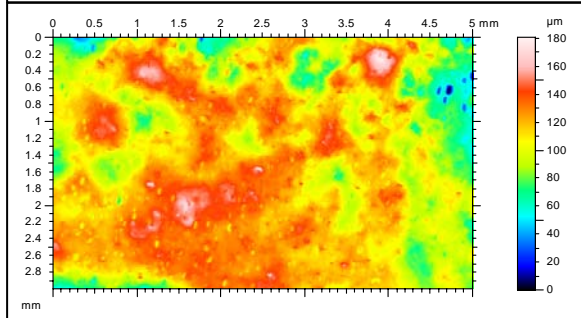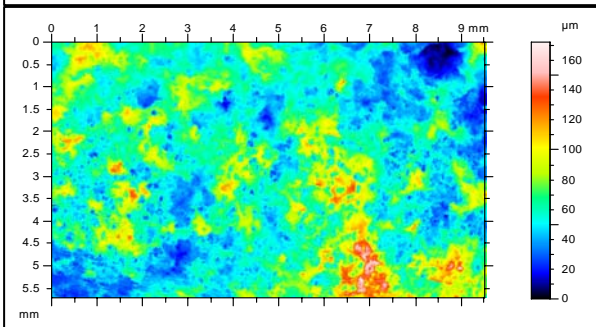
Figure 29c. Topological map of Coupon 3 Burn 2.
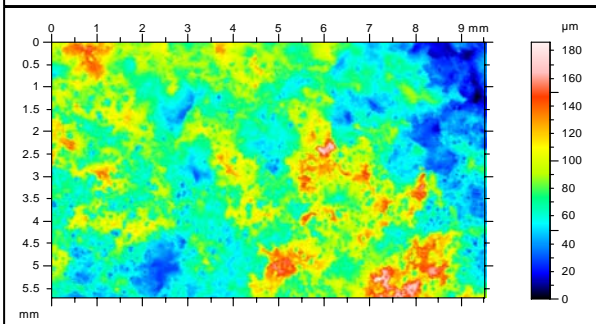
Figure 29d. Topological map of Coupon 3 Burn 3.
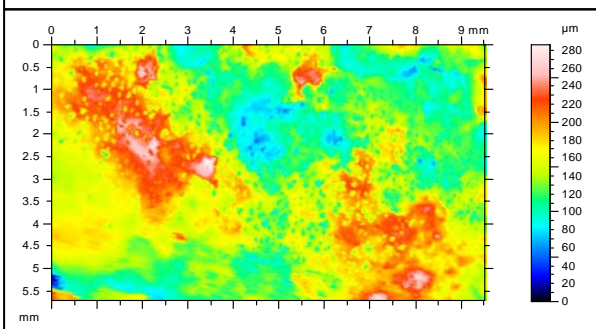
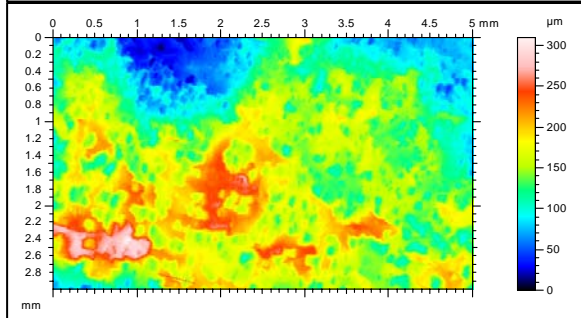**Figure 29e.** Topological map of Coupon 3 Burn 4.

Figure 29. Topological representations of deposits on Coupon 3 (TBC).

55
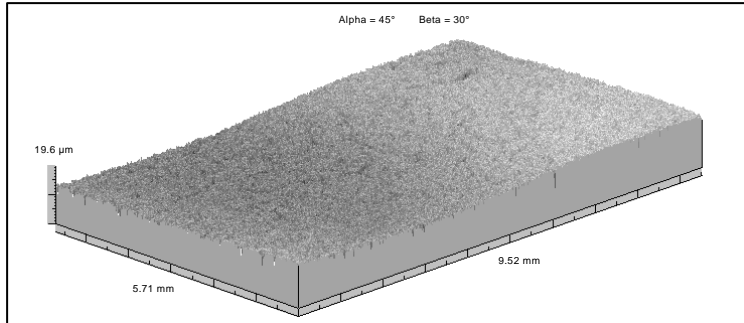
Figure 30a. Three-dimensional representation of Coupon 3 prior to exposure to deposition conditions (preburn).
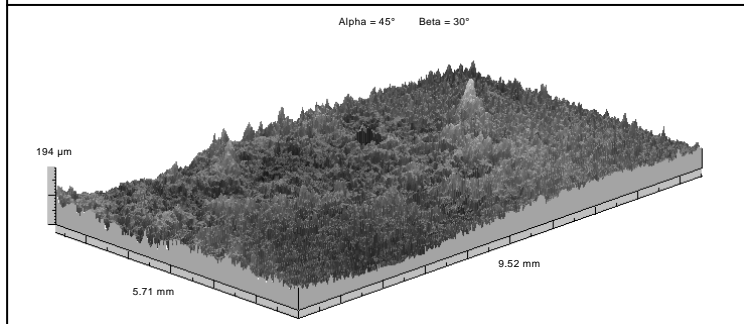
Figure 30b. Three-dimensional representation of Coupon 3 Burn 1.
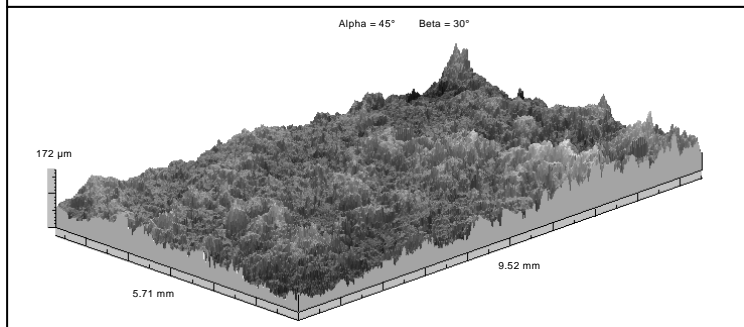
Figure 30c. Three-dimensional representation of Coupon 3 Burn 2.

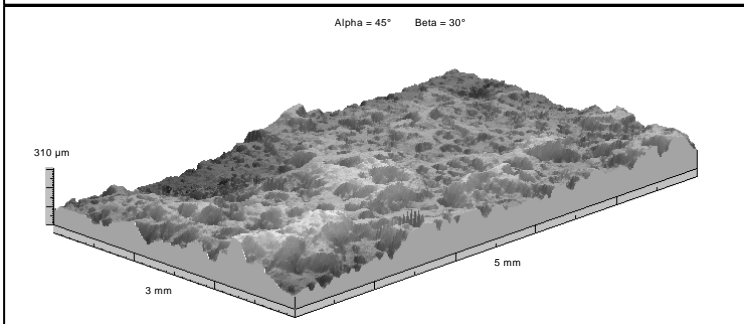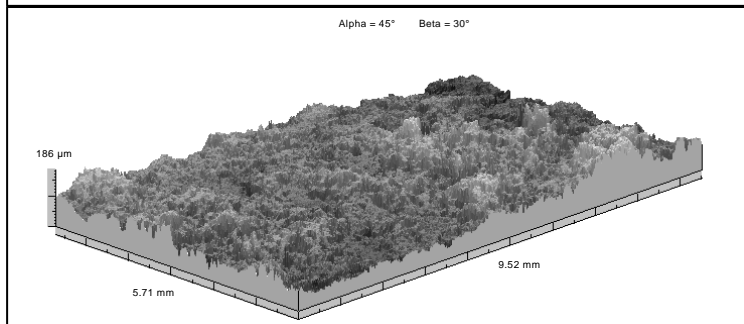**Figure 30d.** Three-dimensional representation of Coupon 3 Burn 3.
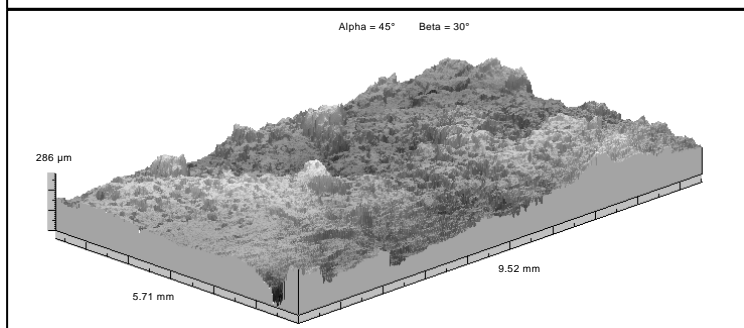
Figure 30e. Three-dimensional representation of Coupon 3 Burn 4.

Figure 30. Three-dimensional representations of deposits on Coupon 3 (TBC).
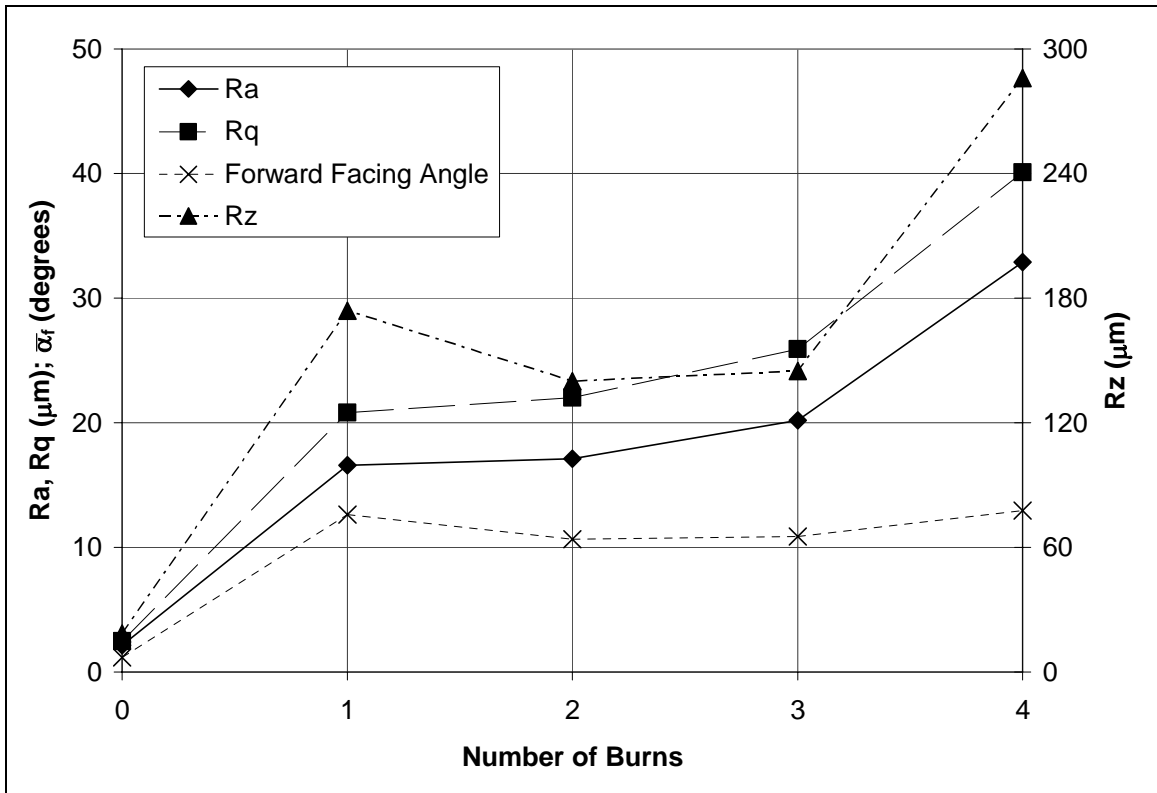
Figure 31. Plot of roughness statistics for a 9.52 mm x 5.71 mm region of Coupon 3.

3.5   Commentary on Roughness Similarities Between Coupons 1, 2, and 3

A review of the different types of surfaces experienced by Coupons 2 and 3 illustrates

that the deposits on a turbine blade surface may undergo extreme changes in character

and appearance over time, despite having been exposed to the same deposition conditions

(e.g., duration of exposure, particulate loading, and freestream temperature). At one point

the deposits may take the form of distinct peaks. At another point, the deposits may form

a thick, wavy crust. Some structures may slowly develop over time, whereas others

appear much more rapidly. The only apparent constant is that surface roughness, in the

form of *Ra* and *Rq*, continually increases with time, although not necessarily at a constant

rate.

The interruption in the rise of Ra, Rq, and $\overline{\alpha_f}$, in which there is a "pause" in Ra and Rq and a decrease in $\overline{\alpha_f}$, is of particular interest. Whether or not this pattern continues could be determined with further burns beyond what has been performed for this study.

Why this trend occurred is not entirely known. It is possible that, with the initial exposure to deposition conditions, large peaks are formed across the relatively smooth surface, resulting in a spike in Rz and average forward facing angle, $\overline{\alpha_f}$. As time passes, the continuing deposition fills in the valleys between the peaks, resulting in a decrease in those two values. At this point, the surface roughness begins to plateau. This might continue until a certain "critical mass" is reached, at which point a new series of peaks is formed, resulting in an increase in Ra, Rz, and $\overline{\alpha_f}$ similar to that seen after the initial exposure to deposition conditions.

Analysis of Coupon 1 shows that it follows a similar pattern as Coupons 2 and 3, although with a different starting point. The preburn Ra of Coupon 1 is 21% higher than the Burn 2 Ra for the magnified region of Coupon 2 and only 5.8% lower than the Burn 1 Ra of Coupon 3. The average forward facing angle for the Coupon 1 preburn surface is also quite high. Red boxes in Figure 32 illustrate where the evolution of deposits on the surface of Coupon 1 falls with regards to deposit evolution on the other two coupons. Whereas Coupons 2 and 3 developed peaked surfaces with higher values of $\overline{\alpha_f}$ following the first effective burn, Coupon 1 began with such a surface. Consequently, the exposure of Coupon 1 to deposition conditions caused a decrease in the average forward

facing angle, just as it occurred with Coupons 2 and 3. Additionally, the values of *Ra* and

Rq saw a period of stagnation in all three cases. It is likely that further deposition would

have also caused Coupon 1 to experience an increase in the roughness statistics

mentioned.
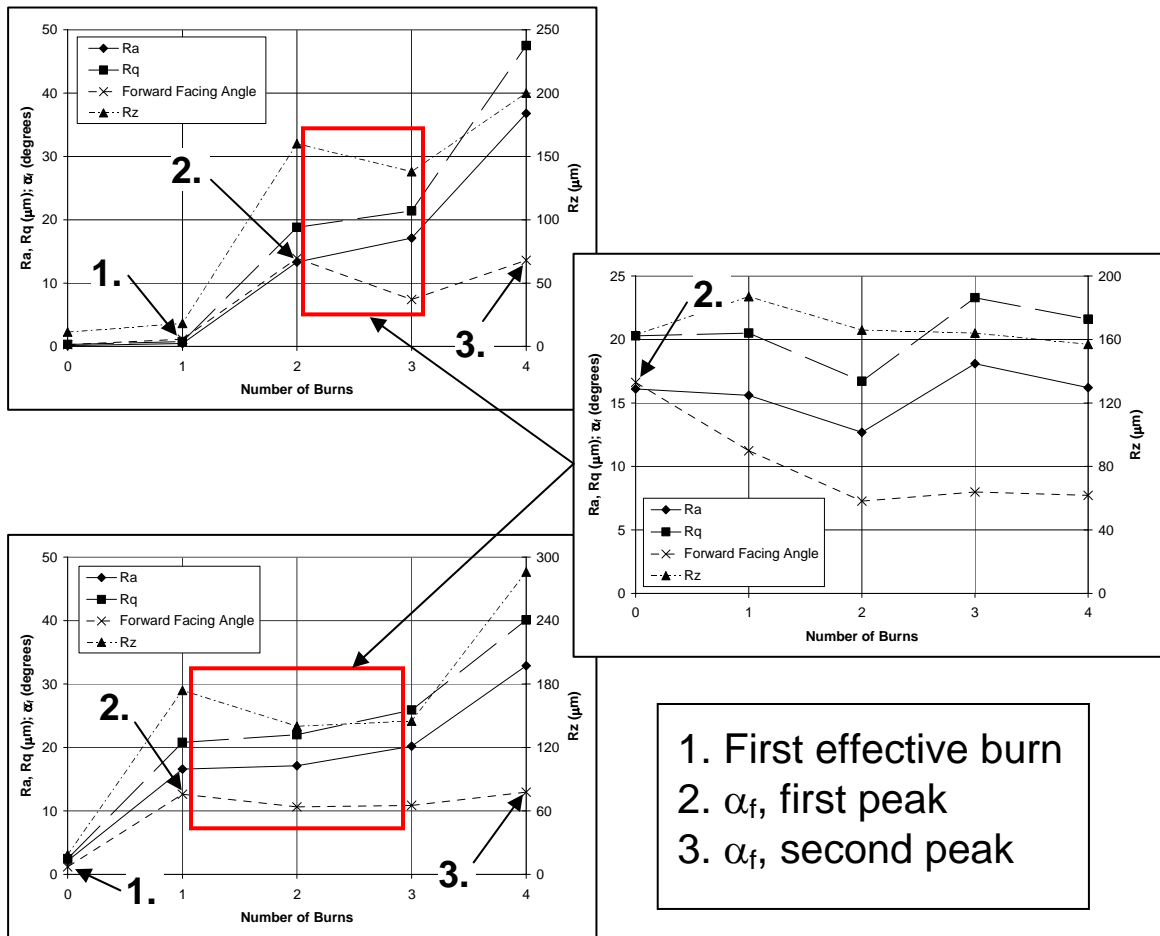
Figure 32. Comparison between deposit evolution on Coupons 1, 2, and 3.

Chapter 4: Convective Heat Transfer Measurements—Experimental Facilities and Techniques

4.1 Roughened Turbine Blade Surfaces and Convective Heat Transfer

With the development of accelerated deposition evolution, the convective heat transfer characteristics of the surfaces produced could be determined. The method chosen to accomplish this is relatively common and involves the use of a heated wind tunnel and scaled-up Plexiglas models of the rough coupon surfaces. In order to allow the use of a fairly conventional wind tunnel with manageable freestream velocities and temperatures, the heat transfer characteristics of the surfaces tested were expressed in the form of the dimensionless Stanton number (St):

$$St = \frac{h}{\rho u_\infty c_p} \tag{7}$$

4.2 Roughness Models

Plexiglas models of the rough surfaces of the coupons were used for the wind-tunnel based thermal studies for several reasons. First, the method used to find the Stanton number requires that the thermal diffusivity of the rough surface be known. The non-isotropic nature of the coupon surfaces with deposits makes determination of an average density and specific heat difficult, while the complex structure of the deposits requires extensive testing to determine their thermal conductivity. A scaled-up isotropic model of

61

the coupon surfaces that is constructed of a material of known thermal properties is therefore preferable in this regard. The material used was Atofina (now Arkema Group) Plexiglas G cast acrylic (Table 8). Second, in order to simulate the conditions found within a gas turbine, the turbine blade Reynolds number must be matched. Because the freestream velocity produced by the wind tunnel is much lower than that experienced by a first stage turbine blade, a model that is larger than the original surface must be used to allow Reynolds number matching.

Table 8. Average thermal properties for Arkema Plexiglas G at 25°C.

ρ (kg/m^3)	k (W/mK)	c_P (J/kgK)
1190	0.19	1464

Four Plexiglas roughness models were produced based on the results from the TBC coupon. The TBC coupon was selected for having the same kind of coating that is most often used on the first stage blades of modern gas turbines. The roughness models produced were based on the measurements of the coupon surfaces made with the aforementioned Hommel profilometer. The text files created during topological measurements were fed into a MATLAB program written by the author in order to convert the raw data into a form compatible with a CNC mill. This program scaled the model up, converted units from millimeters to inches, and added axis callouts, cutting speeds, and other information necessary for CNC-compatible code. Model scaling was limited by the ratio Rz/θ, which did not exceed a value of 3 (Table 9). The momentum thickness, θ, was measured during wind tunnel validation.

Table 9. *Rz/θ* ratios for TBC coupon models.

Burn	1	2	3	4
Model *Rz* (mm)	3.48	2.8	2.9	5.72
Rz/θ	1.36	1.10	1.14	2.24

A review of the literature shows that, as a general guideline in turbine roughness

experimentation, the ratio of *Rz/θ* does not exceed a value of 3 (e.g. Bons, 2002). The

four surfaces in this study were enlarged by a factor of 20, which produced a maximum

Rz/θ ratio of 2.24 in the case of Burn 4. Because of this scaling factor, and due to the

limited size of the largest usable rectangular region of roughness with the appropriate

proportions (5.715 mm x 9.525 mm), the original data formed 25% of the total model

surface, with the remaining 75% being composed of mirror images of the original data.

Thus the entire 22.86 cm x 38.1 cm space provided for the model in the wind tunnel was

filled (Figure 33).
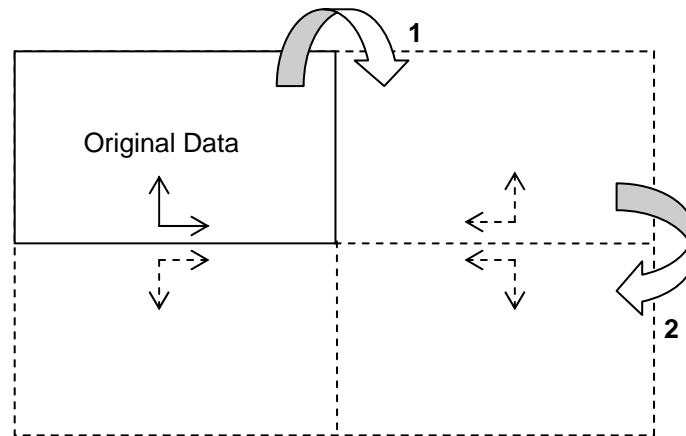
Figure 33. Technique used to mirror data. 1. Original data is mirrored across the y-axis in order to form the top half of the model. 2. The top half is then mirrored across the x-axis in order to form the bottom half of the model.

Although by mirroring the data a region has been produced in which the average forward facing angle is now the leeward facing angle and vice versa, this only occurs on the upstream half of the models. The average surface temperature of only the downstream half, where the forward facing angles of the original surface are correctly oriented, is measured by the FLIR camera. Each model measures 22.86 cm x 38.1 cm, with the leading 11.43 cm of the model serving to accomplish the smooth-to-rough transition. Antonia & Luxton (1971) and Taylor & Chakroun (1992) showed that the smooth-to-rough transition occurs within approximately 3 to 4 boundary layer thicknesses. Within the region of transition, skin friction values (c_f) and Stanton numbers can be up to 20% higher than the transitioned values. For the wind tunnel used in this project, pitot probe measurements showed that the average boundary layer thickness in the vicinity of the models was 2.3 cm, giving a smooth-to-rough transition length somewhere between 6.9 cm and 9.2 cm. In order to ease the transition from flow over smooth panels to flow over a rough panel, approximately 1 cm of the leading edge of each model was machined with a 5/8" ball end mill down to the meanline of the model roughness (Figure 34).

Given that each raw data file was composed of nearly 550,000 discrete points, and that this number of points would have to be quadrupled in order to fill the necessary area, the program which produced the CNC code also deleted every other x-coordinate and every other y-coordinate prior to mirroring the data. This increased the x and y distance between each point from approximately 0.203 mm to 0.406 mm. Despite this fourfold decrease in the number of points used to reproduce the coupon surfaces, the resulting
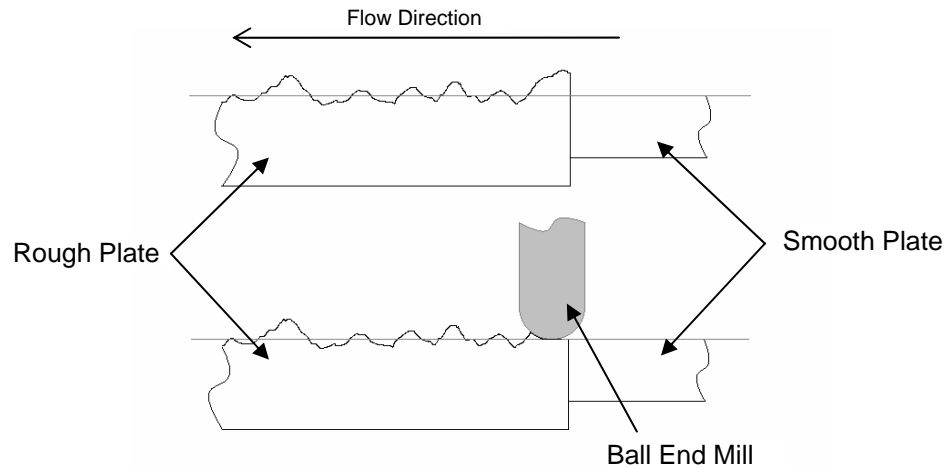
Figure 34. A ball end mill is used to eliminate an abrupt smooth-to-rough transition at the model's leading edge.

CNC code was 12.7 MB in size and required 10 hours to machine. The impact of this decrease in resolution on the values of *Ra* and *Rq* was not measured.

With the CNC code, the roughness models were cut out of 2.54 cm thick Plexiglas acrylic sheets using a Fryer CNC mill equipped with a modified countersink. The countersink was chosen because it most closely approximated the tip of the profilometer stylus that scanned the surface originally. Both are conical in shape with a 90° included angle. This was to ensure that the model contours would be as close as possible to the original surface measurements. However, the countersink is not precisely a 20x scaled-up model of the Hommel stylus. The stylus had a tip radius of 5 μm, which would translate to a scaled-up tip radius of 0.1 mm, whereas the countersink had a tip radius of approximately 0.5 mm. This causes a slight error in the cutting of the model. The worst case scenario, in which the most amount of actual surface material is removed, is one in which the countersink cuts along the side of a structure with a 45° slope. In this event there would

65

be an error of 0.117 mm perpendicular to the surface (the equivalent of 5.85 µm for the model) (Figure 35). This scenario is not likely to happen more than a few times per model given that the highest average surface angle in either the x or y direction is 13.63° (the average leeward facing angle for Coupon 3, Burn 4). For this angle, the error perpendicular to the surface is 0.011 mm (the coupon equivalent of 0.563 µm) (Figure 36).
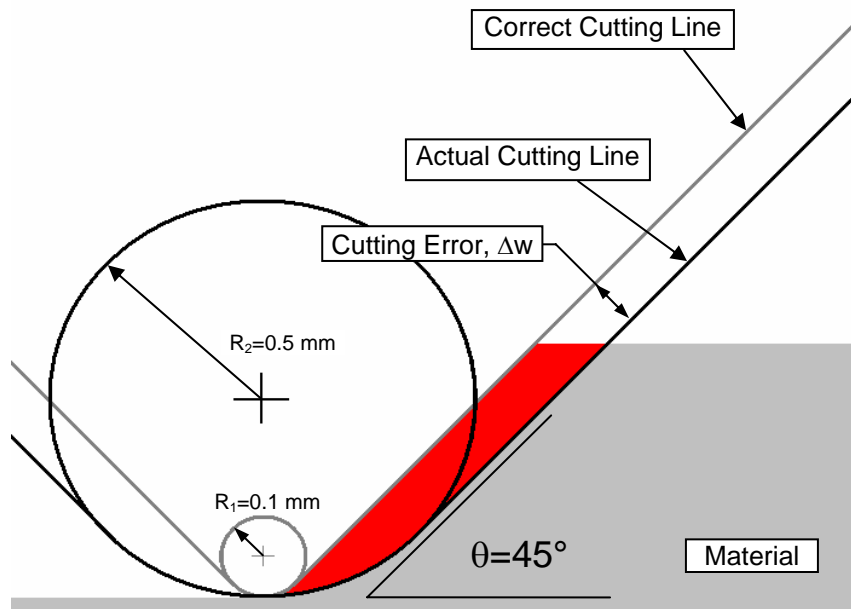
Figure 35. Cutting error worst case scenario. The red region represents material that has been incorrectly removed. Tool path may be into or parallel to the page.

The thickness of the extra material removed perpendicular to the surface, Δw, can be calculated using Equation 8.

$$\Delta w = \left(R_2 - R_1\right)\left(1 - \cos\theta\right) \qquad (8)$$
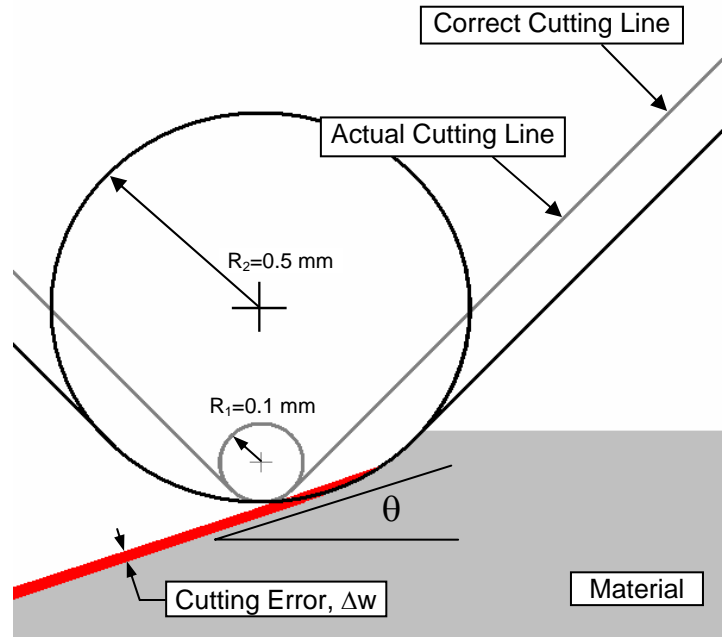
Figure 36. Cutting error for angles below 45°. The red region represents material that has been incorrectly removed. Tool path may be into or parallel to the page.

Additionally, there is an advantage to using a tool with a slightly oversized tip radius.

Due to the fact that the tool-tip is rounded, small ridges are left between the rows that the

tool traces. The size of these ridges can be reduced either by reducing the distance

between the rows (Δy), by increasing the tool-tip radius, or both. Given the size of the file

and the time it takes to machine a model, the option of decreasing Δy was not considered.

Had a tool with a 20x scaled-up tip been used with the 0.406 mm spacing, it would have

produced ridges that were approximately 0.162 mm in height—an equivalent height of

8.09 μm on the coupon. The tool that was used, with the 0.5 mm tip-radius, produced

ridges that were approximately 0.043 mm in height—the scaled-down equivalent of

2.12 μm high ridges (Figure 37). Being on the order of the *Ra* value for the preburn

surface, this ridge height is more acceptable. The deviations from the original surfaces

introduced during the manufacturing process will tend to make the models slightly

rougher. The equipment used during this project did not have the range necessary to measure the magnitude of the effect on *Ra* and *Rq*.
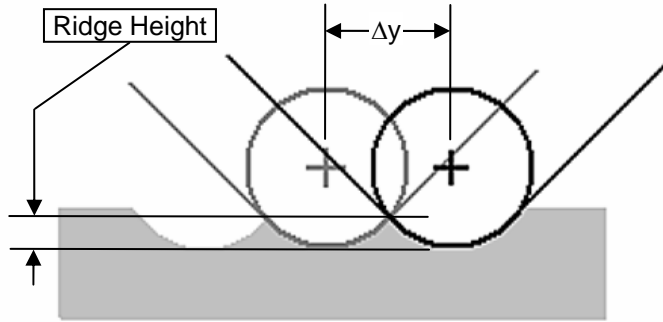
Figure 37. Schematic of ridges formed by rounded tool-tip. Tool path is into the page.

4.3   Wind Tunnel Heat Transfer Analysis

In order to determine the convective heat transfer properties of the deposit roughened surfaces, a technique which takes advantage of a relation developed by Schultz and Jones was utilized (Equation 9) (Schultz & Jones, 1973). The equation derives from the solution of the heat diffusion equation as applied to a semi-infinite surface with one-dimensional conduction. Small departures from a uniform heat transfer rate are assumed and the surface temperature is assumed to be a piece-wise linear function. A derivation of Equation 9 can be found in Appendix B.

$$q"_{cond,i} = \frac{2\kappa}{\sqrt{\pi\alpha}} \sum_{j=1}^{i} \frac{T_{S,j} - T_{S,j-1}}{\sqrt{t_i - t_j} + \sqrt{t_i - t_{j-1}}} \tag{9}$$

This equation was developed to allow the determination of the heat flux into or out of a surface under transient conditions through average surface temperature measurements.

This is the same technique and equation utilized by Bons (Bons, 2002). In this technique, following a period of thermal soaking, a heated freestream is suddenly blown over a roughness model with known thermal properties. The surface temperature history is monitored with a FLIR thermal camera, while the freestream temperature history is monitored by a 0.005" K-type thermocouple immersed in the flow. The small bead size of the thermocouple decreases its response time to much less than 1 second and decreases the radiation error (Appendix C). Freestream temperatures typically fell between 44°C and 51°C.

Due to the assumption that the surface temperature can be modeled as a piecewise linear function, the equation initially produces an unstable prediction of the heat transfer coefficient. Violation of the piecewise linear assumption is due to the temperature fluctuations that occur immediately after heating of the freestream has begun. However, after this period of instability, the heat transfer coefficient achieves a near constant value with time.

4.4 Wind Tunnel Description

A wind tunnel capable of producing a heated freestream is available in building B-38 at Brigham Young University (Figure 38). The wind tunnel produces a stream of air through the use of a blower. The stream passes through a duct and through a section equipped

with heating elements. The stream then passes through a conditioning plenum that smoothly transitions the stream from a circular cross-section to a square one with side lengths of 38.1 cm while also reducing the freestream turbulence through the use of several layers of screen. The square section of tunnel runs for 134.8 cm until it connects to a rectangular test section constructed for this study (Figure 39). The leading edge of the floor of the test section is set 2.7 cm higher than the floor of the square section. Through this gap the boundary layer that had developed up to this point is allowed to bleed off for improved control over boundary layer growth. The first 7.62 cm of the test section floor is constructed of a thin plate of aluminum which forms the leading edge. A length of 2 mm diameter wire is stretched across this plate at a location 2.5 cm from the leading edge to serve as a boundary layer trip.
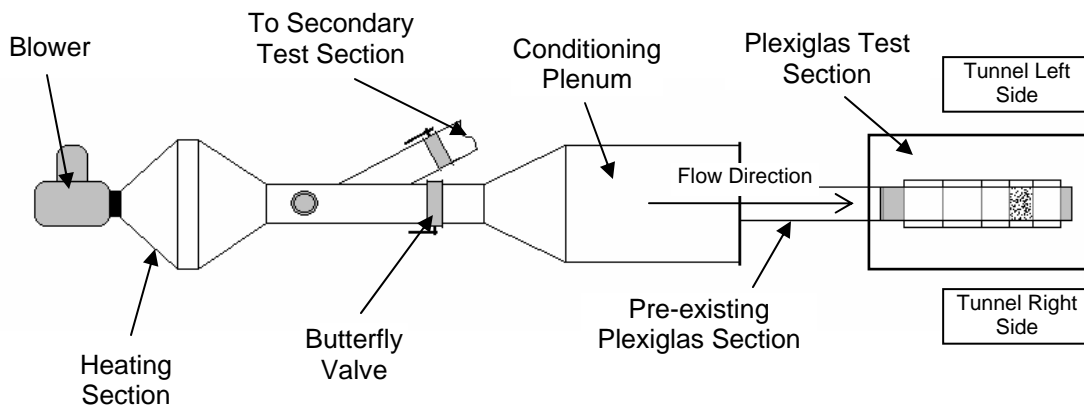
Figure 38. Schematic of the wind tunnel used for heat transfer measurements for this study.

The test section consists of fixed vertical walls, a segmented floor section, and a moveable ceiling. The floor is segmented to allow a roughness model to be placed at a variety of distances from the boundary layer bleed. This allows for greater control over

the ratio of the average roughness height Rz to the local momentum thickness θ of the boundary layer. The roughness model is 38.1 cm wide and 22.9 cm long with its leading edge typically located 103.8 cm from the boundary layer bleed. The ceiling can be adjusted to allow variation of the streamwise pressure gradient present within the test section. Favorable and unfavorable pressure gradients of varying magnitudes may be produced in addition to a pressure gradient of zero. This feature further enhances the controllability of the momentum thickness of the flow over the roughness model.
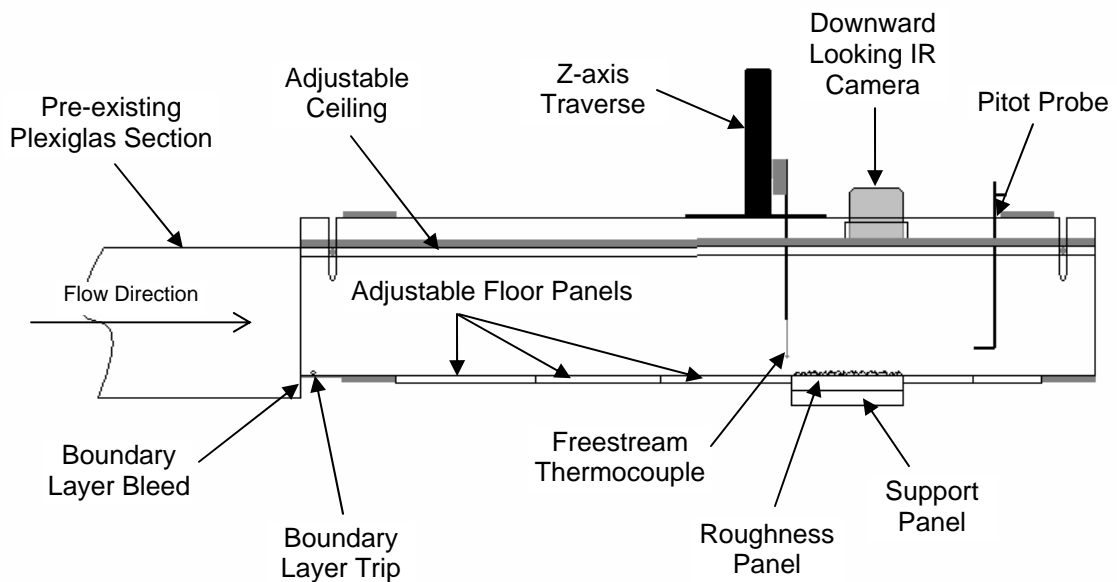
Figure 39. Schematic of wind tunnel test section.

For this study, the wind tunnel ceiling was adjusted so that the pressure gradient would be nearly zero. To achieve this, the ceiling was angled upward approximately 0.3°. The shape of the boundary layer at multiple points along the length of the test section centerline was measured using a boundary layer pitot probe connected to the higher pressure port of a 0.5" H_2O Druck pressure transducer. The lower pressure port of the

71

pressure transducer was connected to the static tap of a stationary pitot probe (Figure 39). All measurements were taken along the wind tunnel centerline. The freestream velocity at each point was determined from each boundary layer measurement. The freestream velocity value found at each point was compared to the others to determine that the pressure gradient within the test section was approximately zero (Figure 40). The boundary layers were found to be self-similar along the length of the tunnel. There was a slight deviation in the boundary layer shape from that of a $1/7^{th}$ power law profile (Figure 41), suggesting the existence of an unresolved disturbance occurring upstream of the test section.

In addition to boundary layer measurements along the length of the test section, boundary layer measurements were made at several points across the freestream in the vicinity of the model location. These measurements showed a difference between the boundary layer on the right side of the test section and the boundary layer on the left side (Figure 42). Although the freestream velocities are nearly the same, the values of δ^*, θ, and H are different (Table 10). It is believed that this asymmetry may be in part due to the high freestream velocities that were used in this study, which were higher than the values for which the tunnel was originally validated.

Table 10. Measured momentum and displacement thickness versus the 1/7th power law prediction. Measurement was taken at the wind tunnel centerline at the location of the model.

	δ^* (mm)	θ (mm)	H
1/7 Power Law	2.687	2.089	1.286
Measured at 123cm	3.141	2.263	1.388
% Difference	16.90	8.33	7.91
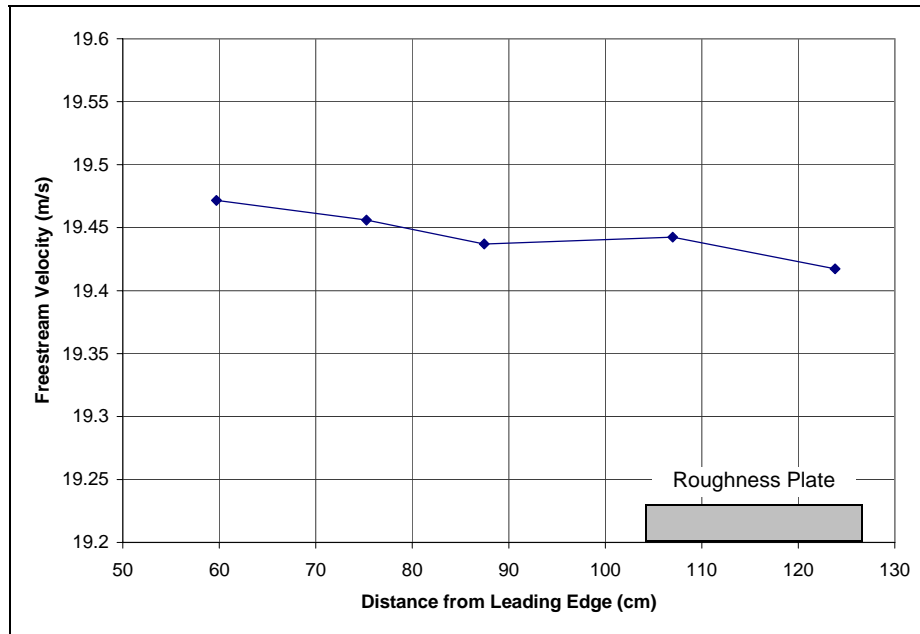
Figure 40. Freestream velocities measured at various distances from the test section leading edge (boundary layer bleed).
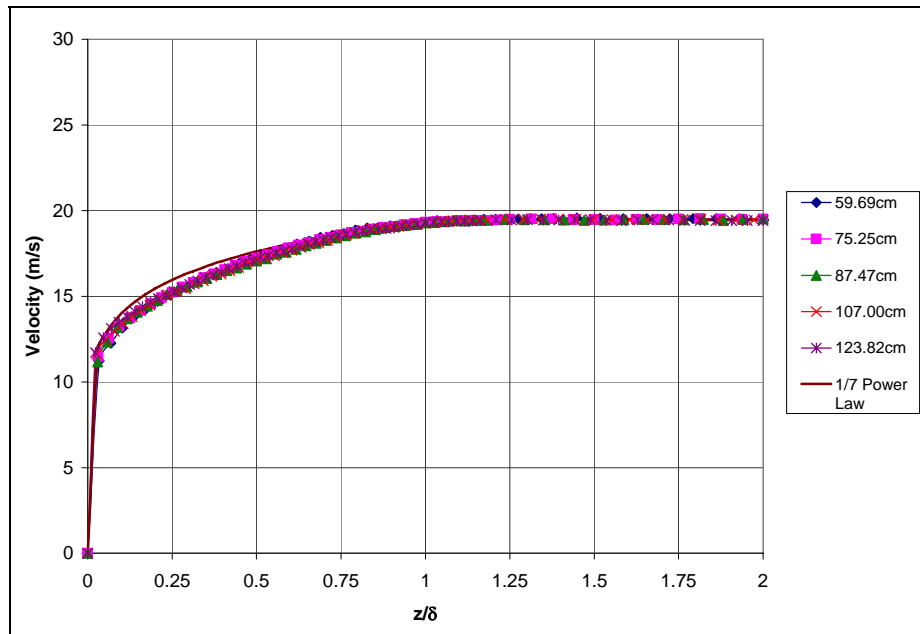
Figure 41. Boundary layer profiles taken at several distances from the leading edge of the wind tunnel test section. All measurements were taken at the wind tunnel centerline.
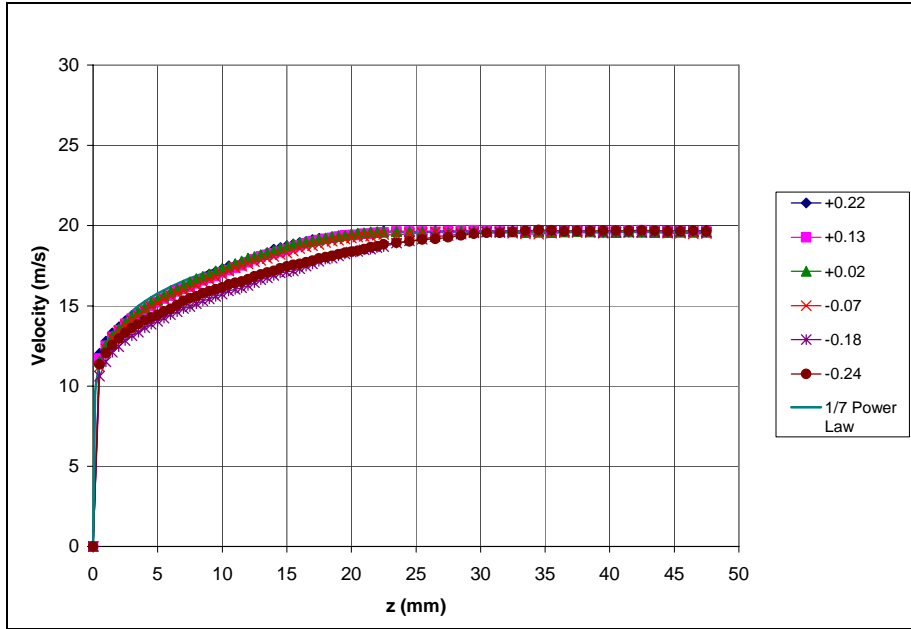
Figure 42. Boundary layer profiles measured across the width of the test section. Distances are measured from the tunnel centerline and are normalized by the tunnel width.

Table 11. Average measured momentum and displacement thicknesses versus those predicted by the 1/7th power law. Measurements were taken across the width of the wind tunnel at the model location.

	δ^*	θ	H
1/7th Power Law	2.874	2.236	1.285
Measured (average)	3.548	2.549	1.392
% Difference	23.45	14.00	8.29

4.5 Thermal Measuring Devices

The FLIR infrared camera is vertically mounted on top of the wind tunnel test section and is aimed directly at the roughness model. The surface temperature data recorded by the camera over time is output to a laptop computer at a user-defined rate. The camera is capable of showing the varying temperatures of a surface through a color coded image and can determine the average temperature of a user-selected region. For this study, the minimum zoom factor of 1.00 was selected, allowing the camera to view a section of the

model 15.87 cm wide and 11.43 cm long with a resolution of 320x240 pixels. The surface

temperature data was recorded by the computer at a sample rate of one reading per

second. The freestream temperature was monitored by a K-type thermocouple with a

bead diameter of 0.127 mm inserted into the flow. This device is also sampled at a rate of

one reading per second. The thermocouple is located at the leading edge of the model and

is fixed approximately 50 mm (~2δ) above the test section floor. The distance of two

boundary layer thicknesses was chosen after it had been discovered that the core flow of

the wind tunnel was approximately 1 to 2 degrees cooler than those regions closer to the

tunnel floor. A measurement of the thermal boundary layer indicated that the freestream

temperature was constant up to at least 2.5 boundary layers. This thermocouple is

monitored simultaneously with a static tap-equipped pitot probe to measure the

freestream velocity during testing.

4.5.1   FLIR Camera In Situ Calibration

An in situ calibration of the FLIR camera was performed which produced a correction

curve for temperature measurements made by the camera. A flat plate that was made of

the same type of Plexiglas as the roughness models and was shown through experiment to

have an emissivity of 0.9 was placed in the wind tunnel. One thermocouple was affixed

to the surface exposed to the flow and another 0.005" diameter bare wire thermocouple

was sandwiched between the underside of the plate and the support panel (see Figure 39).

These two thermocouples indicated when the plate had become isothermal. The plate was

heated to five distinct temperatures within the range of temperatures that a model may

experience during a wind tunnel experiment. These five points were plotted against the

temperature indicated by the surface thermocouple and a curve fit was applied. The temperatures recorded by the FLIR were found to deviate linearly from that of the actual surface (Figure 43).

The equation shown on the plot:

$$T_s = 0.95176T_{IR} + 1.97913$$
$$R^2 = 0.99989$$
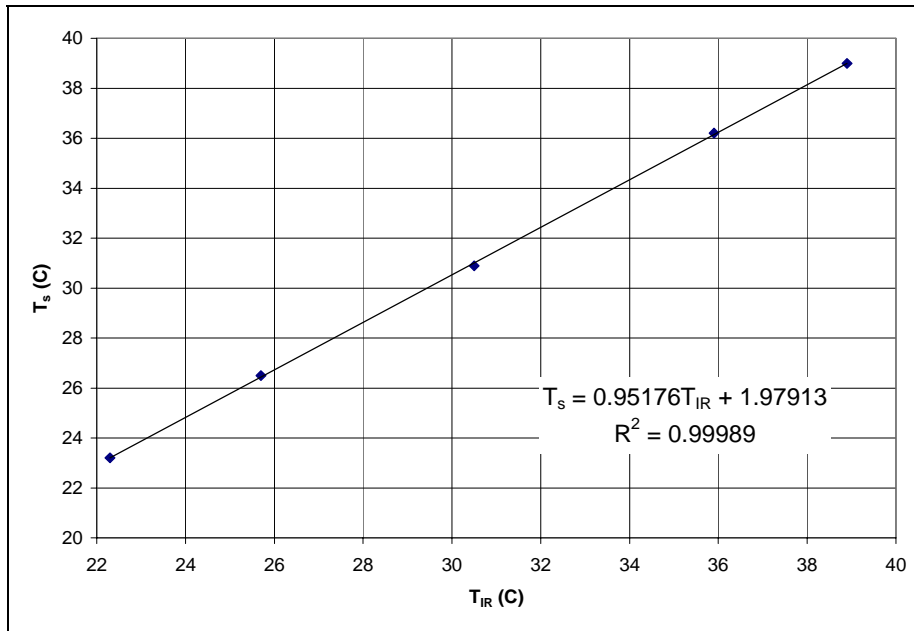
Figure 43. Curve fit for FLIR camera in situ calibration.

4.5.2   FLIR Camera Ambient Temperature Correction

The surface temperature measurements made by the thermal camera were found to be very sensitive to the ambient temperature; i.e. the temperature of the Plexiglas walls surrounding the model. Although the camera software can compensate for the ambient and atmospheric temperatures, these values must be input into the computer manually and cannot be changed while the camera is recording. This does not cause a problem during steady state measurements such as those performed during the in situ calibration.

However, since the ambient temperature is transient during the convective heat transfer experiments, a degree of error is introduced.

The FLIR camera allows a recorded measurement to be played back with different ambient and atmospheric temperature settings. The temperature history resulting from the changes can be saved as a text file. In order to compensate for the error introduced by the limitation of using a fixed ambient temperature, the recording was played back with two different settings: the first set at the initial ambient temperature, immediately prior to the moment at which the heated freestream passed over the surface, and the second at the final ambient temperature achieved during the test. A linear interpolation between the two surface temperature data sets was applied to determine the appropriate surface temperature at any given moment of the temperature history based on the ambient temperature at that moment.

Unfortunately, the ambient temperature was initially assumed to be equal to the freestream temperature. Thus, the temperature of the walls was not monitored during every test. However, the data obtained during those experiments in which the temperature of the walls was measured was used to determine a relation between the freestream temperature and the final wall temperature (i.e., the final ambient temperature). The wall temperature history was reconstructed using the final ambient temperature of the walls and the initial value and curvature of the surface temperature data. This was considered to be an appropriate approach given that both the walls as well as the models are constructed of the same material and are heated by the same stream. The error present in

77

T_w has been approximated to be ±2°C due to the reconstructive method by which it was determined. By replaying the thermal camera data with the ambient temperature set at the two extremes of the ambient temperature data, it was determined that an additional bias error of ±0.24°C was appropriate for T_s (see Appendix C).

4.5.3   FLIR Camera Temperature Drift Correction

The measured temperature values tend to drift during camera operation. The magnitude of the drift tended to be a function of how long the camera had been active prior to testing. One hour of operation would produce an upward drift on the order of 0.5 degrees per minute, whereas three hours of operation would produce a drift, either upward or downward, of up to 0.1 degrees per minute (Figure 44). To correct this, the camera performs an automatic adjustment of its internal shutter every few minutes. The discontinuities introduced into the temperature history by this adjustment cause the Schultz and Jones equation to predict momentary spikes in the heat transfer coefficient and, due to the summation, an overall incorrect result. To avoid this, the auto-adjust was turned off during wind tunnel tests. To compensate for the drift that would occur, a drift test was performed prior to each test. While monitoring an isothermal plate, the camera would be allowed to record temperature data for approximately 4 minutes: the length of a wind tunnel test. The results would be plotted and the slope of the change in mean temperature would be determined. This slope would be used in the post processing of the data obtained during the subsequent wind tunnel test to correct for drift effects.
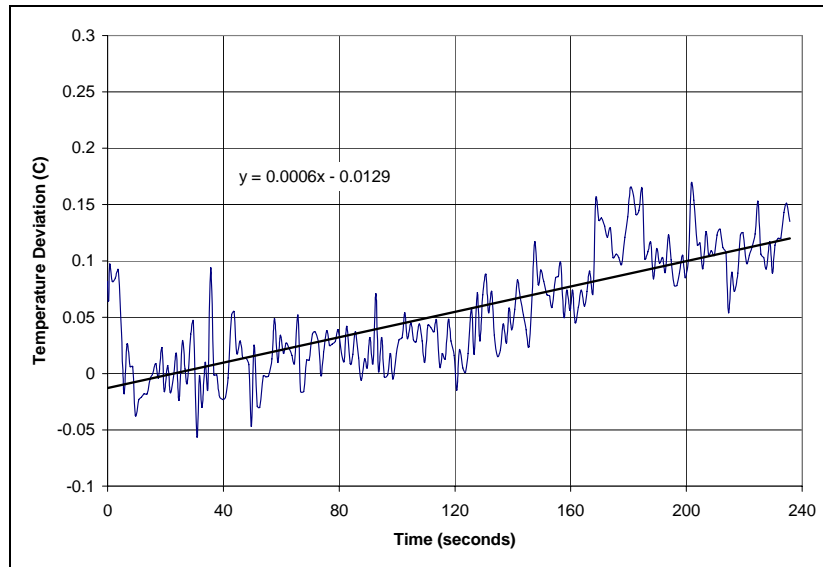
Figure 44. Plot of temperature drift encountered prior to a wind tunnel test.

4.6   Experimental Procedure

Before wind tunnel testing, a roughness model would be placed inside the wind tunnel

test section (see Figure 39). The test section was isolated by blocking off a portion of the

tunnel a short distance upstream of the boundary layer bleed with a sheet of Plexiglas. A

second sheet was taped over the test section exit. The model was allowed time to reach a

near isothermal state—defined for this project as having a temperature difference of

0.6°C or less between the upper and lower surfaces of the model. The temperature

difference was determined with the thermocouple arrangement described in section 4.5.1.

The camera was activated at this point.

Once the model and the camera were ready, the wind tunnel blower was activated and ran

at a frequency of 45 Hz with the flow being ducted through the secondary test section

(see Figure 38). This frequency produces a freestream velocity of approximately 19.5 m/s

79

at room temperature when ducted through the primary test section. Shortly after the blower is turned on, the heating coils are activated. As the flow is heated, a thermocouple mounted in the secondary test section monitors the temperature until steady state is reached. At that point, the recording functions of the computer monitoring the primary test section freestream thermocouple and the computer monitoring the IR camera are activated simultaneously by hand. The Plexiglas sheets blocking off the primary test section are then removed. The butterfly valve closing off the primary test section is quickly opened and the valve leading to the secondary test section is immediately closed. This produces a sudden gust of heated air through the primary test section and over the model. Each test would run for approximately 4 minutes before data collection would be stopped and the heating coils deactivated.

4.7   Stanton Number Determination

One smooth Plexiglas panel, as well as the roughness models based on the four surface measurements of the TBC coated Coupon 3, were tested in the manner described in section 4.6. These tests resulted in surface temperature, freestream temperature, and freestream velocity histories (Figure 45).

Once the temperature histories were obtained, the data were conditioned in Microsoft Excel. First, the surface temperature data produced with the two different ambient temperature settings would be corrected for drift, with the error as a function of time being subtracted from the data. Second, the surface temperature data and the freestream data would be plotted against each other (Figure 45). A slight disparity occurs in the two

time scales since the surface temperatures and the freestream temperatures are recorded on two separate computers.
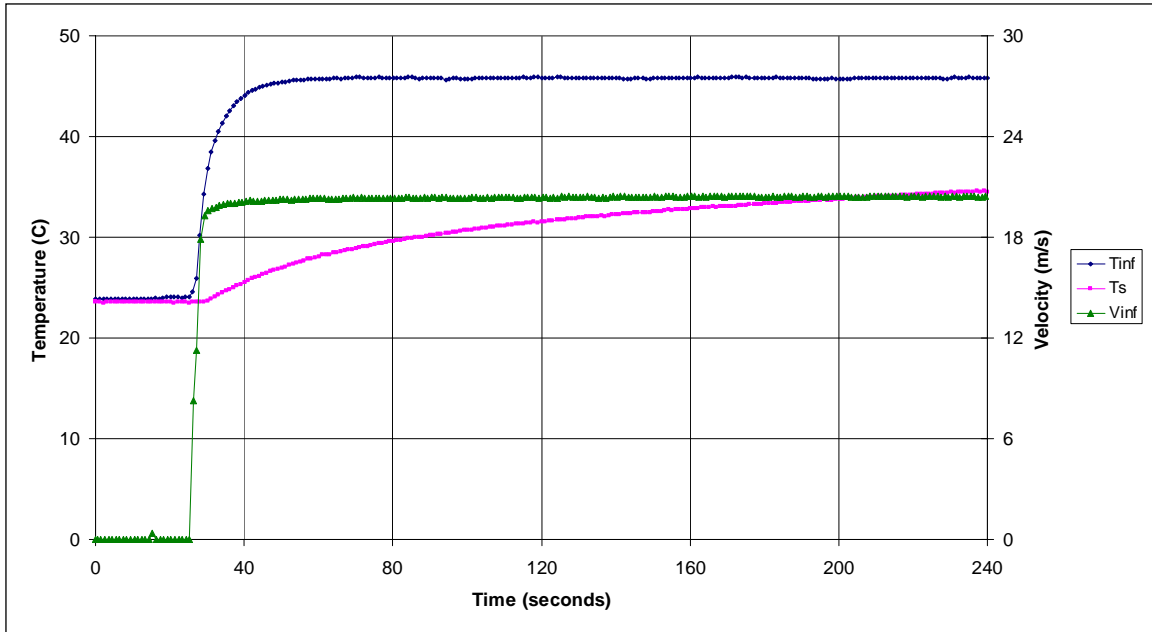
Figure 45. Typical temperature and velocity histories.

Time was either added to or subtracted from the freestream history time scale in order to synchronize the moment in which heated air first flowed over the plate. Synchronization was based on the moment in which both the freestream and the plate began to increase in temperature rather than the moment in which an increase in velocity was measured. An increase in velocity precedes the increase in freestream temperature due to the immediate acceleration of a slug of non-heated air when the butterfly valve is opened. Once the curves were properly aligned, seven columns of data necessary to determine the Stanton number were exported as a tab-delimited text file:

- Column 1: Surface temperature data timescale

- Column 2: Surface temperature with the initial ambient temperature setting

- Column 3: Surface temperature with the final ambient temperature setting

- Column 4: Wall (ambient) temperature data

- Column 5: Freestream temperature timescale

- Column 6: Freestream temperature

- Column 7: Freestream velocity

This text file was exported into the MATLAB program "schultzjones.m" (see Appendix C). Upon activation, this MATLAB program requests the name of the data file to be read and the desired name for the results file. Next, the program asks for the ambient pressure at the time of the test in order to calculate the appropriate air density in the tunnel. Finally, the program asks for the initial and the final ambient temperature settings for the linear interpolation between surface temperature data sets. Hard coded into the program are the thermal properties of Plexiglas G. However, the program can be altered so as to make the properties user-defined.

Although the surface and freestream temperature data are both sampled at a rate of approximately one measurement per second, the sample rate may fluctuate slightly. To compensate, the program interpolates the freestream temperature data, aligning it with the timescale of the surface temperature data. Following this, the program interpolates the two surface temperature data sets as described in section 4.5.2. Once the effect of the ambient temperature on the surface temperature measurements has been compensated for, the correction curve derived from the in situ calibration is applied to further correct the

surface temperature values (section 4.5.1). With the data properly conditioned, the

program performs the operations of the Schultz and Jones equation (Equation 9) to find

the heat flux into the surface. To solve for the convective heat transfer coefficient, the

program performs an energy balance which takes into account thermal radiation

exchange between the model and the wind tunnel walls (Figure 46, Equations 10-12):
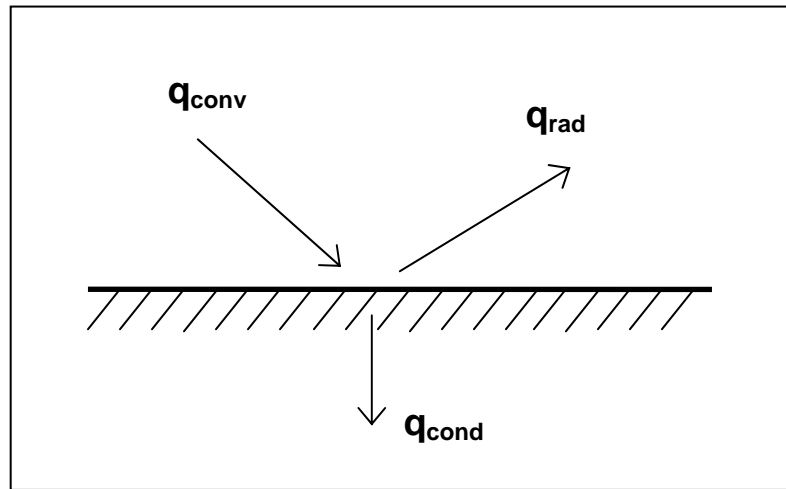
Figure 46. Illustration of heat transfer between a roughness model and the environment.

$$q_{cond} = q_{conv} - q_{rad} \tag{10}$$

$$q_{cond} = hA(T_\infty - T_s) - \varepsilon\sigma A(T_s^4 - T_w^4) \tag{11}$$

$$h = \frac{q''_{cond} + \varepsilon\sigma(T_s^4 - T_w^4)}{T_\infty - T_s} \tag{12}$$

The program results are saved as a text file and are exported back to Excel in order to

determine the moment at which the heat transfer coefficient data—and by association, the

Stanton number data—leveled out (Figure 47). The average and the standard deviation

83

were typically based on 90 seconds or more of data. This represented the period

following the stabilization of the Stanton number and prior to the upturn in the error in

the IR camera measurements of surface temperature that was often encountered

(Figure 44).
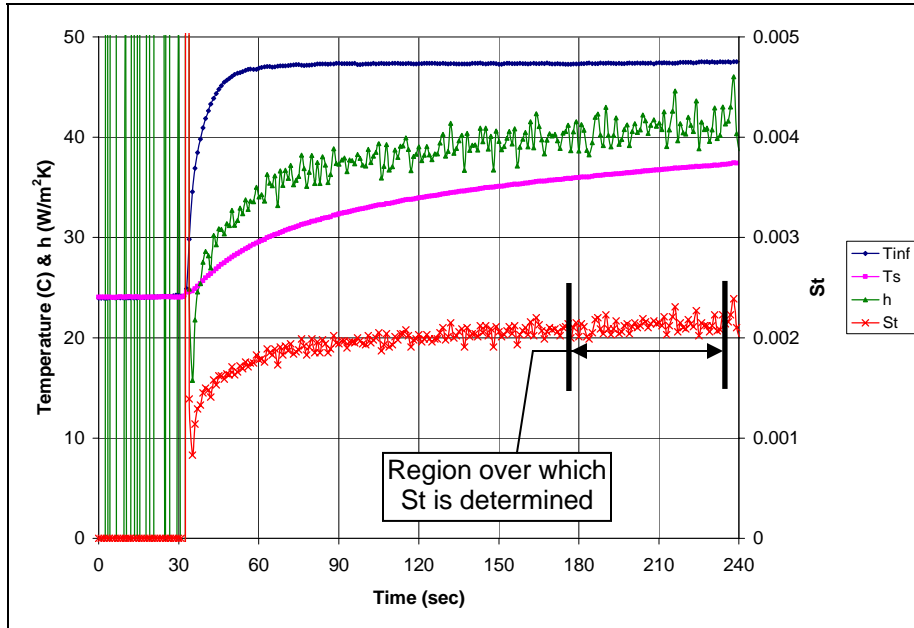
Figure 47. Typical temperature and heat transfer histories. Note the initial instability in h and St.

Chapter 5: Convective Heat Transfer Results

5.1 Stanton Number Correlations

There have been a number of correlations developed which relate the roughness statistics of a surface with its heat transfer properties. In this chapter, several of these correlations are applied to the experimental surface measurements of Coupon 3.

5.1.1 Flat Plate Correlation

The initial heat transfer measurements were made using a smooth, 2.54 cm thick Plexiglas panel. The results obtained with this panel were compared to the results obtained through Kays et al.'s Stanton number correlation for fully turbulent flow over a smooth flat surface with a temperature that is constant with x (Equation 13) (Kays et al, 2005). Because the temperature of the wind tunnel surfaces is not constant with x, use of this Stanton number relation will underestimate the value of St by approximately 3%.

$$St = \frac{0.0287\,\mathrm{Re}_x^{-0.2}}{0.169\,\mathrm{Re}_x^{-0.1}\left(13.2\,\mathrm{Pr} - 9.25\right) + 0.85} \tag{13}$$

This equation assumes that the momentum and thermal boundary layers are of similar thickness with a turbulent Prandtl number of 0.85. It also assumed that the turbulent boundary layer can be adequately described by a $1/7^{\text{th}}$ power law.

Given typical wind tunnel conditions during a test of a flat plate—a freestream temperature of 50.5°C, a freestream velocity of 20.5 m/s, a model location of 1.21 m, and an atmospheric pressure of 86.3 kPa—a Reynolds number of approximately $1.22\text{x}10^6$ is achieved and Equation 13 yields a Stanton number of 0.00204.

5.1.2   Rough Surface Parameters

The majority of Stanton number correlations have been designed to compare the Stanton number of an artificially roughened surface with that of a "real" rough surface. The equivalent sandgrain roughness, k_s, which compares the behavior of any particular rough surface—either roughened with symmetrically placed geometrical structures, packed spheres, real roughness, etc.—with that of a surface roughened with tightly packed sand grains, is widely used in such correlations.

Many Stanton number correlations require that certain parameters of the surface be known. One of the most widely used is the average surface height, k. Although k is often approximated to be Rz, the manner in which the Hommel software solves for Rz tends to result in a high estimate (see section 3.1). Therefore, the raw data for each surface was processed with a MATLAB program to yield an average surface height. For each of the four rough surfaces, the program partitioned the scaled-up version of the surface used for wind tunnel models into 28 full squares having side lengths of 25.5 mm; approximately 10 momentum thicknesses. Excess regions that were too small to be apportioned a full square were omitted. In each square, the difference in height between the highest peak and the lowest valley was found. The value of k was estimated to be the average of these

values. This is similar to the method used by Bons to determine k values for rough

surfaces measured from real turbine blades (Bons, 2005).

A two-dimensional version of k was also found for the four surfaces. This variant of the

average roughness height was developed for use in cases in which three-dimensional

surface maps are unavailable and is based on simple streamwise traces of a surface. In

this method, for every 20 momentum thicknesses of distance along a trace, the seven

largest peak-to-valley distances are averaged (Bons, 2005). An average is then calculated

from the results of each streamwise trace.

A third parameter that is often used in roughness correlations is the shape/density

parameter, Λ_s (also L_s), developed by Sigal and Danberg (1990). This parameter is

defined by Bogard et al. as:

$$\Lambda_s = \left(S \big/ S_f \right) \left(A_s \big/ A_f \right)^{1.6} \tag{14}$$

where S/S_f is the ratio of the surface area without roughness to the total frontal area of the

roughness elements, A_s is the forward projected surface area of the roughness elements,

and A_f is the wetted surface area of those elements (Bogard et al., 1996). Although

originally designed for use with artificially roughened surfaces using systematically

placed roughness elements, Bogard et al. and others have adapted it for use with real,

irregular surfaces.

Finally, with the above parameters the equivalent sand grain roughness may be calculated. A version which varies from the original formulation in order to better apply to real turbine roughness uses average roughness height, k and the shape/density parameter, Λ_s (Bons, 2005):

$$\log\left(\frac{k_s}{k}\right) = -0.43\log(\Lambda_s) + 0.82 \tag{15}$$

Another relation for k_s which uses the two-dimensional k value and the average forward facing angle, $\overline{\alpha}_f$ has also been proposed (Bons, 2005):

$$\frac{k_s}{k} = \frac{0.0191\overline{\alpha}_f^{\;2}}{4} + \frac{0.0736\overline{\alpha}_f}{2} \tag{16}$$

Equation 16 differs from the equation initially proposed by Bons in that the calculation of $\overline{\alpha}_f$ ignores all leeward facing angles. The original relation considers all leeward facing angles to have a value of zero while averaging and omits the 4 and the 2 in the denominator. These roughness parameters may be found in Table 12.

Table 12. Roughness parameters for Coupon 3 (TBC) models.

Burn	1	2	3	4	Notes
k (mm)	2.06	1.96	2.01	2.73	3-D
k (mm)	1.48	1.42	1.46	2.16	2-D
Λ_s	49	72.5	62.7	33.3	-
k_s (mm)	1.78	1.01	1.26	3.91	From Equation 12
k_s (mm)	1.81	1.33	1.41	2.76	From Equation 13

5.1.3 Friction Coefficient Correlations

In order to use most Stanton number correlations, the friction coefficient, c_f, of the surface must be known. Thus, for a purely correlative determination of the nondimensional heat transfer coefficient of a surface to be found, an appropriate relation for the friction coefficient must also be applied. Bons found that the Schlichting friction coefficient most closely matched data taken from real turbine blade surfaces when $k_s > k/2$ (Bons, 2002). Since $k_s > k/2$ for all four Coupon 3 model surfaces, the Schlichting friction coefficient was applied (Schlichting, 1979) (Equation 17).

$$c_f = \left[2.87 + 1.58 \log(x/k_s)\right]^{-2.5} \tag{17}$$

5.1.4 Correlation Results

Two Stanton number correlations were used in this study: one developed by Dipprey and Sabersky (1963) (Equation 18) and one by Kays et al. (2005) (Equation 19).

$$St = \frac{0.5c_f}{1 + \sqrt{0.5c_f}\left(5.19k^{+0.2} \, Pr^{0.44} - 8.5\right)} \tag{18}$$

$$St = \frac{0.5c_f}{Pr_t + \sqrt{0.5c_f}\left(k^{+0.2} \, Pr^{0.44}/C\right)} \tag{19}$$

The value of C in Equation 19 was set as 0.35 due to the discovery that the recommended value of 1 causes the results to diverge from the real roughness data (Bons, 2002). The turbulent Prandtl number, Pr_t, was set at 0.85, which is a typical value for air in an external flow (Kays et al., 2005). The parameter k^+ is often referred to as the roughness

Reynolds number and is in terms of the wall velocity and equivalent sandgrain roughness:

$$k^+ \equiv \mathrm{Re}_k \equiv \frac{k_s u_\tau}{v} = \frac{U_\infty}{v} k_s \sqrt{\frac{c_f}{2}} \qquad (20)$$

Each Stanton number correlation was calculated using the Schlichting friction coefficient equation and either the equivalent sandgrain roughness derived from Equation 15 or the sandgrain roughness derived from Equation 16. This produced a total of four series of Stanton number predictions for the different Coupon 3 surfaces (Figure 48). Note that here Burn 0 refers to the smooth flat plate value rather than to a model representative of preburn surface of Coupon 3.
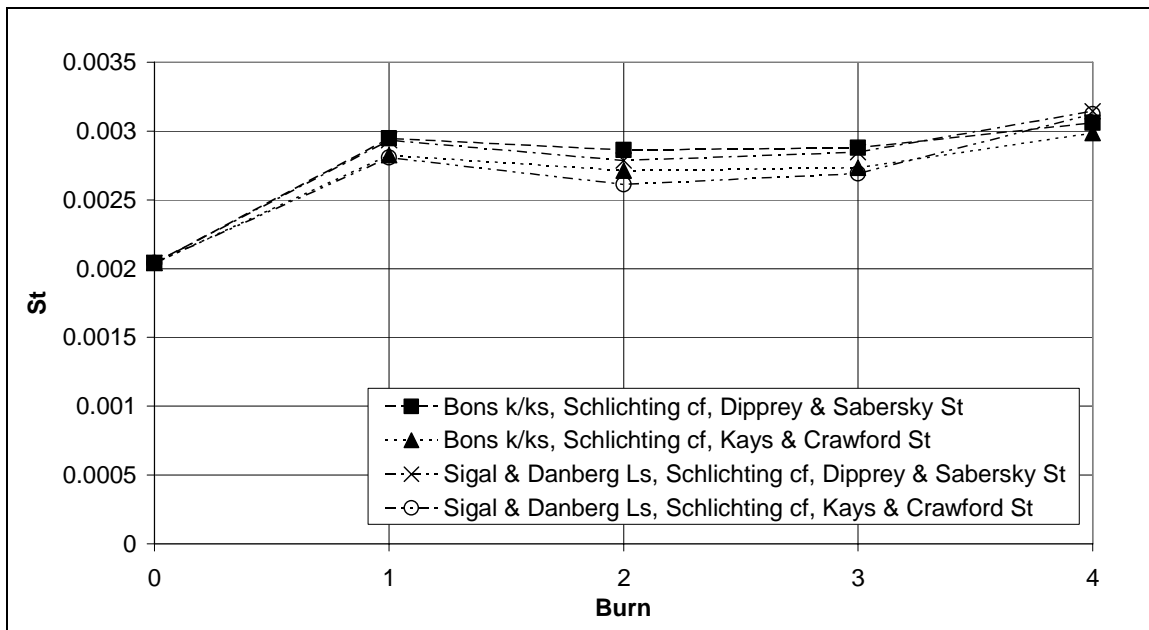
Figure 48. Stanton numbers derived from roughness correlations.

90

The Stanton number predictions clearly show the influence of the drop in the average

forward facing angle between Burns 2 and 3. Despite the increase in the roughness

parameter *Ra*, the Stanton number falls. An interesting illustration of the dependence of

heat transfer rates on the peakedness of the surface occurs when the Stanton number

percentage augmentation with respect to the flat plate value is compared to the average

forward facing angle (Figure 49).
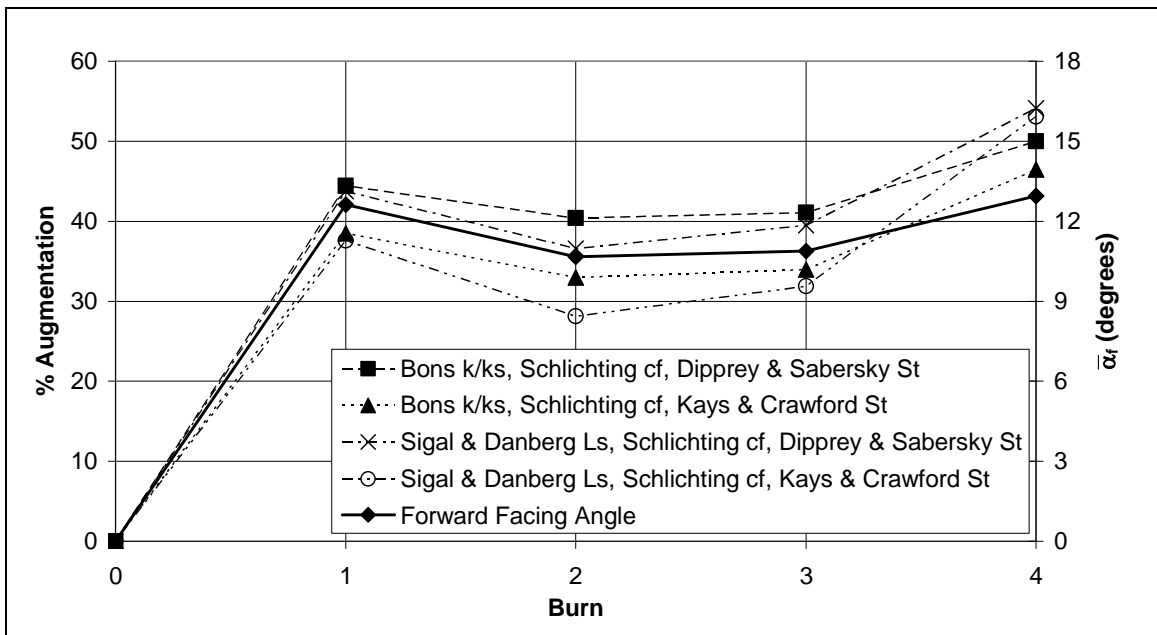
Figure 49. Comparison between trend in forward facing angle and predicted Stanton number percent augmentation.

The dependence of the Stanton number on the average forward facing angle and the

discovery made during this project that the average forward facing angle dropped and

climbed during the deposition process suggest that the heat transfer rate will behave in a

similar manner. Rather than experiencing a continuously increasing rate of heat transfer

during its operation, a turbine blade may see a periodic decline in convective heating.

5.2   Experimental Stanton Number Results

Several series of wind tunnel experiments were performed on the flat plate and the four roughness surfaces during which different techniques and approaches were attempted. Most of these techniques involved different methods of compensating for the changing ambient temperature. The final series of experiments was the most sophisticated and involved the ambient temperature interpolation, in situ calibration, and drift correction described in sections 4.5.1 through 4.5.3. The data obtained during this final series are presented in Figure 50 and Figure 51.

5.2.1   Stanton Number Uncertainty

An uncertainty analysis performed on the final series results gives an average ±6% combined bias and precision error in the measurement of the Stanton number for each experiment. Error sources included noise in electronically gathered data, estimation errors produced by the application of linear fits to temperature and velocity measurements during calibration, and precision limitations of equipment. See Appendix C for details of the uncertainty analysis. Uncertainty with regards to the Plexiglas thermal properties was not included as part of the analysis since the uncertainty in the manufacturer's measurements is not known. However, to provide an estimate of the effect that uncertainties in the material properties would have on the final calculation of Stanton number, calculations of the Stanton number for the flat plate were performed with a 10% change in the value of κ, c_P, and ρ respectively. In each case it was found that a 10% increase would cause the Stanton number to increase by 4.8%. A 10% decrease in either property would lead to a 5% decrease in Stanton number.

5.2.2 Flat Plate

The average Stanton number measured for the flat plate yielded a value that was 21%

lower than that predicted through Kay's relation (section 5.1.1). However, the two

measurements made during the final series of experiments showed excellent repeatability.

This average, labeled as St_0, became the baseline against which the results from the other

plates were judged in the form of a percent augmentation (Figure 50).

5.2.3 Coupon 3, Burn 1

The average Stanton number measured for Burn 1 showed a 22.5% augmentation over

the average flat plate Stanton number (Figure 51). This is well below the augmentation of

40% that the correlations suggest. There is also a large variation between the two points.

The source of this variation is unknown. An uncertainty analysis (Appendix C) shows

that the points are separated by a magnitude great enough to prevent the regions of

uncertainty from overlapping (see error bars in Figure 50).

5.2.4 Coupon 3, Burn 2

The Stanton number of Burn 2 does not follow the expected trend; it appears to climb

slightly despite a reduced k and $\overline{\alpha_f}$ (Figure 50). However, the margin of error is wide

enough to put this into doubt. The average percent augmentation is still lower than

predicted, achieving a value of 24.2% versus an expected percent augmentation lying

between 28.1% and 40.4% (Figure 51). Like Burn 1, Burn 2 also suffers from a large

spread in the data. The percent augmentation for the highest Stanton number value

calculated for Burn 2 is the only point which falls among the values bracketed by the

correlations (Figure 51).
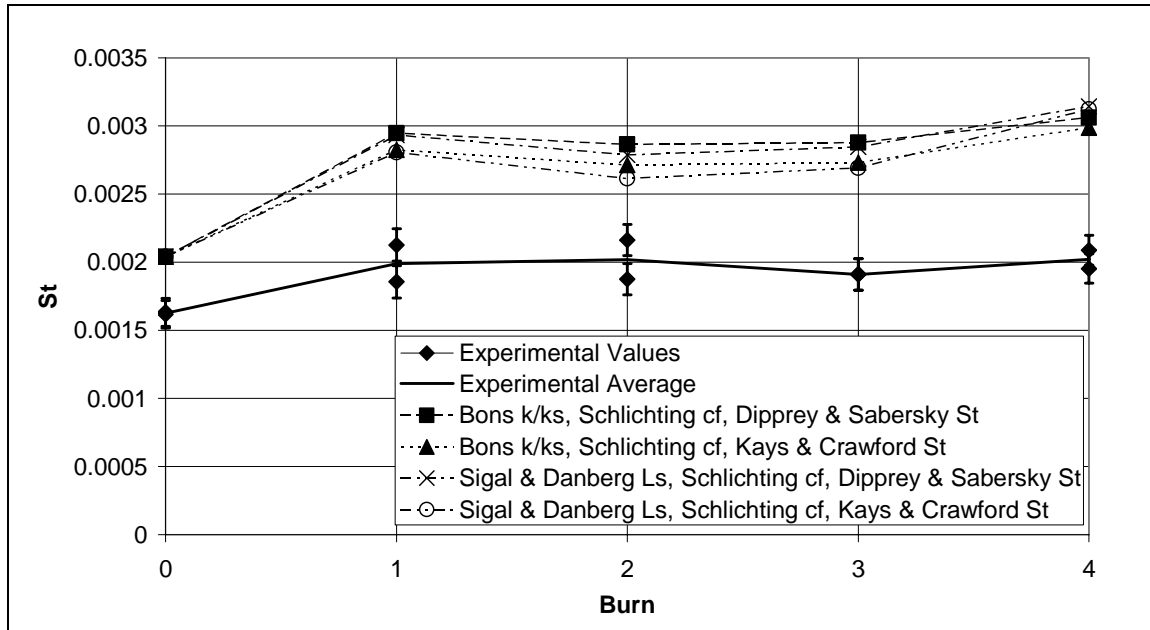
Figure 50. Experimentally derived Stanton numbers compared to Stanton number correlations.

5.2.5   Coupon 3, Burn 3

The average Stanton number for Burn 3 has dropped to an augmentation of 17.6%

(Figure 51), contrary to the expectation of a slight rise. This trend defies the predictions,

given that the four primary roughness parameters discussed, Ra, Rq, Rz, k, and $\overline{\alpha_f}$, all

rose slightly between Burns 2 and 3. The data for Burn 3 have the lowest spread, with

less than a 0.2% discrepancy between the lowest and the highest St values obtained.

5.2.6 Coupon 3, Burn 4

Burn 4 was measured to have an average percent augmentation of 24.3%, which is the highest of the four surfaces. This is to be expected, considering that Burn 4 had the highest values of k and $\overline{\alpha_f}$. However, this may not necessarily be correct given the wide spread in the data for Burns 2 and 3, in addition to the uncertainty involved in each measurement.
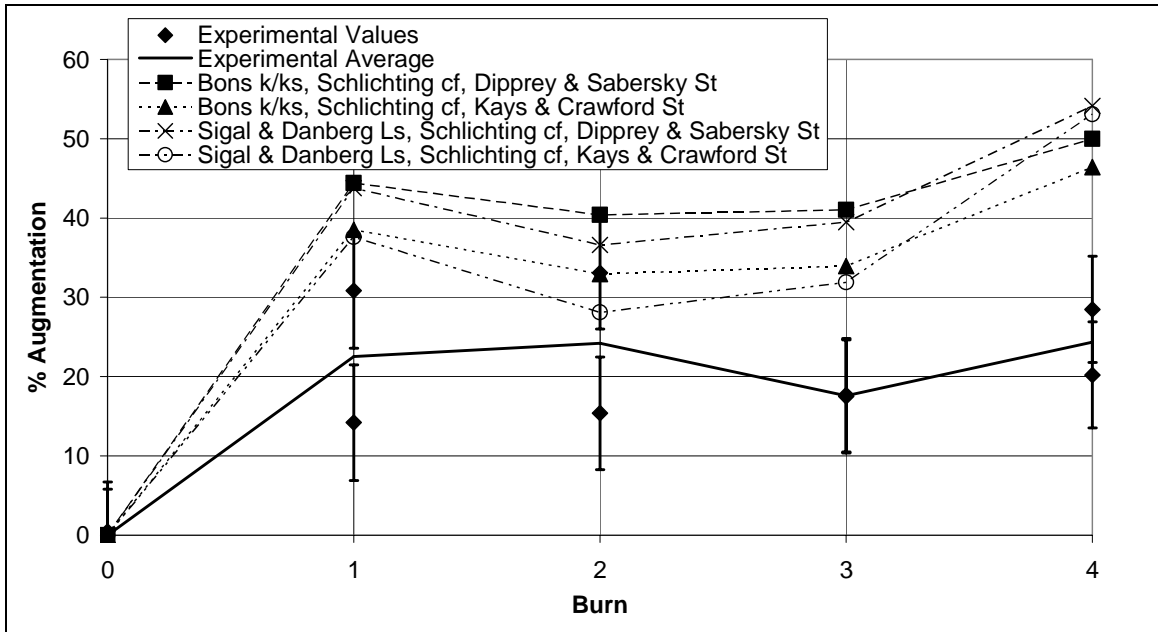
Figure 51. Experimentally derived Stanton number percent augmentation compared to Stanton number correlation results.

5.3 Stanton Number Underprediction

Both the magnitude of the individual Stanton numbers and the percent augmentations fall short of predictions. This proved to be the case in nearly all permutations of the wind tunnel experiments. The failure of the measured values to match the magnitudes

95

predicted by the correlations and the cause for the spread in the data has not yet been discovered. Other than resulting in excessively low Stanton numbers, the data collected for each individual measurement showed no unusual or unexpected behavior. Precautions were taken to ensure that the requirements of the Schultz and Jones equation were met: e.g. thick Plexiglas panels were used to provide a semi-infinite surface and the wind tunnel test section was closed at both ends for several hours to allow it to reach an isothermal state prior to each test. The order in which the models were tested was distributed randomly in order to eliminate the possibility of confusing potential changing conditions (e.g., drifting instruments, malfunctioning equipment, etc.) with real heat transfer trends.

With regards to the method used in this study, the Schultz and Jones equation has been in use for several decades and its derivation has been reviewed by the author. The specific measurement technique has been successfully applied by other investigators. Additionally, the correlations used with the modifications indicated have been shown to bracket the heat transfer data from real turbine blade surfaces (Bons, 2002). Thus, all indications are that the error lies with the data obtained.

It is believed that the instruments behaved correctly due to the calibrations performed and the comparisons made between the results obtained from a variety of measuring devices (e.g., the IR camera was often compared against a Fluke thermocouple reader, the freestream thermocouple was compared against a thermometer). It is also believed that the final approach taken to compensate for the transient ambient temperature was the

most appropriate method available. It is probable that the error lies in the physical aspects of the experiment: the models, the wind tunnel, or both.

As mentioned above, the uncertainty in the physical properties of the Plexiglas is not known. However, it is mentioned in section 5.2.1 that a 10% increase in any of the three relevant material properties would cause a Stanton number increase of only 4.8%. Even if all the magnitude of all three properties had been underestimated by 10%, a correction in the equation would only yield a Stanton number increase of 15.4%. This is far from the 26% increase needed to match the predicted flat plate Stanton number value.

The problem may lie with the wind tunnel, the test section, and the characterization of the test section. First, this study was performed using a freestream velocity that was higher than that for which the tunnel had originally been validated. This could have led to irregularities in the flow such as the unresolved disturbance found in the centerline boundary layer measurements and the asymmetry in the flow about the axis of the tunnel (section 4.4). It may be advisable to repeat the experiments at lower Reynolds numbers. Additionally, the passive boundary layer bleed that was used in the place of active boundary layer suction may have contributed to or even caused some of the flow deviations. There may be a benefit in applying active suction to better control the beginning of the boundary layer in the test section.

Although it was initially deemed that the flow irregularities would have a minimal impact on the heat transfer properties, the behavior of the flow could have changed once the flow

was heated. It may be useful to perform extensive boundary layer measurements while the wind tunnel is operating at higher temperatures. It has already been discovered that temperatures in the core flow of the wind tunnel are 1°C to 2°C lower than temperatures at the edge of the thermal boundary layer at higher speed settings. Measurements of the thermal boundary layer along the centerline and across the width of the tunnel in the vicinity of the model at elevated temperatures may also be helpful.

Until such time that the phenomenon or errors that have caused these underpredictions can be discovered and compensated for, the Stanton numbers for these four surfaces must be determined through experimentally confirmed correlations such as those presented in this chapter.

Chapter 6: Conclusions and Recommendations

6.1   Review of Project Goals

With the development of a facility that can produce realistic turbine blade deposits,

deposit evolution can now be simulated quickly and conveniently. For this project, three

coupons were exposed to deposition conditions with two primary objectives:

- Determine what trend, if any, can be discovered in the manner in which turbine

  blade surface roughness changes over time with deposit evolution.

- Determine the convective heat transfer properties of the roughened surfaces that

  result from accelerated deposit evolution.

6.2   Deposit Evolution

With regards to the first goal: accelerated deposition evolution was observed in all three

coupons. Although the three surfaces were different in their surface coatings and initial

roughness, deposits that changed with time were seen to form on their surfaces. Portions

of the two coupons with the most amount of deposit evolution—the bare substrate

coupon, Coupon 2, and the TBC coated coupon, Coupon 3—displayed an interesting

trend. The roughness in the form of *Ra* would increase rapidly with an accompanying

increase in average forward facing angle. The rate of roughness increase would then

subside slightly and the average forward facing angle would decrease. This would then be

followed by another increase in roughness and surface angle. These results show that

deposition evolution is not limited to a slow, linear process, but that it often occurs in relatively rapid jumps.

6.3   Recommendations Regarding Deposition Evolution

It is hoped that the trends seen in Coupons 2 and 3 will serve as a motivation for further study. It may be useful to expose multiple coupons to many more than four burns in order to determine whether or not the trend noted during this project is a common one and whether or not it is continuous. It would also be of interest to determine whether or not this phenomenon occurs regularly in real gas turbines. If that proves to be the case then the condition of a turbine blade at one point in its cycle could be used as an indicator for the upcoming conditions. For example, if a blade were found to have peak-dominated deposits and a high average forward facing angle, it could be predicted that the blade roughness would soon plateau, the average forward facing angle would drop, and the value of Rz would go down. This would be accompanied by a slackening in the convective heat transfer rate. A wavier surface with a lower value of $\overline{\alpha_f}$ and Rz could mean that a spike in roughness and an increase in convective heat transfer is about to occur. If substantial deposits already exist, the operator might want to choose that moment to service the turbine.

6.4   Heat Transfer Rate Determination

While the deposition evolution followed an unexpected trend, its overall behavior (i.e. a constant increase in surface roughness, Ra) had been expected. The Stanton numbers

obtained through wind tunnel testing, however, did not behave as expected or as predicted through Stanton number correlations. Low Stanton number measurements and percent augmentations were the common result of several series of convective heat transfer tests. The fact that a variety of different approaches to compensating for changing ambient temperatures and calibrating measuring equipment resulted in the same type of error suggests that the problem is physically rather than analytically based.

6.5   Recommendations on Heat Transfer Rate Determination

The first task in determining the cause of the drop in Stanton number would be to further validate the wind tunnel test section. This process should be performed at a temperature equivalent to those reached during a convective heat transfer test. It may also be useful to investigate the effect of lower Reynolds numbers or active boundary layer suction on Stanton number results.

6.6   Accomplishments

During the course of this study, there were several accomplishments of note:

- The Turbine Accelerated Deposition Facility was modified to allow improved burning, ease of use, and more accurate measurement of important parameters such as air flow rate and Mach number.

- Accelerated deposits were formed with surface features that compare favorably with deposits found on real turbine blades (Table 7). This further corroborates the principle of accelerated deposition as a means to accurately simulate real deposition.

- Deposits were evolved on three coupons simulating approximately one year's worth of deposition.

- Distinct trends were discovered with respect to the evolution of certain roughness parameters over time. Studies have shown that these parameters have a strong influence on heat transfer properties.

- A simple and inexpensive method for constructing scaled-up models of roughened surfaces was developed and implemented, producing four models representing four distinct stages in the evolution of turbine blade deposits.

- Roughness correlations for the prediction of the Stanton number were applied to the four surfaces, producing a probable Stanton number history for the surface.

- A wind tunnel test section was designed and constructed for the purpose of convective heat transfer experimentation using the scaled-up roughness panels.

- Numerous experiments with the panels indicate that further characterization is required in order to obtain appropriate values.

Bibliography

Antonia, R. A., and Luxton, R. E., 1971, "The Response of a Turbulent Boundary Layer to a Step Change in Surface Roughness. Part 1: Smooth to Rough," ASME J. Fluid Mech. 48, pp. 721–726.

Blair, M. F., 1994, "An Experimental Study of Heat Transfer in a Large-Scale Turbine Rotor Passage," ASME J. Turbomach., 116, No. 1, pp. 1-13.

Bogard, D. G., Schmidt, D. L., and Tabbita, M., "Characterization and Laboratory Simulation of Turbine Airfoil Surface Roughness and Associated Heat Transfer," 96-GT-386, (1996), (presented at the Gas Turbine and Aeroengine Congress & Exhibition, Birmingham, UK, June 10-13, 1996).

Bons, J.P., Taylor, R., McClain, S., and Rivir, R.B., "The Many Faces of Turbine Surface Roughness," ASME J. Turbomach., 123, No. 4, pp. 739-748.

Bons, J.P., 2002, "St and C_f Augmentation for Real Turbine Roughness with Elevated Freestream Turbulence," Transactions of the ASME, vol. 124, OCT 2002, pgs 632-644.

Bons, J.P., 2005, "A Critical Assessment of Reynolds Analogy for Turbine Flows," Transactions of the ASME, vol. 127, MAY 2005, pgs 472-485.

Borom, Marcus P., Johnson, Curtis A., and Peluso, Louis A., 1996, "Role of environmental deposits and operating surface temperature in spallation of air plasma sprayed thermal barrier coatings," Surface and Coatings Technology 86-87, pp.116-126.

Boynton, J. L., Tabibzadeh, R., and Hudson, S. T., 1993, "Investigation of Rotor Blade Roughness Effects on Turbine Performance," ASME J. Turbomach., 115, pp. 614-620.

Dipprey, D. F., and Sabersky, R. H., 1963, "Heat and Momentum Transfer in Smooth and Rough Tubes at Various Prandtl Numbers," Int. J. Heat Mass Transfer, 6, pp. 329–353.

Ford, W.E., (revision), *Dana's Textbook of Mineralogy* (after E.S. Dana) 4th edn., 16th printing, John Wiley & Sons, NY 1954, p379.

Incropera, F.P., and DeWitt, D.P., *Fundamentals of Heat and Mass Transfer* 5th edn., John Wiley & Sons, NY 2002.

Jensen, J. W., 2004, "The Development of an Accelerated Testing Facility for the Study of Deposits In Land-Based Gas Turbine Engines," M.S. Thesis, Brigham Young University, Provo, Utah.

Jensen, J. W., Squire, S. W., and Bons, J. P., 2005, "Simulated Land-Based Turbine Deposits Generated in an Accelerated Deposition Facility," ASME J. Turbomach., 127, pp. 462-470.

Kays, W. M., Crawford, M. E., and Weigand, B., *Convective Heat and Mass Transfer, 4th* Edition, 2005, McGraw-Hill, New York, NY.

Kim, J., Dunn, M.G., and Baran, A.J. et al, 1993, "Deposition of Volcanic Materials in the Hot Sections of Two Gas Turbine Engines," ASME J. Engr. Gas Turbines & Power, 115, pp. 641-651.

Schlichting, H., *Boundary Layer Theory,* 7th Edition, 1979, McGraw-Hill, New York, NY.

Schultz, D. L., and Jones, T. V., 1973, "Heat-transfer Measurements in Shortduration Hypersonic Facilities," Advisory Group for Aerospace Research and Development, No. 165, NATO.

Sigal, A., and Danberg, J. E., "New Correlation of Roughness Density Effects on the Turbulent Boundary Layer," AIAA Journal, vol. 28, pp. 554-556.

Smialek, J.L., Archer, F.A., and Garlick, R.G. in F.H. Froes et al. (eds.), *The Chemistry of Saudi Arabian Sand: A Deposition Problem on Helicopter Turbine Airfoils, Advances in Synthesis and Processes*, SAMPE, 3, 1992, M92-M101.

Stripf, M., Schulz, A., and Wittig, S., 2005, "Surface Roughness Effects on External Heat Transfer of a HP Turbine Vane," ASME J. Turbomach., 127, pp. 200-208.

Tabakoff, W., Metwally, M., and Hamed, A., 1995, "High-Temperature Coatings for
Protection Against Turbine Deterioration," Transactions of the ASME, vol. 117,
JAN 1995, pgs 146-151.

Tarada, F., and Suzuki, M., 1993, "External Heat Transfer Enhancement to
Turbine Blading Due to Surface Roughness," ASME Paper No. 93-GT-74.

Taylor, R. P., and Chakroun, W. M., 1992, "Heat Transfer in the Turbulent Boundary
Layer with a Short Strip of Surface Roughness," AIAA Paper No. 92-0249.

Toriz, F.C., Thakker, A.B., and Gupta, S.K., J. ASME, "Thermal Barrier Coatings for Jet
Engines" 88-GT-279, (1988), (presented at the Gas Turbine and Aeroengine
Congress Amsterdam, The Netherlands, June 6-9, 1988).

Wenglarz, R.A., and Fox, R.G. Jr., 1990, "Physical Aspects of Deposition From Coal-
Water Fuels Under Gas Turbine Conditions," ASME J. Engr. Gas Turbines &
Power, Jan 1990, pp. 9-14.

Wenglarz, R.A., and Wright, I.G., "Alternate Fuels for Land-Based Turbines," published
in proceedings of the "Workshop on Materials and Practices to Improve
Resistance to Fuel Derived Environmental Damage in Land-and Sea-Based
Turbines," October 22-24, 2002, Colorado School of Mines, Golden, Colorado.

Appendix

Appendix A: Derivation of the Schultz and Jones Equation

The heat diffusion equation:

$$\frac{\partial}{\partial x}\left(\kappa\frac{\partial T}{\partial x}\right) + \frac{\partial}{\partial y}\left(\kappa\frac{\partial T}{\partial y}\right) + \frac{\partial}{\partial z}\left(\kappa\frac{\partial T}{\partial z}\right) + \dot{q} = \rho c\frac{\partial T}{\partial t} \tag{A.1}$$

Assume one-dimensional heat flux with no heat generation and constant properties:

$$\frac{\partial}{\partial x}\left(\kappa\frac{\partial T}{\partial x}\right) = \kappa\frac{\partial^2 T}{\partial x^2} = \rho c\frac{\partial T}{\partial t} \tag{A.2}$$

$$\frac{\partial^2 T}{\partial x^2} = \frac{1}{\alpha}\frac{\partial T}{\partial t} \tag{A.3}$$

Apply Laplace transform:

$$\frac{\partial^2 \overline{T}(s)}{\partial x^2} = \frac{1}{\alpha}\left[s\overline{T}(s) - T(0)\right] \tag{A.4}$$

$$\frac{\partial^2 \overline{T}}{\partial x^2} = \frac{s}{\alpha}\overline{T} \rightarrow \frac{\partial^2 \overline{T}}{\partial x^2} - \frac{s}{\alpha}\overline{T} = 0 \tag{A.5}$$

Auxiliary equation:

$$m^2 + (0)m - \frac{s}{\alpha} = 0 \rightarrow m = \pm\sqrt{\frac{s}{\alpha}} \tag{A.6}$$

$$\overline{T} = c_1 e^{x\sqrt{s/\alpha}} + c_2 e^{-x\sqrt{s/\alpha}} \tag{A.7}$$

Transform boundary conditions,

$$-\kappa \frac{\partial T}{\partial x} = \dot{q}'' \rightarrow -\kappa \frac{\partial \overline{T}}{\partial x} = \overline{\dot{q}''} \ @ \ x = 0, \overline{T}(x = \infty) = 0 \tag{A.8}$$

Substitute:

$$\overline{T}(x = \infty) = 0 = c_1 e^{(\infty)\sqrt{s/\alpha}} + c_2 e^{-(\infty)\sqrt{s/\alpha}} \rightarrow c_1 = 0 \tag{A.9}$$

$$\frac{\partial \overline{T}}{\partial x} = -c_2 \sqrt{s/\alpha} \, e^{-(0)\sqrt{s/\alpha}} = \frac{-\overline{\dot{q}''}}{\kappa} \rightarrow c_2 = \frac{\overline{\dot{q}''}}{\kappa \sqrt{s/\alpha}} \tag{A.10}$$

$$\overline{T} = \frac{\overline{\dot{q}''}\sqrt{\alpha}}{\kappa \sqrt{s}} e^{-x\sqrt{s/\alpha}} \tag{A.11}$$

At the surface, x=0:

$$\overline{T}_s = \frac{\overline{\dot{q}''}\sqrt{\alpha}}{\kappa \sqrt{s}} \rightarrow \overline{\dot{q}''} = \frac{\kappa}{\sqrt{\alpha}} \overline{T}_s \sqrt{s} \tag{A.12}$$

$$\overline{\dot{q}''} = \frac{\kappa}{\sqrt{\alpha}} s\overline{T}_s \frac{1}{\sqrt{s}} = \frac{\kappa}{\sqrt{\alpha}} \left(s\overline{T}_s\right)\left(\frac{1}{\sqrt{s}}\right) \tag{A.13}$$

Let $F(s) = s\overline{T}_s$ and $G(s) = \dfrac{1}{\sqrt{s}}$, invert the transform:

$$\dot{q}'' = \frac{\kappa}{\sqrt{\alpha}} \int_0^t \frac{dT}{d\tau} \frac{1}{\sqrt{\pi(t-\tau)}} d\tau = \frac{\kappa}{\sqrt{\pi\alpha}} \int_0^t \frac{\dfrac{dT}{d\tau}}{\sqrt{t-\tau}} d\tau \tag{A.14}$$

110

Integrate by parts, for $\tau=0$, $T(\tau)=0$:

$$\dot{q}'' = \frac{\kappa}{\sqrt{\pi\alpha}} \left[\frac{T(t)}{\sqrt{t}} + \frac{1}{2} \int_0^t \frac{T(t) - T(\tau)}{(t-\tau)^{3/2}} d\tau \right] \tag{A.15}$$

Assuming small departures from a uniform rate of heat transfer:

$$\overline{T}(\tau) = T(t_{i-1}) + \frac{T(t_i) - T(t_{i-1})}{\Delta t}(\tau - t_{i-1}) \tag{A.16}$$

Where $t_{i-1} \le \tau \le t_i$ and $i=1, 2, 3,\ldots,n$. Evaluate integral:

$$R = \frac{1}{2} \int_0^t \frac{T(t) - T(\tau)}{(t-\tau)^{3/2}} d\tau = \frac{1}{2} \sum_{i=1}^n \int_{t_{i-1}}^{t_i} \frac{T(t_n) - \overline{T}(\tau)}{(t_n - \tau)^{3/2}} d\tau \tag{A.17}$$

$$= \frac{1}{2} \sum_{i=2}^n \left\{ [T(t_n) - T(t_{i-1})] \int_{t_{i-1}}^{t_i} \frac{d\tau}{(t_n - \tau)^{3/2}} - \left[\frac{T(t_i) - T(t_{i-1})}{\Delta t} \right] \int_{t_{i-1}}^{t_i} \frac{(\tau - t_{i-1})}{(t_n - \tau)^{3/2}} d\tau \right\} \tag{A.18}$$

Evaluate the first integral:

$$\int_{t_{i-1}}^{t_i} \frac{d\tau}{(t_n - \tau)^{3/2}} = \int_{t_{i-1}}^{t_i} (t_n - \tau)^{-3/2} d\tau = 2\left[\frac{1}{\sqrt{t_n - t_i}} - \frac{1}{\sqrt{t_n - t_{i-1}}} \right] \tag{A.19}$$

Evaluate the second integral using integration by parts:

$$\int_{t_{i-1}}^{t_i} \frac{(\tau - t_{i-1})}{(t_n - \tau)^{3/2}} d\tau = \frac{2\Delta t}{(t_n - t_i)^{1/2}} + 4\left[(t_n - t_i)^{1/2} - (t_n - t_{i-1})^{1/2} \right] \tag{A.20}$$

Substitute back into the original equation:

$$R = \frac{1}{2}\sum_{i=1}^{n} 2\left[T(t_n) - T(t_{i-1})\right]\left[\frac{1}{\sqrt{t_n - t_i}} - \frac{1}{\sqrt{t_n - t_{i-1}}}\right] - \left[\frac{T(t_i) - T(t_{i-1})}{\Delta t}\right]\left\{\frac{2\Delta t}{(t_n - t_i)^{1/2}} + 4\left[\sqrt{t_n - t_i} - \sqrt{t_n - t_{i-1}}\right]\right\} \quad (A.21)$$

$$R = \sum_{i=1}^{n}\frac{T(t_n) - T(t_i)}{\sqrt{t_n - t_i}} - \sum_{i=1}^{n}\frac{T(t_n) - T(t_{i-1})}{\sqrt{t_n - t_{i-1}}} + 2\sum_{i=1}^{n}\frac{T(t_i) - T(t_{i-1})}{\sqrt{t_n - t_i} + \sqrt{t_n - t_{i-1}}} \quad (A.22)$$

At $i=n$ $\dfrac{T(t_n) - T(t_i)}{\sqrt{t_n - t_i}}$ is indeterminate. However, $T(t)$ was assumed to be piecewise linear:

$$R = \sum_{i=1}^{n-1}\left\{\frac{T(t_n) - T(t_i)}{\sqrt{t_n - t_i}} - \frac{T(t_n) - T(t_{i-1})}{\sqrt{t_n - t_{i-1}}} + 2\frac{T(t_i) - T(t_{i-1})}{\sqrt{t_n - t_i} + \sqrt{t_n - t_{i-1}}} + \frac{T(t_n) - T(t_{n-1})}{\sqrt{\Delta t}}\right\} (A.23)$$

For $t_0=0$, $T(t_0)=0$

$$R = \sum_{i=1}^{n} 2\frac{T(t_i) - T(t_{i-1})}{\sqrt{t_n - t_i} + \sqrt{t_n - t_{i-1}}} \quad (A.24)$$

Substitute back into equation:

$$\dot{q}" = \frac{2\kappa}{\sqrt{\pi\alpha}}\left[\frac{T(t_n)}{\sqrt{t_n}} + \sum_{i=1}^{n} 2\frac{T(t_i) - T(t_{i-1})}{\sqrt{t_n - t_i} + \sqrt{t_n - t_{i-1}}}\right] \quad (A.25)$$

$\dfrac{T(t_n)}{\sqrt{t_n}} = 0$ when $t_0=0$:

$$\dot{q}" = \frac{2\kappa}{\sqrt{\pi\alpha}}\sum_{i=1}^{n}\frac{T(t_i) - T(t_{i-1})}{\sqrt{t_n - t_i} + \sqrt{t_n - t_{i-1}}} \quad (A.26)$$

$$\dot{q}" = \frac{2\kappa}{\sqrt{\pi\alpha}}\sum_{j=1}^{i}\frac{T_{S,j} - T_{S,j-1}}{\sqrt{t_i - t_j} + \sqrt{t_i - t_{j-1}}} \quad (A.27)$$

112

Appendix B: MATLAB Programs

schultzjones.m

This program uses conditioned temperature and velocity histories to determine the

Stanton number of a surface tested in a wind tunnel. The results are output to a text file.

```
% schultzjones.m
% Written by James Wammack 06/01/05
% Modified 08/11/05
% This program uses the Shultz and Jones equation to determine the heat
% transfer coefficient given a set of temperature data

clear all;
warning off;

% Obtain user inputs
infile = input('Enter name of input file with its extension: ','s');
outfile = input('Enter name of output file with its extension: ','s');

% For user defined properties
% k = input('Enter model thermal conductivity value in W/m*K: ');
% cp = input('Enter model specific heat in J/kg*K: ');
% rho = input('Enter model density in kg/m^3: ');
% epsilon = input('Enter model emissivity: ');

% Plexiglas G properties
k = 0.18733;
cp = 1464.4;
rho = 1190;
epsilon = 0.9;

% Bons' model properties
% k = 0.226;
% cp = 1913;
% rho = 1207;

press_eng = input('Enter pressure in psf:');
Tamb1 = input('Enter initial ambient temperature: ');
Tamb2 = input('Enter final ambient temperature: ');

alpha = k/(rho*cp);

% Read topological data into MATLAB
```

```
M = dlmread(infile,'\t');

% Separate data into times, freestream temperature, surface temperature,
% and velocity matrices

% For data sets with two different ambient temperatures
Ts_data = M(1:size(M,1),1:4);
Tinf_data = M(1:size(M,1),5:7);
Ts1 = Ts_data(:,2);
Ts2 = Ts_data(:,3);
Tw = Ts_data(:,4);

% % For data sets with one ambient temperature
% Ts_data = M(1:size(M,1),1:2);
% Tinf_data = M(1:size(M,1),3:5);
% Ts = Ts_data(:,2);

t = Ts_data(:,1);

% Interpolate Tinf data based on Ts data's time scale
for i=1:size(t,1)
    for j=1:(size(Tinf_data,1)-1);
        if Tinf_data(j,1)<t(i) && Tinf_data(j+1,1)>t(i)
            Tinf(i) = Tinf_data(j+1,2)-(Tinf_data(j+1,2)-Tinf_data(j,2))*...
                ((Tinf_data(j+1,1)-t(i))/(Tinf_data(j+1,1)-Tinf_data(j,1)));
            Vinf(i) = Tinf_data(j+1,3)-(Tinf_data(j+1,3)-Tinf_data(j,3))*...
                ((Tinf_data(j+1,1)-t(i))/(Tinf_data(j+1,1)-Tinf_data(j,1)));
        elseif Tinf_data(j,1)==t(i)
            Tinf(i) = Tinf_data(j,2);
            Vinf(i) = Tinf_data(j,3);
        end
    end
end

if size(t,1)==size(Tinf,2)+2
    Tinf(size(t,1)-1)=Tinf(size(t,1)-2);
    Vinf(size(t,1)-1)=Vinf(size(t,1)-2);
    Tinf(size(t,1))=Tinf(size(t,1)-1);
    Vinf(size(t,1))=Vinf(size(t,1)-1);
elseif size(t,1)==size(Tinf,2)+1
    Tinf(size(t,1))=Tinf(size(t,1)-1);
    Vinf(size(t,1))=Vinf(size(t,1)-1);
end

% Interpolate between TsIR at Tamb,i and Ts at Tamb,f
for i=1:size(t,1)
    TsIR(i) = Ts1(i)+(Ts2(i)-Ts1(i))*((Tinf(i)-Tamb1)/(Tamb2-Tamb1));
end

% Apply In Situ calibration
Ts = 0.95176*TsIR+1.97913;

Ts(1)=Ts(2);
Tsize = size(Tinf,2);

if Tsize<size(Ts,1)
```

```matlab
      for i=Tsize:size(Ts,1)
        Tinf(i) = Tinf(Tsize);
        Vinf(i) = Vinf(Tsize);
      end
  end

% Perform Shultz & Jones equation
for i=1:size(t,1)
    inner = 0;
    summation = 0;
    for j=1:i
      if j==1
        inner(j) = 0;
      else
        inner(j) = (Ts(j)-Ts(j-1))/(sqrt(t(i)-t(j))+sqrt(t(i)-t(j-1)));
      end
    end
    summation = sum(inner);
    qc(i) = (2*k/sqrt(pi*alpha))*summation;
end

% Perform radiation compensation
sigma = 5.67*10^-8;

for i=1:size(t,1)
    qr(i) = epsilon*sigma*(Ts(i)^4-Tw(i)^4);
    h(i) = (qc(i)+qr(i))/(Tinf(i)-Ts(i));
end

% Determine Stanton Number
pressure = (press_eng/144)*6894.757;

for i=1:size(t,1)
    if Vinf(i)~=0;
      rho(i) = pressure/(287*(Tinf(i)+273.15));
      St(i) = h(i)/(rho(i)*Vinf(i)*1005.5);
    else
      St(i) = 0;
    end
end

% Print data to a text file
fid=fopen(outfile,'at');
fprintf(fid,'Time\tTinf\tTs\th\tSt\n');

% for a=1:size(t,2)
for a=1:size(t,1)
    fprintf(fid,'%.2f\t%.2f\t%.2f\t%.3f\t%.5f\n',t(a),Tinf(a),Ts(a),h(a),St(a));
end

fclose(fid);

% Plot data
subplot(2,1,1)
plot(t,Tinf,'-',t,Ts,'--',t,h,'-.');
axis([0 max(t) 0 80]);
```

```
grid on;
legend('T_i_n_f','T_S','h',4);
title('Temperature and Heat Transfer Coefficient History');
xlabel('Time (sec)');
ylabel('Temperature(C), Heat Transfer Coefficient (W/m^2 K)');

subplot(2,1,2)
plot(t,St);
grid on;
title('St history');
xlabel('Time (sec)');
ylabel('St');
```

angles.m

This program determines the roughness slope angles of a surface in both the cross-stream

and the streamwise directions. It also computes their statistics and outputs the results to

the screen and to a text file.

```
% Written by James Wammack 04/01/05
% Modified 06/18/05
% This program reads roughness coordinates, determines the angle from the
% horizontal from point to point and calculates the statistics

clear all;
warning off;

% Obtain user inputs
infile = input('Enter name of input file with its extension:','s');
outfile = input('Enter name of output file with its extension:','s');

% Begin counting time
tic;

% Read topological data into MATLAB
M0 = csvread(infile);

t1 = toc/60;
fprintf('Data file read:\t%.2f minutes\n',t1);

% Determine number of rows and columns
rows = 1;
for i=2:size(M0,1)
   if M0(i,2) ~= M0(i-1,2)
      rows = rows+1;
   end
end
points = size(M0,1)/rows;
```

```matlab
% Truncate data with respect to Y
for i=1:(rows/2)
    Mtruncy((points*i-(points-1)):points*i,:) = M0((points*(2*i-1)-(points-1))...
        :points*(2*i-1),:);
end

% Truncate data with respect to X
for i=1:(size(Mtruncy,1)/2)
    Mtruncxy(i,:) = Mtruncy((2*i-1),:);
end

% Determine new number of rows and points
rows2 = 1;
for i=2:size(Mtruncxy,1)
    if Mtruncxy(i,2) ~= Mtruncxy(i-1,2)
        rows2 = rows2+1;
    end
end
points2 = size(Mtruncxy,1)/rows2;

t2 = toc/60;
fprintf('Data truncated with respect to X and Y:\t%.2f minutes\n',t2);

% X column
Mx = Mtruncxy(1:size(Mtruncxy,1),1);

% Y column
My = Mtruncxy(1:size(Mtruncxy,1),2);

% Z column
Mz = Mtruncxy(1:size(Mtruncxy,1),3);

% Determine angles in X direction
for i=2:(size(Mz,1))
    deltax(i-1) = Mx(i)-Mx(i-1);
    if deltax(i-1)<0
        deltax(i-1) = Mx(i+1)-Mx(i);
    end
    deltaxz(i-1) = Mz(i)-Mz(i-1);
    anglex(i-1) = abs((atan(deltaxz(i-1)/deltax(i-1)))*180/pi);
end

anglex_mean = mean(anglex);
anglex_med = median(anglex);
anglex_dev = std(anglex);
anglex_skew = skewness(anglex);

% Determine forward-facing and rearward-facing angles in Y direction
j = 0;
k = 0;

for i=1:(size(Mz,1)-points2)
    deltay(i) = My(points2+i)-My(i);
    deltayz(i) = Mz(points2+i)-Mz(i);
    angley(i) = (atan(deltayz(i)/deltay(i)))*180/pi;
```

```
    if angley(i)<=0
        j = j+1;
        forwardangle(j) = abs(angley(i));
    elseif angley(i)>0
        k = k+1;
        rearangle(k) = abs(angley(i));
    end
end

forwardangle_mean = mean(forwardangle);
forwardangle_med = median(forwardangle);
forwardangle_dev = std(forwardangle);
forwardangle_skew = skewness(forwardangle);

rearangle_mean = mean(rearangle);
rearangle_med = median(rearangle);
rearangle_dev = std(rearangle);
rearangle_skew = skewness(rearangle);

t3 = toc/60;

fprintf('Angle data found:\t%.2f minutes\n',t3);

% Y plane screen printouts
fprintf('Analysis in the streamwise (Y) direction\n');
fprintf('Average forward-facing angle:\t%.2f degrees\n',forwardangle_mean);
fprintf('Median forward-facing angle:\t%.2f degrees\n',forwardangle_med);
fprintf('Standard deviation of forward-facing angles:\t%.2f degrees\n',forwardangle_dev);
fprintf('Skewness of forward-facing angles:\t%.2f degrees\n\n',forwardangle_skew);

fprintf('Average rearward-facing angle:\t%.2f degrees\n',rearangle_mean);
fprintf('Median rearward-facing angle:\t%.2f degrees\n',rearangle_med);
fprintf('Standard deviation of rearward-facing angles:\t%.2f degrees\n',rearangle_dev);
fprintf('Skewness of rearward-facing angles:\t%.2f degrees\n\n',rearangle_skew);

% X plane screen printouts
fprintf('Analysis in the cross-stream (X) direction\n');
fprintf('Average roughness angle:\t%.2f degrees\n',anglex_mean);
fprintf('Median roughness angle:\t%.2f degrees\n',anglex_med);
fprintf('Standard deviation of angles:\t%.2f degrees\n',anglex_dev);
fprintf('Skewness of angles:\t%.2f degrees\n\n',anglex_skew);

% Produce histogram of angles
bins = 50;
for i=1:bins
    % Y plane
    centersforward(i) = [min(forwardangle)+(max(forwardangle)-min(forwardangle))/(bins)*i-
0.5*(max(forwardangle)...
        -min(forwardangle))/bins];

    centersrear(i) = [min(rearangle)+(max(rearangle)-min(rearangle))/(bins)*i-0.5*(max(rearangle)...
        -min(rearangle))/bins];

    % X plane
    centersx(i) = [min(anglex)+(max(anglex)-min(anglex))/(bins)*i-0.5*(max(anglex)...
        -min(anglex))/bins];
```

```
end
centersforward = centersforward';
centersrear = centersrear';
centersx = centersx';

% Write data to file
fid=fopen(outfile,'at');
fprintf(fid,'Analysis of file %s\n',infile);

% Y plane file printouts
fprintf(fid,'Analysis in the streamwise (Y) direction\n');
fprintf(fid,'Average forward-facing angle:%.2f degrees\n',forwardangle_mean);
fprintf(fid,'Median forward-facing angle:%.2f degrees\n',forwardangle_med);
fprintf(fid,'Standard deviation of forward-facing angles:%.2f degrees\n',forwardangle_dev);
fprintf(fid,'Skewness of forward-facing angles:%.2f degrees\n\n',forwardangle_skew);

fprintf(fid,'Average rearward-facing angle:%.2f degrees\n',rearangle_mean);
fprintf(fid,'Median rearward-facing angle:%.2f degrees\n',rearangle_med);
fprintf(fid,'Standard deviation of rearward-facing angles:%.2f degrees\n',rearangle_dev);
fprintf(fid,'Skewness of rearward-facing angles:%.2f degrees\n\n',rearangle_skew);

% X plane file printouts
fprintf(fid,'Analysis in the cross-stream (X) direction\n');
fprintf(fid,'Average roughness angle:%.2f degrees\n',anglex_mean);
fprintf(fid,'Median roughness angle:%.2f degrees\n',anglex_med);
fprintf(fid,'Standard deviation of angles:%.2f degrees\n',anglex_dev);
fprintf(fid,'Skewness of angles:%.2f degrees\n',anglex_skew);
fclose(fid);

% Plot data
% Y plane data
subplot(3,1,1);
hist(forwardangle,centersforward);
xlabel('Forward-Facing Angles (deg)');
ylabel('Frequency');
title('Histogram of Forward-Facing Angle Data');

subplot(3,1,2)
hist(rearangle,centersrear);
xlabel('Rearward-Facing Angles (deg)');
ylabel('Frequency');
title('Histogram of Rearward-Facing Angle Data');

% X plane data
subplot(3,1,3);
hist(anglex,centersx);
xlabel('Roughness Angle (deg)');
ylabel('Frequency');
title('Histogram of Roughness Angle Data in the Cross-stream (X) Direction');
```

cnc_conversion.m

This program converts raw surface data into a CNC-compatible file for machining. The

results are output to a text file.

```
% Written by James Wammack 03/01/05
% Revised 06/16/05
% This program reads roughness coordinates, converts from mm to in and
% scales the coordinates by some value

clear all;
warning off;

% Obtain user inputs
infile = input('Enter name of input file with its extension:','s');
%width = input('Input step size in y in microns:');
scale = input('Input desired scaling:');
outfile = input('Enter name of output file with its extension:','s');

% Begin counting time
tic;

% Read topological data into MATLAB
M0 = csvread(infile);

t1 = toc/60;
fprintf('Data file read:\t%.2f minutes\n',t1);

% Determine number of rows and columns
rows = 1;
for i=2:size(M0,1)
   if M0(i,2) ~= M0(i-1,2)
      rows = rows+1;
   end
end
points = size(M0,1)/rows;

% Truncate data with respect to Y
for i=1:(rows/2)
   Mtruncy((points*i-(points-1)):points*i,:) = M0((points*(2*i-1)-(points-1))...
      :points*(2*i-1),:);
end

% Truncate data with respect to X
for i=1:(size(Mtruncy,1)/2)
   Mtruncxy(i,:) = Mtruncy((2*i-1),:);
end

t2 = toc/60;
fprintf('Data truncated with respect to X and Y:\t%.2f minutes\n',t2);
```

```
% Determine new number of rows and points
rows2 = 1;
for i=2:size(Mtruncxy,1)
   if Mtruncxy(i,2) ~= Mtruncxy(i-1,2)
      rows2 = rows2+1;
   end
end
points2 = size(Mtruncxy,1)/rows2;

% Create first quadrant of data

% X column
Mx1 = (scale*0.03937)*(Mtruncxy(1:size(Mtruncxy,1),1));

% Y column
My1 = (scale*0.03937)*(Mtruncxy(1:size(Mtruncxy,1),2));

% Z column (adjusted for machining purposes)
Mz1o = (scale*0.03937)*(Mtruncxy(1:size(Mtruncxy,1),3));
Mz1 = Mz1o-max(Mz1o);

% Create second quadrant of data
Mx2 = Mx1+max(Mx1);

My2 = My1;

for i=1:rows2
   Mz1a = Mz1((points2*i+1)-points2:points2*i);
   for j=1:points2
      Mz1b(j) = Mz1a((points2+1)-j);
   end
      Mz2((points2*i+1)-points2:points2*i) = Mz1b;
end

% Combine quadrants 1 and 2 into the lower half of data
for i=1:rows2
   Mxa((points2*(2*i-1)-(points2-1)):points2*(2*i-1)) = Mx1((points2*i+1)-points2:points2*i);
   Mxa((points2*(2*i)-(points2-1)):points2*(2*i)) = Mx2((points2*i+1)-points2:points2*i);
   Mya((points2*(2*i-1)-(points2-1)):points2*(2*i-1)) = My1((points2*i+1)-points2:points2*i);
   Mya((points2*(2*i)-(points2-1)):points2*(2*i)) = My2((points2*i+1)-points2:points2*i);
   Mza((points2*(2*i-1)-(points2-1)):points2*(2*i-1)) = Mz1((points2*i+1)-points2:points2*i);
   Mza((points2*(2*i)-(points2-1)):points2*(2*i)) = Mz2((points2*i+1)-points2:points2*i);
end

% Mirror lower half to produce upper half
Mx(1:size(Mxa,2)) = Mxa;
Mx(size(Mxa,2)+1:2*size(Mxa,2)) = Mxa;
My(1:size(Mya,2)) = Mya;
My(size(Mya,2)+1:2*size(Mya,2)) = Mya+max(Mya);

for i=1:rows2
   Mzb(((2*points2)*i+1)-(2*points2):(2*points2)*i) = ...
      Mza((size(Mza,2)-i*(2*points2)+1):(size(Mza,2)-(i-1)*(2*points2)));
end

Mz(1:size(Mza,2)) = Mza;
```

```matlab
Mz(size(Mza,2)+1:2*size(Mza,2)) = Mzb;

t3 = toc/60;
fprintf('Data has been scaled, mirrored, and converted to inches:\t%.2f minutes\n',t3);

% Print data to a CNC compatible file. Cutting speed is 12in/min
for a=1:size(Mx,2)
    fid=fopen(outfile,'at');
    if a==1
        fprintf(fid,'G0T0Z0\nT1\nM7\nS2000\nX0 Y0.2 Z0.1\nM3\nM100Y\nG01F12\n');
        fprintf(fid,'X%.3f\tY%.3f\tZ%.4f\n',Mx(a),My(a),Mz(a));
    elseif Mx(a)>=(max(Mx)-0.01) && a<size(Mx,2)
        fprintf(fid,'X%.3f\tY%.3f\tZ%.4f\n',Mx(a),My(a),Mz(a));
        fprintf(fid,'G00\n');
        fprintf(fid,'X%.3f\tY%.3f\tZ%.4f\n',Mx(a),My(a),(max(Mz)+0.05));
        fprintf(fid,'X%.3f\tY%.3f\tZ%.4f\n',0,My(a+1),(max(Mz)+0.05));
        fprintf(fid,'G01F12\n');
    else
        fprintf(fid,'X%.3f\tY%.3f\tZ%.4f\n',Mx(a),My(a),Mz(a));
    end
end

fprintf(fid,'Z0.5\nG0T0Z0\nM5\nM2');

fclose(fid);

t4 = toc/60;
fprintf('CNC code has been generated, program complete.\t%.2f minutes\n',t4);
```

Appendix C: Uncertainty Analysis

Freestream and Surface Temperature Uncertainty

Precision error for both T_∞ and T_S were determined using approximately 60 seconds of data taken at a moment in which the tunnel was isothermal.

$$P_{\bar{x}} = t \frac{S_x}{\sqrt{n}} \tag{C.1}$$

Bias error was introduced when calibration curves were used to correct the measurements made by the FLIR camera and freestream thermocouple. This error was approximated to be the standard error of estimate produced when a least-squares best fit is applied to a set of data.

$$S_{y,x} = \sqrt{\frac{\sum y_i^2 - b\sum y_i - a\sum x_i y_i}{n-2}} \tag{C.2}$$

$$a = \frac{n\sum x_i y_i - \left(\sum x_i\right)\left(\sum y_i\right)}{n\sum x_i^2 - \left(\sum x_i\right)^2} \tag{C.3}$$

$$b = \frac{\sum x_i^2 \sum y_i - \left(\sum x_i\right)\left(\sum x_i y_i\right)}{n\sum x_i^2 - \left(\sum x_i\right)^2} \tag{C.4}$$

123

The limited precision of the instruments used to calibrate these two devices (i.e. a Fluke thermocouple reader for IR camera calibration and a mercury thermometer for the freestream thermocouple) introduced further bias. This was approximated to be one half the least count or ±0.05°C. The error introduced into the surface temperature data due to the drift in the IR camera's measurements was approximated to be ±0.1°C. Finally, as mentioned in the text, the uncertainty in the ambient temperature introduced an error of ±0.24°C.

Density and Freestream Velocity Uncertainty

The density of the flow was determined using the ideal gas relation. Pressure uncertainty was considered to be one half the least count of the pressure gage used to determine the ambient pressure for all experiments, which was ±48 Pa. It was found that the uncertainty in freestream temperature had the greatest contribution to the uncertainty in density.

$$w_\rho = \left[\left(w_P \frac{1}{RT_\infty} \right)^2 + \left(-w_{T_\infty} \frac{P}{RT_\infty^2} \right)^2 \right]^{\frac{1}{2}} \qquad (C.5)$$

The uncertainty in velocity was caused by the uncertainty in density as well as the uncertainty in the pressure differential measured by the transducer. The transducer error was dominated by the standard error of estimate produced by the least-squares fit produced during the calibration of the transducer. The precision error of the velocity was determined using 60 seconds of data taken at a near constant velocity.

$$w_{U_\infty} = \left[\left(w_{\Delta P} \frac{1}{2} \left(\frac{2\Delta P}{\rho} \right)^{\frac{-1}{2}} \left(\frac{2}{\rho} \right) \right)^2 + \left(w_\rho \frac{1}{2} \left(\frac{2\Delta P}{\rho} \right)^{\frac{-1}{2}} \left(\frac{-2\Delta P}{\rho^2} \right) \right)^2 \right]^{\frac{1}{2}} \quad \text{(C.6)}$$

Convective and Radiative Heat Transfer Uncertainty

Due to the complexity of the Schultz and Jones equation and the accompanying radiation

calculations, the bias error in the convective heat transfer coefficient, h, was determined

by adding a feature to the program "schultzjones.m" that randomly added or subtracted a

value less than or equal to the uncertainty in that particular temperature measurement for

each data point. The program was run three times for each experiment: once for the

surface temperatures, once for the freestream temperatures, and once for the wall

temperatures. The standard deviation produced for each calculation was used to

determine the precision error contributed by each variable.

Stanton Number Uncertainty

The uncertainty in Stanton number was determined using the uncertainty in the heat

transfer coefficient, the density, the freestream velocity, and the specific heat. The

uncertainty in specific heat was estimated to be one half the least count of the air

properties table from which it was obtained. The average error in Stanton number per

experiment was found to be ±6%.

$$w_{St} = \left[\left(w_h \frac{1}{\rho U_\infty c} \right)^2 + \left(w_\rho \left(-\frac{h}{\rho^2 U_\infty c} \right) \right)^2 + \left(w_{U_\infty} \left(-\frac{h}{\rho U_\infty^2 c} \right) \right)^2 + \left(w_c \left(-\frac{h}{\rho U_\infty c^2} \right) \right)^2 \right]^{\frac{1}{2}} \quad \text{(C.7)}$$

Thermocouple Error

A worst-case-scenario analysis was performed to determine how significant an error radiative heat transfer introduced into the data collected by the 0.005" diameter freestream thermocouple. The thermocouple bead was treated as a sphere in cross flow. Temperatures and velocities were taken from an experiment involving Coupon 3, Burn 2 where the average temperature measured by the thermocouple was 49.3°C.

$$\text{Re}_D = \frac{\rho U_\infty D}{\mu} = 123.8 \tag{C.8}$$

$$\overline{Nu}_D = 2 + \left(0.4\,\text{Re}_D^{\frac{1}{2}} + 0.006\,\text{Re}_D^{\frac{2}{3}} \right) \text{Pr}^{0.4} \left(\frac{\mu}{\mu_s} \right)^{\frac{1}{4}} = 7.174 \tag{C.9}$$

The ratio μ/μ_s is close to one if the freestream and the film temperature near the surface of the bead are nearly equal.

$$\overline{h} = \overline{Nu}_D \frac{k}{D} = 1634.7 W/m^2 K \tag{C.10}$$

An energy balance was performed that assumed that the thermocouple bead was at steady state. The emissivity of the chromel/alumel bead was assumed to be 0.87, which is the emissivity of oxidized chromel.

$$\overline{h}(T_\infty - T_{T-C}) = \varepsilon\sigma\left(T_{T-C}^4 - T_w^4\right) \tag{C.11}$$

$$T_\infty = 49.36°C \tag{C.12}$$

The analysis indicated that the effects of radiation caused a temperature underprediction

of 0.06°C. This is 18% as large as the total error caused by other sources.